Non Linear Dynamics in Complex Systems: From Quantum Systems to Brain Neurons and Galaxies

Thanos Manos

CY CERGY PARIS UNIVERSITÉ

Laboratoire de Physique Théorique et Modélisation (UMR 8089 CNRS)

Mémoire pour la soutenance
de l'Habilitation à Diriger des Recherches

Discipline : Physiques

Non Linear Dynamics in Complex Systems: From Quantum Systems to Brain Neurons and Galaxies

---

Thanos (Athanasios) MANOS

Soutenue à CY Cergy Paris Université,
le 15 décembre 2020, devant le jury composé par :

Rapporteur/Examinateur :	Rainer KLAGES	School of Mathematical Sciences Queen Mary University of London London, UK
Rapporteur/Examinateur :	Astero PROVATA	Statistical Mechanics & Complex Dynamical Systems Laboratory Institute of Nanoscience & Nanotechnology National Center for Scientific Research *Demokritos* Athens, GREECE
Rapporteur/Examinateur :	Andrey SHILNIKOV	Neuroscience Institute Department of Mathematics & Statistics Georgia State University, USA
Examinateur :	Bonnie STEVES	Graduate School Glasgow Caledonian University Scotland, UK
Examinateur :	Dimitri GADOTTI	European Southern Observatory Garching, Munich, GERMANY
Examinateur :	Fernando PERUANI	Laboratoire de Physique Théorique et Modélisation UMR 8089, CNRS - CY Cergy Paris Université 95302 Cergy-Pontoise cedex, FRANCE
Garant/Examinateur :	Alessandro TORCINI	Laboratoire de Physique Théorique et Modélisation UMR 8089, CNRS - CY Cergy Paris Université 95302 Cergy-Pontoise cedex, FRANCE

Acknowledgments

I would like to acknowledge and thank all my collaborators over the last recent years. I have enjoyed the personal and scientific interaction with all of them. The experience I have acquired working with them has helped me to learn a lot and further broaden my scientific research interests into new to me fields.

I would also like to thank Dr. Constanza ROJAS-MOLINA and Dr. Charalampos SKOKOS for reading early drafts of this manuscript and giving me their feedback which ultimately improved its quality.

I am also very grateful to Dr. Astero PROVATA, Dr. Rainer KLAGES and Prof. Andrey SHILNIKOV for having agreed to review this habilitation thesis as well as Prof. Alessandro TORCINI for agreeing to supervise it.

Finally, I wish to thank Meriem MATOUK for her help in the amelioration of the French of the "Résumé".

Cergy-Pontoise
September, 2020

Thanos (Athanasios) MANOS

List of publications

The results presented in this thesis are based on material published in the following articles (in chronological order).

1. **Manos T.** and Robnik M.:*"Dynamical localization in chaotic systems: spectral statistics and localization measure in the kicked rotator as a paradigm for time-dependent and time-independent systems"*, *Phys. Rev. E* **87**, 062905, 2013.

2. Batistić B., **Manos T.** and Robnik M.:*"The intermediate level statistics in dynamically localized chaotic eigenstates"*, *EPL (Europhysics Letters)* **102**, 50008, 2013.

3. **Manos T.**, Bountis T. and Skokos Ch.:*"Interplay between chaotic and regular motion in a time-dependent barred galaxy model"*, *J. Phys. A: Math. Theor.* **46**, 254017, 2013.

4. **Manos T.** and Machado R. E. G.:*"Chaos and dynamical trends in barred galaxies: bridging the gap between time-dependent analytical models and N-body simulations"*, *Mon. Not. R. Astron. Soc.* **438**, 2201–2217, 2014.

5. **Manos T.** and Robnik M.:*"Survey on the role of accelerator modes for anomalous diffusion: the case of the standard map"*, *Phys. Rev. E* **89**, 022905, 2014.

6. **Manos T.** and Robnik M.:*"Statistical properties of the localization measure in a finite-dimensional model of the quantum kicked rotator"*, *Phys. Rev. E* **91**, 042904, 2015.

7. Machado R. E. G. and **Manos T.**:*"Chaotic motion and the evolution of morphological components in a time-dependent model of a barred galaxy within a dark matter halo"*, *Mon. Not. R. Astron. Soc.* **458**, 3578–3591, 2016.

8. Chaves-Velasquez L., Patsis P.A., Puerari I., Skokos Ch. and **Manos T.**:*"Boxy orbital structures in rotating bar models",The Astrophysical Journal* **850**, 145, 2017.

9. **Manos T.**, Zeitler M. and Tass P.A.:*"Short-term dosage regimen for stimulation-induced long-lasting desynchronization"*, *Front. Physiol.* **9**, 376, 2018.

10. **Manos T.**, Zeitler M. and Tass P.A.:*"How stimulation frequency and intensity impact on the long-lasting effects of coordinated reset stimulation'*, *PLoS Comput. Biol.* **14** (5), e1006113, 2018.

11. Popovych O.V., **Manos T.**, Hoffstaedter F. and Eickhoff S.B.:*"What Can Simulations Contribute to Neuroimaging Data Analytics"*, *Front. Syst. Neurosci.* **12**, 68, 2019.

Related papers "in preparation":

1. **Manos T.**, Diaz-Pier S. and Tass P.A.:*"Long-term desynchronization by coordinated reset stimulation in a neural network model with synaptic and structural plasticity"*, (in revision), 2020.

2. Popovych O.V., Kyesam J., **Manos T.**, Diaz-Pier S., Hoffstaedter F., Schreiber J., Yeo, B.T.T. and Eickhoff S.B.:*"Impact of brain parcellation and empirical data on modeling of the resting-state brain dynamics"*, (submitted), 2020.

3. Marostica D. A., Machado R. E. G., **Manos T.** and Athanassoula E.:*"From stellar to halo bars: quantifying the dark matter response"*, (submitted), 2020.

4. **Manos T.**, Skokos Ch. and Patsis P. A.:*"Orbits supporting bars in 3D, rotating, non-autonomous Hamiltonian systems"* (in preparation), 2020.

5. Moges H., **Manos T.** and Skokos Ch.:*"Anomalous diffusion and chaotic motion in standard map lattices"*, (in preparation), 2020.

Abstract

The field of complex systems is a broad scientific area which spans across different disciplines, such as mathematics, physics, chemistry, biology, medicine, engineering and many others. One of their most typical traits is the presence of different interacting components which may exhibit individually regular or chaotic (unpredictable but not random) behaviour. Such type of interactions may result in phenomena whose evolution is not trivial (i.e. complex) to predict, even when the underlying mechanisms happen to be deterministic. This complexity arises from the type of interactions, one of, which is the nonlinear terms in the dynamical equations of the models which are able to better approximate observable data. Nonlinear dynamical systems provide with theoretical concepts and tools for the analysis of a large variety of problems. For example, the investigation of systems where the motion can be chaotic, pattern formation, synchronization phenomena. Nonlinear dynamical systems are typically divided into conservative and dissipative according to whether or not the total energy of the system or some other relevant quantity is conserved. One example of a powerful tool, from this field with many applications in different systems, is the so-called bifurcation analysis. Such an analysis provides an underlying theoretical explanation and model-based prediction of the qualitative variables' time evolution (periodic, quasi-periodic or chaotic) according to given model parameters (fixed or time-dependent). However, when aiming to model systems with different components and study their long term evolution, things become more difficult and complex. Their interplay often gives rise to phenomena that can not be predicted simply by the dynamics of each component separately, its initial conditions and parameters, even when that is well understood. Hence, the emerging dynamics of the whole ensemble can be very different. Examples and applications of such systems can be found in dynamical astronomy, quantum mechanics, brain dynamics and elsewhere. This habilitation thesis aims to summarize a collection of recent results which span along these three research field areas. Namely, results in (i) quantum chaotic systems, anomalous transport and localization of quantal eigenfunctions, (ii) classical chaotic systems with application in galactic dynamics and (iii) brain dynamics and synchronization phenomena with applications in medical treatments of certain diseases. In each respective subject, different questions and problems are posed as well as adequate tools for tackling them, which originate from the field of nonlinear dynamical systems.

Résumé

Le domaine des systèmes complexes est un vaste domaine scientifique qui couvre différentes disciplines, telles que les mathématiques, la physique, la chimie, la biologie, la médecine, l'ingénierie et bien d'autres. L'un de leurs traits les plus typiques est la présence de différents composants en interaction qui peuvent présenter un comportement individuellement régulier ou chaotique (imprévisible mais pas aléatoire). Un tel type d'interactions peut aboutir à des phénomènes dont l'évolution n'est pas triviale (donc "complexe") à prédire, même lorsque les mécanismes sous-jacents se trouvent être déterministes. Cette complexité émerge du type d'interactions, comme c'est le cas des termes non linéaires dans les équations dynamiques des modèles qui sont capables de mieux approcher les données observables. Les systèmes dynamiques non linéaires fournissent des concepts et des outils théoriques pour l'analyse d'une grande variété de problèmes tels que l'étude de systèmes où le mouvement peut être chaotique (imprévisible mais non aléatoire), la formation de motifs et les phénomènes de synchronisation. Les systèmes dynamiques non linéaires sont soit conservatifs soit dissipatifs, selon que l'énergie totale du système ou une autre quantité pertinente est conservée ou non. Un exemple d'outil puissant, issu de ce domaine avec de nombreuses applications dans différents systèmes, est l'analyse dite de bifurcation. Une telle analyse fournit une explication théorique sous-jacente et une prédiction basée sur un modèle de l'évolution temporelle des variables qualitatives (périodique, quasi-périodique ou chaotique) selon les paramètres des modèles donnés (fixes ou dépendants du temps). Cependant, lorsqu'on cherche à modéliser des systèmes avec différents composants et à étudier leur évolution à long terme, les choses deviennent plus difficiles et complexes. Leurs interactions donnent souvent lieu à des phénomènes qui ne peuvent être prédits simplement par la dynamique de chaque composant séparément, ni par ses conditions initiales et ses paramètres, même si cela est bien compris. Par conséquent, la dynamique émergente de l'ensemble peut être très différente. Des exemples et des applications de tels systèmes peuvent être trouvés dans l'astronomie dynamique, la mécanique quantique, la dynamique cérébrale et ailleurs. Cette thèse d'habilitation vise à résumer un ensemble de résultats récents qui couvrent ces trois domaines de recherche. À savoir, il en résulte (i) des systèmes chaotiques quantiques, un transport anormal et une localisation de fonctions propres quantiques, (ii) des systèmes chaotiques classiques avec application dans la dynamique galactique et (iii) la dynamique cérébrale et des phénomènes de synchronisation avec des applications dans les traitements médicaux de certaines maladies. Pour chacun de ces sujets, différentes questions et problèmes sont posés. Pour les aborder, des outils adéquats issus du domaine des systèmes dynamiques non linéaires sont utilisés.

General introduction

Nonlinear Dynamical Systems and complexity

The theoretical background and framework of dynamical systems have been and still are broadly used on a large spectrum of research areas. Applications of dynamical systems, employing differential equations, are found in mathematics, physics, chemistry, engineering, economics, sociology, medicine etc. Dynamical systems are divided into two main categories, linear and nonlinear according to the underlying process one aims to describe. Linear dynamical systems are to a large extent simpler, well understood and have limited applications. A plethora of phenomena in nature are better and more accurately described by employing nonlinear terms in our models. Such deterministic systems are able to generate complex and often counterintuitive variables' time evolution, like for example chaotic motion (unpredictable but not random). Dynamical systems together with other research fields such as network dynamics, pattern formation, game theory, collective behavior and others, can help us to model and better understand complex interactions in nature and self-organization phenomena, i.e. the so-called complex systems [Vemuri 1978].

Nonlinear dynamical systems can be further divided into conservative (Hamiltonian) and dissipative. For the former, the type of evolution (qualitatively) is associated with the number of conserved quantities (e.g. total energy, angular momentum etc.) and the degrees of freedom, while for the latter one can use dissipative quantities (e.g. Lyapunov functions). Furthermore, the bifurcation analysis provides an underlying theoretical explanation and model-based prediction of the qualitative variables' time evolution (periodic, quasi-periodic or chaotic) according to given model (fixed or time-dependent) parameters [Strogatz 2000].

This habilitation thesis aims to summarize a collection of recent results which span along three quite (at a quick first glance) different and fascinating research field areas. Nevertheless, there are many links among them when one models their evolution and collective behavior using concepts and properties from nonlinear dynamical systems theory. Hence, we present here results in (i) quantum chaotic systems, anomalous transport and localization of quantal eigenfunctions, (ii) classical chaotic systems with applications in galactic dynamics and (iii) brain dynamics and synchronization phenomena with applications in medical treatments of certain diseases. Evidently, in each respective subject, different questions and problems are posed, as well as different tools for tackling them.

Setting as a starting point the classical dynamical systems, there is a well-developed framework for the description of different natural phenomena, i.e. their evolutionary mechanisms, their potential sensitivity to initial conditions, the transition from one state to another (often associated with some model parameter, e.g. bifurcations), potential model limitations etc. Stellar dynamics is one example where physical models are used for the description of stars' motion (e.g. in galaxies), tested for supporting sufficiently well observed complex structural patterns as well their stability and much more. When switching to the study of quantum systems there are evidently major differences compared to classical systems in many aspects. Yet, they are related to each other. For example, several properties observed in quantum (chaotic) systems, such as localization of eigenfunctions and kinetic energy diffusion, are directly associated with their classical corresponding model, at least up to certain time scales. In this framework, understanding the classical models can help in the better description and prediction of the quantum ones. In brain dynamics, and when setting out to model collective (e.g. electrical) activity and dynamics of networks, composed either by point neurons (micro-scale)

or mean activity of larger areas (meso/macro scale), systems of nonlinear ordinary (and partial) differential equations also provide an adequate tool. There is a large spectrum of mathematical models which are constructed and actively (re-)validated by (new) empirical data for the description for different (from a physiological point of view) neuron populations whose distinct spiking patterns affect their collective (healthy or abnormal) activity. The latter is often quantified by the concept of the so-called synchronization which, roughly speaking, measures the degree of the relative rhythmic or repetitive patterns of neural activity. Switching from one rhythmic state to another can be modeled via parameter changes of the model, associated to attractors in the phase space, bifurcations and network analysis.

In this thesis, several concepts of chaos in classical systems are also mentioned and used in the quantum ones, hence, we opt to list the chapter order as follows: in Chapter 1, we start with the discussion classical chaos in astrophysics, then, in Chapter 2, we discuss a few recent findings on quantum chaos, transport and localization and finally in Chapter 3 we focus on neural (de-)synchronization phenomena in the human brain related to healthy vs pathological activity.

Classical Chaos in Astrophysics

The main concepts of *classical chaos* lie on the so-called sensitivity to initial conditions in low–dimensional systems and their origins go back to Henri Poincaré, the 3–body problem, the fact that it is not integrable and the coexistence of quasi-periodic and chaotic dynamics in such Hamiltonian systems. In addition the basic defining property of deterministic chaos, i.e. the divergence of initially nearby phase space trajectories, is quantified by the positivity of the largest Lyapunov exponent [Lichtenberg and Lieberman 1992]. In astrophysics, one employs nonlinear dynamical systems to model astronomical systems, e.g. celestial bodies, planetary satellites, pulsating stars, and their evolution. To this end, one may consider the *gravitational N–body problem* (GNBP), in order to model planetary systems, star clusters of various richness, galaxies and galaxy clusters and super–clusters (clusters of clusters). In this framework all types of interactions, except the gravitational one, are not taken into account, as the body distances are much larger than their typical sizes and thereby are not affecting their dynamics. A special case of the GNBP, is the $N = 2$ case which is equivalent to the one–body (Kepler) problem. In such models, the body evolution is determined only by their gravitational self-interactions and the relative motion and patterns are self-organized. An alternative approach to the GNBP, is the use of Hamiltonian systems, namely dynamical systems that follow Hamilton's equations with conservation properties linked to symmetries of the Hamiltonian function which describes the system and its phase space (periodic, quasi-periodic and chaotic) dynamics. The Hénon & Heiles model [Hénon and Heiles 1964] is considered one of the first such Hamiltonian systems, exhibiting deterministic chaos which considers point mass stars in a mean field model approximation of an axially symmetric galaxy.

Orbits of stars are the fundamental building blocks of any galactic structure and their properties give important insight for understanding the formation and evolution of such structures [Binney and Tremaine 2008]. Our understanding relies significantly on the adequacy and efficiency of the models used either in the time-dependent (TD) self-consistent models or in the rather 'simpler' analytical time-independent (TI) ones. It is by now well accepted that the chaotic or regular nature of orbits influences the general stability of the N-body simulations, which is straightforwardly related to the underlying dynamics. Therefore, studying the general stability and the detailed structure of the phase (but also of the configuration) space of analytical models can be proven to be very useful,

provided that the gravitational potentials are realistic in terms of representing density distribution profiles close to those derived by simulations. In this Chapter, we summarize some recent results on TD analytical models, their, in general, good agreement with N-body simulations, the presence and evolution of periodic orbits associated with the main galaxy features like the barred shape, the distribution of regular and chaotic motion in the phase as well as configuration space.

Quantum Chaos, Diffusion and Localization

Quantum chaos or *wave chaos* is a more recent branch of chaotic dynamical systems and its main goal is to study the properties of quantum systems which, in their classical limit, exhibit classical (deterministic) chaotic dynamics [Stöckmann 1999; Haake 2001]. Applications of quantum chaos can be found in many areas, such as nuclear, atomic and molecular physics, quantum transport, mesoscopic solid-state systems, wave propagation, acoustics, quantum computers etc.

With the term *quantum motion*, one refers to the time evolution of the wavefunctions. Even though quantum motion of bound systems with purely discrete energy spectrum is ultimately (after sufficiently long time) stable and regular (almost periodic), it exhibits many features of the classical motion such as for example diffusion in a chaotic domain, for time up to the Heisenberg time. The Heisenberg time, also called *break time*, is an important time scale in any quantum system, and is given by $t_H = 2\pi\hbar/\Delta E$, where $h = 2\pi\hbar$ is the *Planck constant* and ΔE is the mean energy level spacing, such that the mean energy level density is $\rho(E) = 1/\Delta E$. For time shorter than approximately t_H the quantum diffusion follows the classical chaotic diffusion, but is stopped at larger times, just due to the interference phenomena (similar to *Anderson localization* occurring for particles in disordered solids). Pictorially speaking, for time up to t_H the quantum system behaves as if its evolution operator has a continuous spectrum, like the classical one has in the chaotic regime, but at later times it senses the discreteness of the spectrum. If the quantum diffusion stops, while the classical chaotic diffusion continues, we speak about the *dynamical localization*, or *quantum localization* or *Chirikov localization*, first observed in time-dependent systems [Casati, Chirikov, et al. 1979]. The problem of quantum or dynamical localization is related to the Anderson localization model, within the framework of the tight-binding approximation, with hopping transitions between the nearest neighbors [Fishman, Grempel, and Prange 1982]. We here summarize some recent results on dynamical localization in time-dependent periodic (Floquet) systems and diffusion properties, exemplified by the quantum kicked rotator.

Modeling Neurons and the Dynamics of the Brain

Biological systems is another field where nonlinear dynamical systems have also been used for the description and understanding of complex collective activity. One of the most important applications is in the dynamics of nerve membranes via the so-called action potential. Such a biological activity resembles the one used for the dynamics of electric circuits and ideas from the field of nonlinear dynamical systems are also used here, associating the type of activity of individual cells/neurons or the interaction as ensembles (networks) with bifurcations of certain parameters resulting in periodic, quasi-periodic or chaotic activity.

Alan Hodgkin and Andrew Huxley pioneered the field of dynamical neuroscience when in 1952 introduced a mathematical model of nonlinear differential equations to describe and explain the mechanisms of the electrophysiological activity of squid giant axons (i.e. nerve membranes), based

on their experimental data. When a squid giant axon is not sending any signal is said to be at rest. One can modulate the dynamical activity of such nerve by modifying external ionic (such as the calcium) concentrations around the axon and induce self-sustained oscillations [Huxley 1959; Hodgkin and Huxley 1952], a state at which the nerve membrane acts as a neural oscillator. Linking these behaviors to dynamical systems' terminology, the resting state corresponds to a stable equilibrium point while the oscillatory to a stable limit cycle. Non-periodic (chaotic) oscillations can also be observed [Izhikevich 2007]. Transitions from one state to another take place via bifurcations associated to model parameters and/or external electrical input.

When aiming to understand the collective behavior of neural systems (ensembles of neurons), besides the individual's neuron activity pattern, the concept of *synchronization* becomes rather relevant. Namely, the adjustment of rhythmic activity of self-sustained periodic (neural) oscillators due to the type of (network) connectivity and interaction they have which, in a more physiologically realistic description, can be time dependent (plasticity). Such a collective activity is usually associated to the dynamics of the neurons' phases (neurons can be modeled as oscillators), their relative phase difference which may result to phase locking, frequency entrainment or asynchronous activity [A. Pikovsky, Rosenblum, and Jürgen Kurths 2003; Strogatz 2003].

Neuronal synchronization processes are relevant under normal as well as abnormal conditions. A number of brain disorders are associated with abnormal neuronal synchrony, for example Parkinson's disease (see e.g. [Hammond, Bergman, and Brown 2007]), tinnitus (see e.g. [Elgoyhen et al. 2015]) and epilepsy (see e.g. [Wong, Traub, and Miles 1986]). To specifically counteract abnormal neuronal synchrony and, hence, related symptoms, a number of invasive and non-invasive techniques have been developed over the last years. Coordinated Reset (CR) stimulation is a rather recent protocol which employs basic plasticity and dynamic self-organization principles of the nervous system. Its fundamental goal is to induce long-lasting desynchronizing effects that persist cessation of stimulation. The latter are key to reducing side effects of invasive therapies such as the standard high-frequency (> 100 Hz) deep brain stimulation [Deuschl et al. 2006] which has only acute clinical and electrophysiological effects, present only during stimulation as well as a number of adverse events, such gait disturbances and speech problems. We here summarize some recent results on efficient and optimized CR stimulation signal patterns which induce long-lasting desynchronization of abnormal activity that may occur in Parkinson's disease and tinnitus.

The thesis consists of three Chapters based largely on published papers. Each Chapter is dedicated to one of the above described topics with a separate and extensive introduction of the topic's background and general concepts, the models' presentation, a few representative results from the related published papers and a summary accompanied with perspectives for future investigation. Each Chapter is self-contained in order to give the reader a good overview of the published work in the respective eleven papers listed in the "List of publications" section. All journals gave permission to use these papers in their published versions and to be inserted after each respective Chapter. However, that choice would substantially increase the thesis' size, and for this reason we opted for a more dense and concise style, still enabling an independent reading. A collection of all the aforementioned papers can be found either on the respective online journals' web-pages or alternatively on my personal web-page: https://sites.google.com/site/thanosmanos/Publications. At the end of the thesis one can find the full bibliography for all chapters.

Contents

Chapter 1

Classical chaos in astrophysics

1.1 Background and introduction

Orbits of starts are generally regarded as the backbone of structure in galaxies. Exploring orbital properties in general – and in particular the evolution of their dynamical stability – is a fundamental aspect in improving our understanding of galactic structures as a whole [Binney and Tremaine 2008]. Our ability to explore the details of orbital stability in galaxies depends considerably on the adequacy of analytical models, which can be time-independent (TI) or time-dependent (TD). Studying the stability and the phase space structure via analytical models (see e.g. [Manos and Athanassoula 2011]) has proven to be quite useful (for a review, see [Contopoulos 2002]), as long as those potentials are realistic, in the sense of adequately representing the density distributions of real galaxies. It is well accepted that the chaotic or regular nature of orbits influences the general stability of the N-body simulations, which is straightforwardly related to the underlying dynamics (self-consistent, i.e. the motions are caused from the forces generated by the masses themselves). Hence, studying the general stability and the detailed structure of the phase and configuration space of analytical models can be proven to be very useful, provided that these potentials are realistic in terms of representing density distribution profiles close to those derived by simulations or extracted from observational data.

The general nature of an orbit, in conservative (Hamiltonian) TI-systems, can only be one of the following: periodic (*stable* or *unstable*), quasi-periodic or chaotic [Lichtenberg and Lieberman 1992]. Nevertheless, there are cases where chaos can be characterized as *weak*, suggesting that orbits spend a significant fraction of their time in confined regimes and do not fill up phase space as 'homogeneously' as the *strongly* chaotic ones. In these cases, the different rate of diffusion in the phase space plays an important role, associating for example the weak chaotic motions with barred or spiral galaxy features, giving rise to a number of interesting results, see e.g. [Athanassoula, Romero-Gómez, Bosma, et al. 2009; Athanassoula, Romero-Gómez, and Masdemont 2009; Athanassoula, Romero-Gómez, Bosma, et al. 2010; Harsoula and Kalapotharakos 2009; Harsoula, Kalapotharakos, and Contopoulos 2011a; Harsoula, Kalapotharakos, and Contopoulos 2011b; Contopoulos and Harsoula 2013; Kaufmann and Contopoulos 1996; Patsis, Athanassoula, and Quillen 1997; Patsis 2006; Romero-Gómez, Masdemont, et al. 2006; Romero-Gómez, Athanassoula, et al. 2007; T. Bountis, Manos, and C. Antonopoulos 2012]. There are also several results in the recent literature showing that strong local instability does not necessarily imply widespread diffusion in phase space [Cachucho, Cincotta, and Ferraz-Mello 2010; Giordano and Cincotta 2004]. In [Contopoulos and Harsoula 2008; Contopoulos and Harsoula 2010] 'stickiness' was studied thoroughly in 2-degrees of freedom (d.o.f.) while in [Katsanikas, Patsis, and Pinotsis 2011; Katsanikas and Patsis 2011; Katsanikas, Patsis, and Contopoulos 2011] and in [Manos, C. Skokos, and C. Antonopoulos 2012] the role of 'sticky' chaotic orbits and the diffusive behavior, in the neighborhood of invariant tori surrounding periodic solutions of the Hamiltonian in the vicinity of periodic orbits in conservative systems, was also studied.

Lyapunov exponents (see e.g. [C. Skokos 2010] for a review and references therein) have been extensively used for the detection of chaotic motion in several different models. However, there are often disadvantages which hinder their use, for example their slow convergence. Several approaches exist to detect and quantify chaos, whose differences and efficacy have been thoroughly compared and discussed in the recent literature (see [Contopoulos 2002; Maffione et al. 2011; Maffione et al. 2013] and references therein). In [Ch. Skokos, Gottwald, and Laskar 2016] the reader may find a special volume with a more complete and recent review of the several broadly used chaos detection methods and their predictability as well as all the relevant references regarding their theoretical background, numerical implementation and applications in various models. We use the Generalized Alignment Index (GALI) method [C. Skokos, T. C. Bountis, and C. Antonopoulos 2007; Manos, T. Bountis, and C. Skokos 2013; C. Skokos and Manos 2016]. In [Manos, T. Bountis, and C. Skokos 2013], a study was carried out focusing on the dynamics of a barred galaxy model containing a disc and a bulge component. Considering a TD analytical model – extending a TI one [Manos, C. Skokos, Athanassoula, et al. 2008; Manos and Athanassoula 2011; T. Bountis, Manos, and C. Antonopoulos 2012] – whose mass parameters of the bar and disc potential vary linearly as functions of time (the one at expense of the other). Two very general conceivable cases in barred galaxies were analyzed: (a) a model where the mass of bar grows, considering a common trend found in N-body simulations due to the exchange of angular momentum (see e.g. [Athanassoula and Misiriotis 2002; Athanassoula 2003]) and (b) a case where the bar gets weaker by losing mass (see e.g. [Combes 2008a; Combes 2008b]). There, a reliable way of using the GALI chaos detection method was used for estimating the relative fraction of chaotic *vs.* regular orbits in such TD potentials. We stress here that in the TD models, individual trajectories may display sudden transitions from regular to chaotic behavior and vice versa during their time evolution and in general the 'sticky' behaviour, as discussed in the literature, is less pronounced. This is also the typical case in the N-body simulations where, generally speaking, the motion may also be either: (i) regular throughout the whole evolution, (ii) chaotic throughout the whole evolution, (iii) alternate between chaotic and regular motion with simultaneously orbital shape change (but not necessarily), e.g. from disc to bar like, etc.

Regarding the galaxies' evolution and formation of their several features, it is generally accepted that the most appropriate way to study them is by analyzing N-body simulations. The self-consistency of the models in this approach captures much better several details of the general dynamics. The direct application of chaos detection methods to individual orbits is still a rather difficult task while, for a large ensemble of particles, it is even harder if not unfeasible. To overcome this obstacle, mean field potentials have been used in the literature in order to study in more detail the dynamical properties of a specific N-body simulation. These potentials are referred to as 'frozen' are TI and are derived at specific snapshots of the simulations. Hence, one can apply chaos detection tools to the mean field potential instead of the N-body simulation. For example, [Muzzio, Carpintero, and Wachlin 2005] used an elliptical galaxy simulation (no bar or halo) without dissipation which collapses and eventually reaches an equilibrium state. Then, by taking a quadrupolar expansion of the frozen snapshot, they derive a stationary smooth potential. In [Voglis, Stavropoulos, and Kalapotharakos 2006] and references therein, the authors deal with disc galaxies, focusing mainly on the spiral structures rather than bars (no halo) while the extraction of the mean field potential is again performed in a similar manner. Following this approach, the role of chaotic motion and diffusion rate in barred spiral galaxies has also been studied [Harsoula and Kalapotharakos 2009; Harsoula, Kalapotharakos, and Contopoulos 2011a; Harsoula, Kalapotharakos, and Contopoulos 2011b; Maffione et al. 2013; Contopoulos and Harsoula 2013] while some applications to the Milky Way bar can be found in [Y.

Wang et al. 2012] and recently a new code for orbit analysis and Schwarzschild modelling of triaxial stellar systems was given in [Vasiliev 2013]. Nevertheless, following this approach one only derives a stationary mean field model for an equilibrium state of the simulation under study. Furthermore, it does not incorporate an appropriate type set of parameters that would be able to describe and reproduce the time-dependencies in axis ratios, masses, pattern speed, etc. of the several components of a model, like for example the growth of the bar component or the evolution of the disc in time. Let us point out here, the fact that in all these approaches the orbits under study can be only either regular or chaotic. The latter ones may be further distinguished to strongly or weakly chaotic, depending on their diffusion properties, sticky effects etc... during the whole evolution.

We here consider an N-body simulation of a disc galaxy embedded in a live halo (i.e. both the stellar disc and the dark matter halo are represented by responsive particles). Disc-halo interaction leads to the formation of a strong bar. We then measure how the galaxy components vary in time during the simulation. The time evolution of the structural parameters is provided as input to the analytical TD model we build. This 'candidate' analytical mean field potential is meant to mimic the N-body simulation evolution and more importantly to generate orbits with more similar (and in some sense 'richer') morphological behaviour to those of the N-body simulation, i.e., permitting for individual orbits the interplay between regular and chaotic epochs as time evolves and providing a stable structure at the same time. Note that, in TI frozen models an orbit cannot convert from chaotic to regular. Our TD model is composed of three components (bar, disc and halo) whose parameters were fitted with the N-body measurements, via the rotation curves. Note that many simplifying assumptions are made. For example, our TD model considers an (ellipsoidal) analytical bar component which is not always an excellent approximation of the shape of the actual N-body bar. Likewise, the analytical description of the halo and the disc cannot be expected to behave identically, either. However, our goal is to study the general dynamical impact in stability caused by the bar's growth in time (as it happens in the N-body simulation). Thus, by using a realistic TD model, without aiming to describe of the exact detailed dynamics yielding from the simulation, we can use chaos detection tools and quantify general trends of the fraction of regular and chaotic orbits in the phase and configuration space. Keeping this in mind, we draw (disc) initial conditions directly from the simulation and we evolve them in time with the mean field TD potential.

1.2 The $N-$body and time-dependent analytical models

The $N-$body simulation

To serve as the base reference for the analytical model, we use one of the simulations described in [Machado and Athanassoula 2010]. For simplicity, we select initial conditions with a spherical halo. The mass of the stellar disc is $M_d = 5 \times 10^{10}\ M_\odot$, with an exponential density profile of radial scale length $R_d = 3.5$ kpc, and vertical scale height $z_0 = 0.7$ kpc:

$$\rho_d(R,z) = \frac{M_d}{4\pi z_0 R_d^2} \exp\left(-\frac{R}{R_d}\right) \mathrm{sech}^2\left(\frac{z}{z_0}\right), \tag{1.1}$$

The spherical dark matter halo has a [Hernquist 1993] density profile and it is five times more

massive than the disc:

$$\rho_h(r) = \frac{M_h}{2\pi^{3/2}} \frac{\alpha}{r_c} \frac{\exp\left(-r^2/r_c^2\right)}{r^2 + \gamma'^2}, \tag{1.2}$$

where $M_h = 2.5 \times 10^{11}\ M_\odot$ is the mass of the halo, $\gamma' = 1.7$ kpc is a core radius and $r_c = 35$ kpc is a cutoff radius. The normalisation constant α is defined by

$$\alpha = \{1 - \sqrt{\pi} q \exp\left(q^2\right)[1 - \mathrm{erf}(q)]\}^{-1} \tag{1.3}$$

where $q = \gamma'/r_c$. For additional details on the initial conditions, see [Machado and Athanassoula 2010].

This is a fairly representative collisionless simulation of a strongly barred galaxy. Four snapshots of the disc particles are displayed in the upper row of Fig. 1.1. It was performed with the N-body code GYRFALCON [Dehnen 2000; Dehnen 2002] using a total of 1.2 million equal-mass particles, with a gravitational softening length of 0.175 kpc, resulting in 0.1 per cent energy conservation. The simulation was carried out for approximately one Hubble time.

N-body simulations have been employed to study chaotic motion in simplified models of disc galaxies. For example, [Voglis, Stavropoulos, and Kalapotharakos 2006] study chaos and spiral structure in rotating disc galaxies, but those galaxies are not embedded in dark matter haloes. The connection between chaos and bars was also analysed by [El-Zant and Shlosman 2002], with models were set up by the addition of disc, bar and halo components. They found that in centrally concentrated models, even a mildly triaxial halo lead to the onset of chaos and the dissolution of the bar in a timescale shorter than the Hubble time.

The time-dependent analytical model

We construct an analytical model that is described by its total gravitational potential $V = V_B(t) + V_D(t) + V_H(t)$, where the three components correspond to the potentials of the bar, disc, and halo, respectively. These components will evolve in time, in accordance with the behaviour we measure from the simulation (see [Manos and Machado 2014] for a detailed motivation and justification).

(i) A triaxial Ferrers bar [Ferrers 1877], whose density is given by:

$$\rho(x,y,z) = \begin{cases} \rho_c(1-m^2)^2 & \text{if} \quad m < 1, \\ 0 & \text{if} \quad m \geq 1, \end{cases} \tag{1.4}$$

where $\rho_c = \frac{105}{32\pi} \frac{GM_B(t)}{abc}$ is the central density, $M_B(t)$ is the mass of the bar, which changes in time, and $m^2 = \frac{x^2}{a^2} + \frac{y^2}{b^2} + \frac{z^2}{c^2}$, $a > b > c > 0$, with a, b and c being the semi-axes of the ellipsoidal bar. The corresponding bar potential is:

$$V_B(t) = -\pi G a b c \frac{\rho_c}{3} \int_\lambda^\infty \frac{du}{\Delta(u)} (1 - m^2(u))^3, \tag{1.5}$$

where G is the gravitational constant (set to unity), $m^2(u) = \frac{x^2}{a^2+u} + \frac{y^2}{b^2+u} + \frac{z^2}{c^2+u}$, $\Delta^2(u) = (a^2+u)(b^2+u)(c^2+u)$, and λ is the unique positive solution of $m^2(\lambda) = 1$, outside of the bar ($m \geq 1$), while $\lambda = 0$ inside the bar. The analytical expression of the corresponding forces are given in [Pfenniger 1984]. In our model, the shape parameters (i.e. the lengths of the ellipsoid axes a, b and c are) are also functions of time.

(ii) A disc, represented by the Miyamoto–Nagai potential [Miyamoto and Nagai 1975]:

$$V_D(t) = -\frac{GM_D(t)}{\sqrt{x^2+y^2+(A+\sqrt{z^2+B^2})^2}}, \tag{1.6}$$

where A and B are its horizontal and vertical scale-lengths, and $M_D(t)$ is the mass of the disc. Here, 'disc mass', refers to the stellar mass excluding the bar. As the bar grows, its mass increases at the expense of the remainder of the disc mass, such that the total stellar mass is constant: $M_B(t) + M_D(t) = 5 \times 10^{10}\ M_\odot$. The parameters A and B are also functions of time.

(iii) A spherical dark matter halo, represented by a Dehnen potential [Dehnen 1993]:

$$V_H(t) = \frac{GM_H}{a_H} \times \begin{cases} -\frac{1}{2-\gamma}\left[1-\left(\frac{r}{r+a_H}\right)^{2-\gamma}\right] & , \quad \gamma \neq 2, \\ \ln\frac{r}{r+a_H} & , \quad \gamma = 2. \end{cases} \tag{1.7}$$

M_H is the halo mass, a_H is a scale radius and the dimensionless parameter γ (within $0 \leq \gamma < 3$) governs the inner slope. The halo mass is constant throughout, but the parameters a_H and γ are functions of time. For $\gamma < 2$ its finite central value is equal to $(2-\gamma)^{-1}GM_H/a_H$.

Instead of attempting to use the (disc and halo) profiles from the N-body simulations, we opted to represent the bar, disc and halo using respectively the Ferrers, Miyamoto–Nagai and Dehnen profiles. There are two reasons for such a choice. First, our approach requires analytical simplicity that could not be afforded by the profiles used in the initial conditions of the numerical simulation. Secondly, due to bar formation and evolution, the initial disc profile in the simulation soon becomes a poor representation in the inner part of the galaxy, where the bar resides. In this sense, it is not advantageous to continue using the initial profiles to model later times. A Miyamoto–Nagai disc provides a sufficient approximation for our purposes. Likewise, even though the [Hernquist 1993] halo profile is well suited for numerical purposes, it is inconvenient from the analytical point of view. We experimented with simple logarithmic halo profiles (because their rotation curves are also appropriate), but the [Dehnen 1993] profile was preferable, as it provided equally acceptable rotation curves, and a more satisfactory global approximation of the mass distribution. Similarly, fitting the bar by a Ferrers ellipsoid is a justifiable approximation. Surely, it fails to capture the N-body bar in all its complexity, particularly after the buckling instability, when the bar is substantially strong and develops the peanut-shaped feature. In general, the N-body bar will be more boxy than the Ferrers shape would allow. Nevertheless, fitting an ellipsoid of the same extent allows us to obtain plausible shapes, to determine the bar orientation and to estimate its mass adequately. Ultimately, regardless of small deviations in the density profiles, our goal is to obtain an analytical total potential that is approximately comparable to the overall potential of the simulation. From the simulation, we are able to measure several quantities as a function of time, which are then used to inform the analytical model.

For the bar, and following [Manos and Machado 2014], the required parameters are the bar mass, the bar shape and the bar pattern speed Ω_b. First, we estimate the bar length as a function of time. This is done by measuring the relative contribution of the $m = 2$ Fourier component of the mass distribution as a function of radius, for each time step, and finding the radius at which the $m = 2$ has its most intense drop after the peak. This radius a is associated with the bar length. Then we

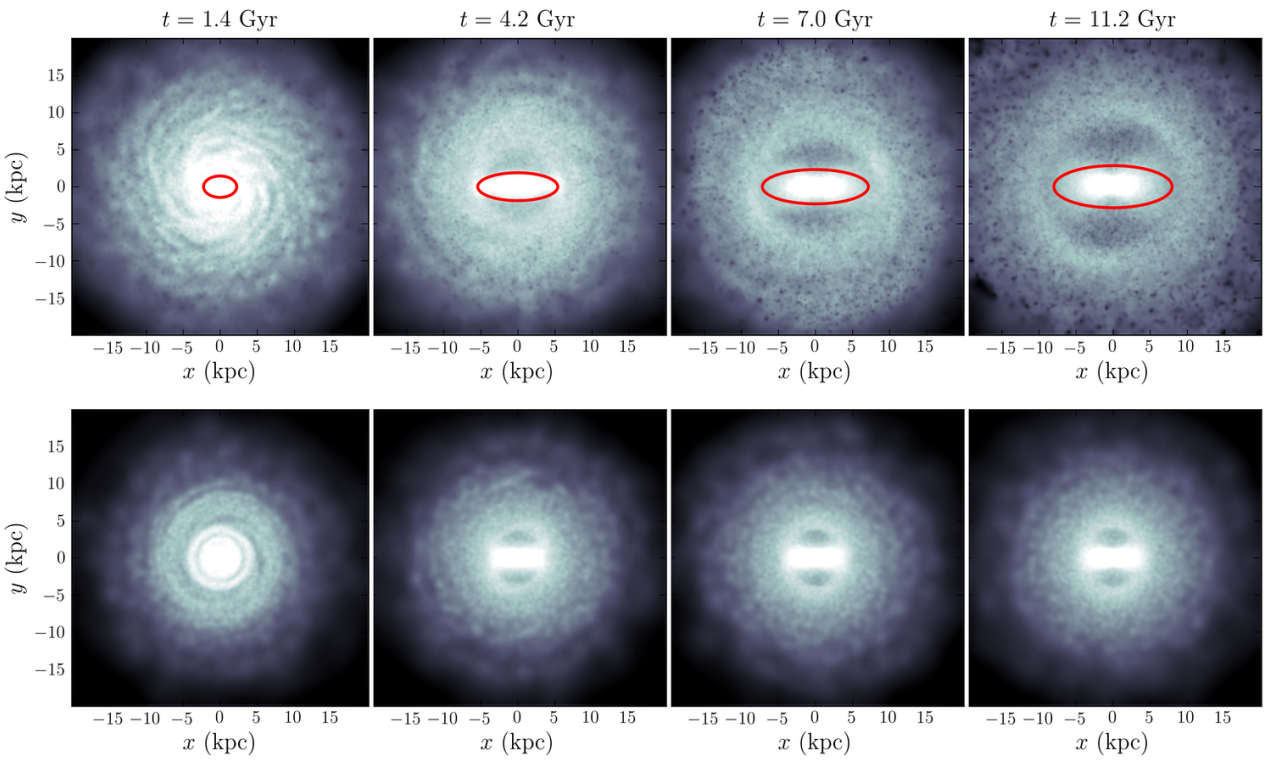

Figure 1.1: Snapshots of the N-body simulation (upper panels) at four different times, displaying stellar density, on the same range, projected on the xy plane. Each frame is 40 by 40 kpc. To illustrate bar lengths and shapes, we overlay ellipses (which are not isophotal fits). The lower panels display the result of evolving an ensemble of initial conditions in the presence of the constructed TD analytical potential.

estimate the bar shape by calculating the axis ratios b/a and c/a from the eigenvalues of the inertia tensor in this region. The bar mass is measured by simply adding up the mass enclosed within an ellipsoid of axes a, b, c. Finally, the successive orientations of the major axis as a function of time are used to compute the pattern speed. The resulting time evolution of all these quantities are displayed in the fourth, fifth and sixth panels of Fig. 1.2. Each of these parameters is measured at several time steps, a sample of which is shown, along with the resulting polynomial fits.

The disc mass $M_D(t)$ is known once the bar mass has been measured, and the halo mass M_H is constant. One still requires the time evolution of two disc parameters (A, B) and two halo parameters (a_H, γ). This is achieved by measuring the rotation curves directly from the simulation (at each time step), and then fitting the analytical $v_c(R)$ to these data. Since the disc and halo potentials are known from equations (1.6) and (1.7), we obtain their respective analytical circular velocities from $v_c^2 = R\frac{dV}{dR}$:

$$v_{c,D}^2(R) = R^2 \, \frac{GM_D}{[R^2 + (A+B)^2]^{3/2}} \tag{1.8}$$

$$v_{c,H}^2(R) = GM_H \, \frac{r^{2-\gamma}}{(r+a_H)^{3-\gamma}} \tag{1.9}$$

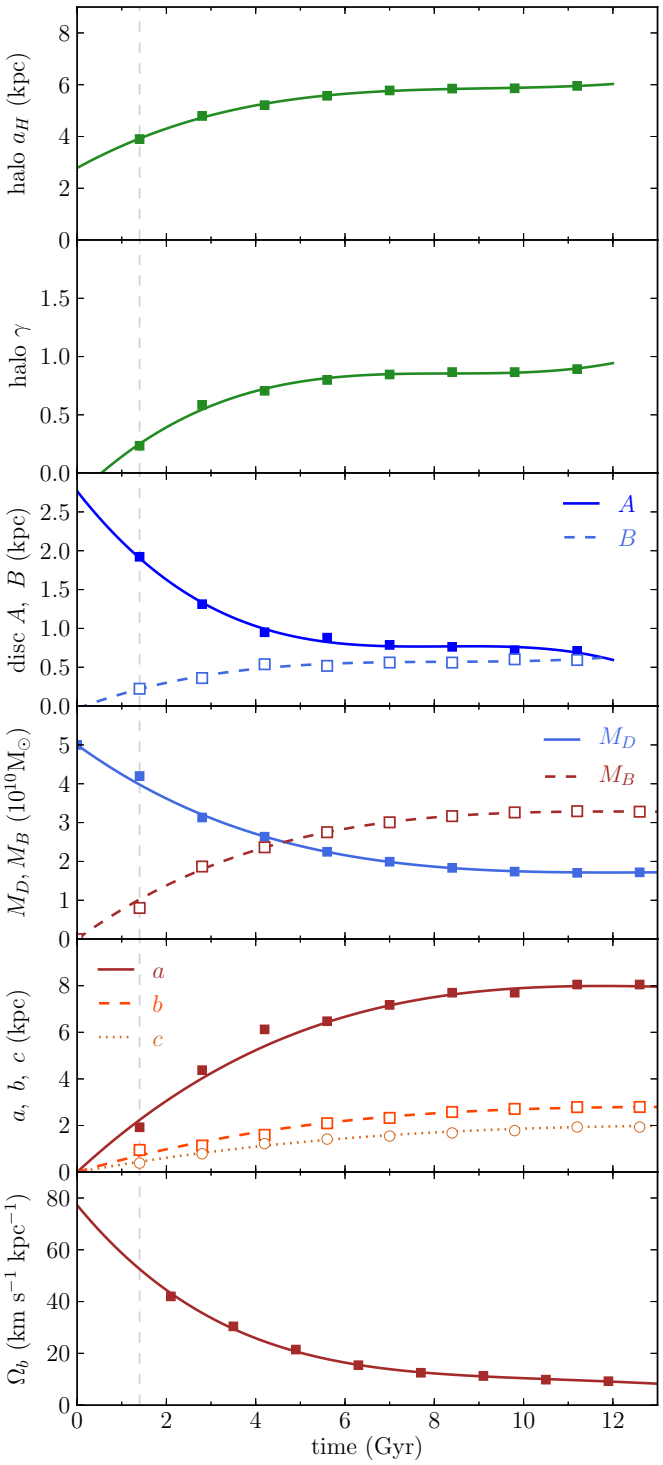

Figure 1.2: Time evolution of the halo, disc and bar parameters, measured from the N-body simulation (points) and supplied to the analytical model (fitted polynomials). First and second panel: parameters of the Dehnen halo profile. Third: parameters of the Miyamoto–Nagai disc. Fourth: bar mass and disc mass. Fifth: semi-major axes of the bar. Sixth: bar pattern speed.

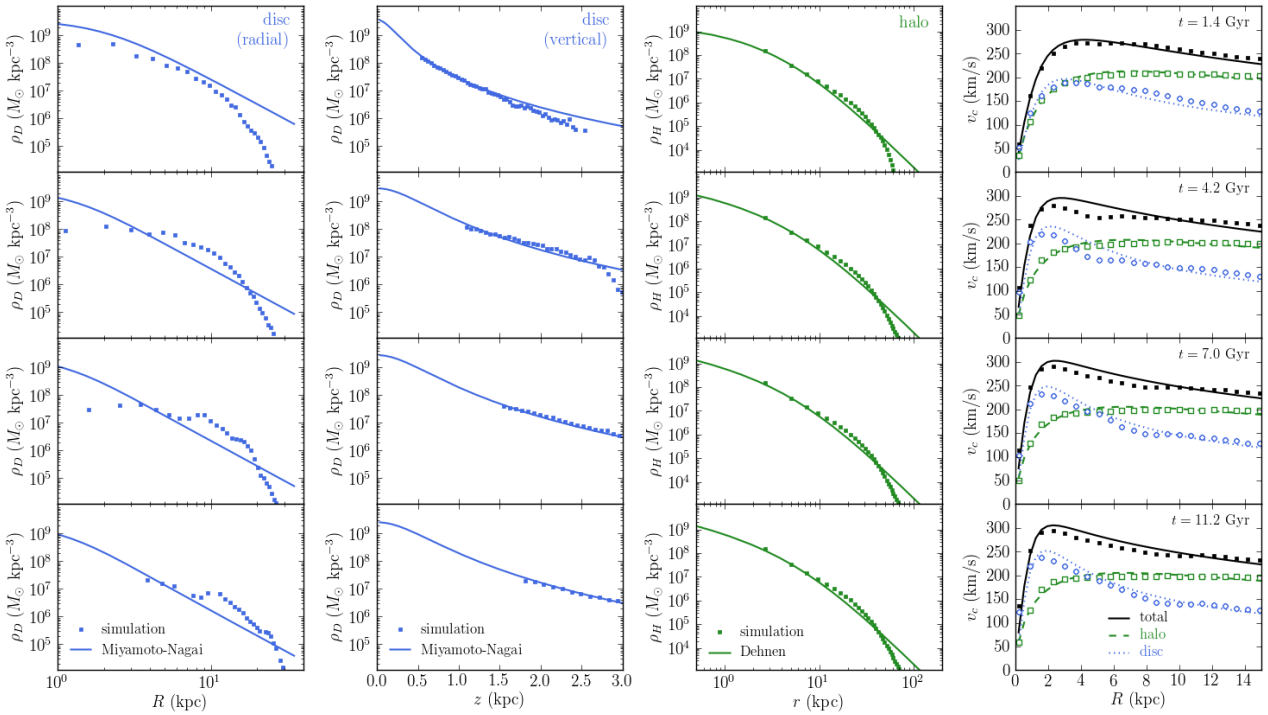

Figure 1.3: (Colour online) Parameters of the Dehnen halo profile and of the Miyamoto–Nagai disc are obtained by fitting the circular velocity curves at each time. Here we display four different times. The fourth column exhibits total, halo and disc circular velocity curves. The first and second columns show the disc density profiles (radial and vertical, respectively). The third column has the halo density profile. Points come from measurements of the N-body simulation, while lines are fitted profiles.

Fitting Eq. (1.9) to the measured halo rotation curve, we obtain a_H and γ. In the case of the disc, it is not enough to fit Eq. (1.8). One must simultaneously fit the Miyamoto–Nagai density profile to disambiguate the $A+B$ (ignoring the inner part of the disc). When fitting the disc rotation curve, we assume the total stellar mass (i.e. we take both disc and bar mass into account). Since the circular velocities rely on azimuthally averaged quantities, the presence of the bar does not greatly interfere with the quality of the fits, while its removal would lead to spurious results. The measured rotation curves (disc, halo and total), as well as the resulting fitted circular velocities, are displayed in the fourth column of Fig. 1.3 (at four illustrative instants in time). Errors in the fitted parameters of rotation curves were typically of about 5 per cent or less. Also shown in the first, second and third panels of Fig. 1.3, are the disc (radial and vertical) and halo density profiles. The points correspond to simulation measurements and the lines give the resulting fits.

One of the main arguments in favor of the adequacy of our analytical model is evidenced by the fact that its total rotation curves are in good agreement with those measured from the simulation. This indicates that the choices of profiles were not unreasonable, as they result in a globally similar gravitational potential. Even if individually the densities of the components are idealized simplifications, the similarity of the total potential ensures that the overall dynamical evolution should be sufficiently well approximated.

Finally, the resulting time evolution of the halo and disc structural parameters, measured in the manner described above, are displayed in the first to fourth panels of Fig. 1.2. With these, the time-dependence of the analytical model is fully specified. In Table 1 in [Manos and Machado 2014], we summarize the analytical model by showing a sample of parameters for the Ferrers bar, Miyamoto–Nagai disc and Dehnen halo potential as fitted by the N-body simulation, at four times.

Bar strength

In order to measure the bar strengths in analytical models, [Manos and Athanassoula 2011] had employed the Q_b parameter [R. Buta, Block, and Knapen 2003; R. Buta, Laurikainen, and Salo 2004], which is a measure of the relative strength of the non-axisymmetric forces. Here, we opt instead to use a method more familiar to N-body simulations, namely measurements of the $m = 2$ Fourier component of the mass distribution. For the N-body simulation, we measure this component straightforwardly as a function of radius and then take the maximum amplitude to be the A_2 (see e.g. [Athanassoula, Machado, and Rodionov 2013a]. We refer to this quantity as the *bar strength*.

For the analytical model, we proceed in a way that allows us to treat it as if it could be represented by particles. We extract from the simulation a random sample of 100 000 initial conditions (i.e. positions and velocities of disc particles) at a time $t_0 = 1.4$ Gyr, where we use this ensemble of orbits to further study dynamical trends). The orbits of each of these 'test particles' are then evolved forward in time in the presence of our time-dependent analytical potential. Their successive positions can be treated as if they were simulation particles. By stacking them at each time step, we produce the snapshots in the bottom row of Fig. 1.1. These mock snapshots display a striking resemblance to the N-body snapshots, specially bearing in mind that they were obtained by very indirect means. While this comparison cannot be expected to yield a perfect morphological equivalence, one notices that the bar lengths are in quite good agreement, and that in both cases rings are present (although not of the same extent). The point is that the dynamics that arises from the analytical model will give rise to very similar disc and bar morphologies. In fact, the relative importance of the bar is also quite comparable, as indicated by the A_2 parameter. Analogously to the N-body case, we compute the A_2 of these mock snapshots and compare them in Fig. 1.4.

We must stress here that this comparison is an *a posteriori* verification, i.e. the bar strength of the N-body simulation was in fact not used as an input to the analytical model. The fact the A_2 do agree well counts as a further sign of the consistency of the constructed analytical model.

It is clear, of course, that the variation of the bar strength modifies the values of several parameters and yields richer information about the dynamics of a self-consistent model. N-body simulations show that in general, variations of the bar mass also change the mass ratios of the model's components, the bar shape and the pattern speed of the galaxy. Hence, if one wishes to use a mean field potential to 'mimic' a self-consistent model as accurately as possible, one should allow for all the parameters that describe the bar (together with all other axisymmetric components) to depend on time, assuming that the laws of such dependence were explicitly known. In our case, however, we adopt a simpler approach and vary only the masses of the bar and the disc, as a first step towards investigating such models when time-dependent parameters are taken into account. Thus, we do not pretend to be able to reproduce the exact dynamical evolution of a realistic galactic simulation. Rather, we wish to understand the effects of time dependence on the general features of barred galaxy models and compare the efficiency of chaos indicators like the GALI method and the Maximal Lyapunov Exponent (MLE) in helping us unravel the secrets of the dynamics in such problems.

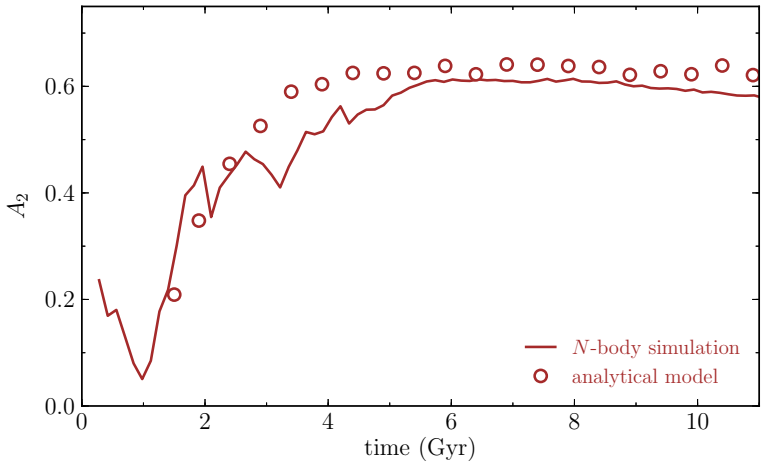

Figure 1.4: Bar strength, measured from the simulation (line) and from the analytical model (points). A_2 is the maximum relative contribution of the $m = 2$ Fourier component of the mass distribution in the disc.

We stress that the method we introduced to construct the analytical model does not rely – at all – on frozen potentials. Instead, it is grounded on the detailed features of a fully time-dependent, self-consistent N-body simulation.

Unless otherwise stated, the units of the analytical model are given as: 1 kpc (length), 1000 km$\cdot$ sec^{-1} (velocity), 1 Myr (time), $2 \times 10^{11} M_{\odot}$ (mass) and km$\cdot$ sec$^{-1}\cdot$ kpc^{-1} (Ω_b) while the parameter $G = 1$. The total mass $M_{tot} = M_B(t) + M_D(t) + M_H$ is set equal to $3 \times 10^{11} M_{\odot}$ and since the halo's mass M_H is kept constant, the disc's mass $M_D(t)$ is varied as $M_D(t) = M_{tot} - (M_H + M_B(t))$.

1.3 Chaos detection techniques

Let us briefly recall how the two main chaos detection methods used throughout the manuscript, namely the GALI and the MLE, are defined and calculated. Considering the following TD 3-d.o.f. Hamiltonian function which determines the motion of a star in a 3 dimensional rotating barred galaxy:

$$H = \frac{1}{2}(p_x^2 + p_y^2 + p_z^2) + V(x, y, z, t) - \Omega_b(t)(xp_y - yp_x). \tag{1.10}$$

The bar rotates around its z–axis (short axis), while the x direction is along the major axis and the y along the intermediate axis of the bar. The p_x, p_y and p_z are the canonically conjugate momenta, V is the potential, $\Omega_b(t)$ represents the pattern speed of the bar and H is the total energy of the orbit in the rotating frame of reference (equal to the Jacobi constant in the TI case).

The corresponding equations of motion are:

$$\begin{aligned}
\dot{x} &= p_x + \Omega_b(t) y, \\
\dot{y} &= p_y - \Omega_b(t) x, \\
\dot{z} &= p_z, \\
\dot{p_x} &= -\frac{\partial V}{\partial x} + \Omega_b(t) p_y, \\
\dot{p_y} &= -\frac{\partial V}{\partial y} - \Omega_b(t) p_x, \\
\dot{p_z} &= -\frac{\partial V}{\partial z},
\end{aligned} \tag{1.11}$$

while the equations governing the evolution of a deviation vector $\mathbf{w} = (\delta x, \delta y, \delta z, \delta p_x, \delta p_y, \delta p_z)$ needed for the calculation of the MLE and the GALI, are given by the variational equations:

$$\begin{aligned}
\dot{\delta x} &= \delta p_x + \Omega_b(t) \delta y, \\
\dot{\delta y} &= \delta p_y + \Omega_b(t) \delta x, \\
\dot{\delta z} &= \delta p_z, \\
\dot{\delta p_x} &= -\frac{\partial^2 V}{\partial x \partial x}\delta x - \frac{\partial^2 V}{\partial x \partial y}\delta y - \frac{\partial^2 V}{\partial x \partial z}\delta z + \Omega_b(t)\delta p_y, \\
\dot{\delta p_y} &= -\frac{\partial^2 V}{\partial y \partial x}\delta x - \frac{\partial^2 V}{\partial y \partial y}\delta y - \frac{\partial^2 V}{\partial y \partial z}\delta z - \Omega_b(t)\delta p_x, \\
\dot{\delta p_z} &= -\frac{\partial^2 V}{\partial z \partial x}\delta x - \frac{\partial^2 V}{\partial z \partial y}\delta y - \frac{\partial^2 V}{\partial z \partial z}\delta z.
\end{aligned} \tag{1.12}$$

Regarding the estimation of the value of the MLE, λ_1, of an orbit under study we follow numerically its evolution in time together with its deviation vectors $\mathbf{w}$, by solving the set of Eqs. (1.11) and (1.12) respectively. For this task we use a Runge-Kutta method of order 4 with a sufficiently small time step, which guarantees the accuracy of our computations, ensuring the relative errors of the Hamiltonian function (in the TI case) are typically smaller than 10^{-6}. Furthermore, we need to have a fixed time step in order to ensure that in the TD case the orbits vary simultaneously with the potential.

In general, the derivatives of the potential V depend explicitly on time and the ordinary differential equations (ODEs) [Eqs. (1.11)] are non-autonomous. Hence, one has to solve together the equations for the deviation vectors [Eqs. (1.12)] with the equations of motion [Eqs. (1.11)]. Transforming the Eqs. (1.11), and consequently [Eqs. (1.12)], to an equivalent autonomous system of ODEs by considering time t as an additional coordinate (see e.g. section 1.2b [Lichtenberg and Lieberman 1992]), is not particularly helpful, and is better to be avoided as shown in [Grygiel and Szlachetka 1995].

So, in order to compute the MLE and the GALI we numerically solve the time-dependent set of ODEs [Eq,. (1.11) and (1.12)]. Then, according to [Benettin, Galgani, and Strelcyn 1976; Contopoulos, Galgani, and Giorgilli 1978; Benettin, Galgani, Giorgilli, et al. 1980] the MLE λ_1 is defined as:

$$\lambda_1 = \lim_{t \to \infty} \sigma_1(t), \tag{1.13}$$

where:

$$\sigma_1(t) = \frac{1}{t} \ln \frac{\|\mathbf{w}(t)\|}{\|\mathbf{w}(0)\|}, \tag{1.14}$$

is the so-called 'finite time MLE', with $\|\mathbf{w}(0)\|$ and $\|\mathbf{w}(t)\|$ being the Euclidean norm of the deviation vector at times $t = 0$ and $t > 0$ respectively. A detailed description of the numerical algorithm used for the evaluation of the MLE can be found in [C. Skokos 2010].

This computation can be used to distinguish between regular and chaotic orbits, since $\sigma_1(t)$ tends to zero (following a power law $\propto t^{-1}$) in the former case, and converges to a positive value in the latter. But the Hamiltonian [Eq. 1.10)] is TD in this case, which means that its orbits could change their dynamical behavior from regular to chaotic and vice versa, over different time intervals of their evolution. In such cases, the MLE (1.13) does not behave exactly as in TI model (presenting in general stronger fluctuations) and its computation might not be able to identify the various dynamical phases of the orbits, since by definition it characterizes the asymptotic behavior of an orbit (see e.g. [Manos, T. Bountis, and C. Skokos 2013] and also [T. Bountis, Manos, and Christodoulidi 2009; Manos and Ruffo 2011; Moges, Manos, and Ch. Skokos 2020] for some relevant applications). Nevertheless, we will show the MLE for a number of orbits throughout the paper, for a more global discussion of the several dynamical properties observed.

Thus, in order to avoid such problems in our study, we use the GALI method of chaos detection [C. Skokos, T. C. Bountis, and C. Antonopoulos 2007]. The GALI index of order k (GALI_k) is determined through the evolution of $2 \leq k \leq N$ initially linearly independent deviation vectors $\mathbf{w}_i(0)$, $i = 1, 2, \ldots, k$, with N denoting the dimensionality of the phase space of our system. Thus, apart from solving Eqs. (1.11), which determines the evolution of an orbit, we have to simultaneously solve Eqs. (1.12) for each one of the k deviation vectors. Then, according to [C. Skokos, T. C. Bountis, and C. Antonopoulos 2007], GALI_k is defined as the volume of the k-parallelogram having as edges the k unit deviation vectors $\hat{\mathbf{w}}_i(t) = \mathbf{w}_i(t)/\|\mathbf{w}_i(t)\|$, $i = 1, 2, ..., k$. It can be shown, that this volume is equal to the norm of the wedge product (denoted by $\wedge$) of these vectors:

$$\mathrm{GALI}_k(t) = \| \hat{\mathbf{w}}_1(t) \wedge \hat{\mathbf{w}}_2(t) \wedge \ldots \wedge \hat{\mathbf{w}}_p(t) \| \,. \tag{1.15}$$

We note that in the above equation the k deviation vectors are normalized but their directions are kept intact.

In principal and for TI systems, the $\mathrm{GALI}_k(t)$ for regular orbits remains practically constant and positive if k is smaller or equal to the dimensionality of the torus on which the motion occurs, otherwise, it decreases to zero following a power law decay. For the chaotic ones, all $\mathrm{GALI}_k(t)$ tend exponentially to zero with exponents that depend on the first k LEs of the orbit [C. Skokos, T. C. Bountis, and C. Antonopoulos 2007; C. Skokos, T. Bountis, and C. Antonopoulos 2008]. Nevertheless, in the TD case studied in [Manos, T. Bountis, and C. Skokos 2013] and also here, the way the theoretical estimation of the GALI's exponential rates are strongly related to the LEs, being more complicated and still open to further inquiry.

The procedure used for the detection of the several different dynamical epochs of the TD system is the following: We evolve the GALI_k with $k = 2$ or $k = 3$ (i.e., using 2 or 3 deviation vectors) for the 2-d.o.f or 3-d.o.f. cases respectively and whenever GALI_k reaches very small values (i.e. $\mathrm{GALI}_k \leq 10^{-8}$) we re-initialize its computation by taking again k new random orthonormal deviation vectors, which resets the $\mathrm{GALI}_k = 1$. We allow then these vectors to evolve under the current dynamics. For time intervals where the index decays exponentially corresponds to chaotic epochs while in the other cases to non-chaotic. The reason in doing this is that we need to follow the current dynamical stability of an orbit under-study which in principle can interplay between chaotic and regular for different epochs during the total time evolution. Thus, let us assume that a trajectory experiences chaotic dynamics and later on drifts to a regular regime. The volume formed by the deviation vectors will first shrink

exponentially to very small values and remain small throughout the whole evolution unless one re-initializes the deviation vectors and their volume, in order to allow them to 'feel' the new current dynamics. However, when we are interested in more general dynamical trends in time (less details), we will fix time intervals and we will re-initialize the deviation vectors in the beginning of each one.

1.4 Results

The 2 D.O.F. Time-Independent Case

Shedding some light on the underlying TI dynamics is an important step for understanding the more complicated case of the fully 3-d.o.f. TD model where all parameters vary simultaneously in time. By setting z, p_z equal to zero at $t = 0$ (remaining zero at all times) in the Hamiltonian Eq. (1.10), the orbits' motion is then restricted in the 2 dimensional (x, y) space. Note that here $t = 0$ refers to the $t_0 = 1.4$ Gyr of the N-body simulation. We can then study, in a frozen potential, individual orbits and the stability of the phase space, in terms of detecting and locating chaotic and regular motion, for the several sets of the potential parameters at deferent times, as derived from the N-body simulation. We shall begin by choosing fixed parameters from four time snapshots, i.e., at $t = 1.4$ Gyr, $t = 4.2$ Gyr, $t = 7.0$ Gyr and $t = 11.2$ Gyr and we integrate orbits for 10 Gyr.

In Fig. 1.5, we present the Poincaré Surface of Section (PSS) defined by $x = 0$, $p_x \geq 0$ with $H = -0.19$, for three typical orbits being integrated for 10 Gyr. The set of parameters for the bar, disc and halo components are chosen from the fits with the 3-d.o.f. TD Hamiltonian at $t = 7.0$ Gyr of the N-body simulation (see see Table 1 in [Manos and Machado 2014] for more details). The blue $(*)$ points on the PSS correspond to a disc regular orbit, forming a curve by the successive intersections with the plane $x = 0$, having initial condition $(y, p_y) = (-1.5, 0.0)$ with $x = 0$ and $p_x = H(x, y, p_y)$ (called 'DR' from now on). Its projection on the (x, y)-plane is shown in the top left inset panels of Fig. 1.5 and coloured in blue. The $GALI_2$ for this orbit confirms that its motion is regular by oscillating to a positive value during its evolution in time as well as the MLE σ_1 following a power law decay [see second and third top inset panels of Fig. 1.5 respectively (blue), note that the axis here are in lin-log scale]. The three small black curves in the central part of Fig. 1.5, marked with $(\times)$, are formed by the successive intersections of an initial condition with $(y, p_y) = (-0.4, 0.0)$ (we will call it 'BR'). From its projection on the (x, y)-plane [first bottom inset panel of Fig. 1.5 (black)], it is evident that it is a bar-like orbit elongated along the long x-axis. It surrounds a stable periodic orbit of period 3 in the center of these islands and its regular dynamics is clearly revealed from the evolution of the $GALI_2$ and the MLE σ_1 evolution [second and third top (black) inset panels of Fig. 1.5 respectively, note that the axis are again in lin-log scale]. The central scattered red points on the PSS, marked with $(+)$, correspond to a chaotic orbit with initial condition $(y, p_y) = (2.5, 0.0)$ (called 'DC' from now on). In the three inset panels positioned vertically in the right part of the Fig. 1.5 (red), we depict its projection on the (x, y)-plane (top panel). Its $GALI_2$ successive and exponential decrease to zero in time (middle panel) indicates its chaotic nature. Notice that we re-initialize the deviation vectors each time the index becomes small $(\leq 10^{-8})$. Its MLE σ_1, as expected, converges to a positive value (bottom inset).

Exploiting this information, we first choose a sample of 2-d.o.f. Hamiltonian function values (for the four times mentioned above and the respective sets of parameters), from the interval of energies where the majority of the N-body simulation's particles is more probable to be found. From this

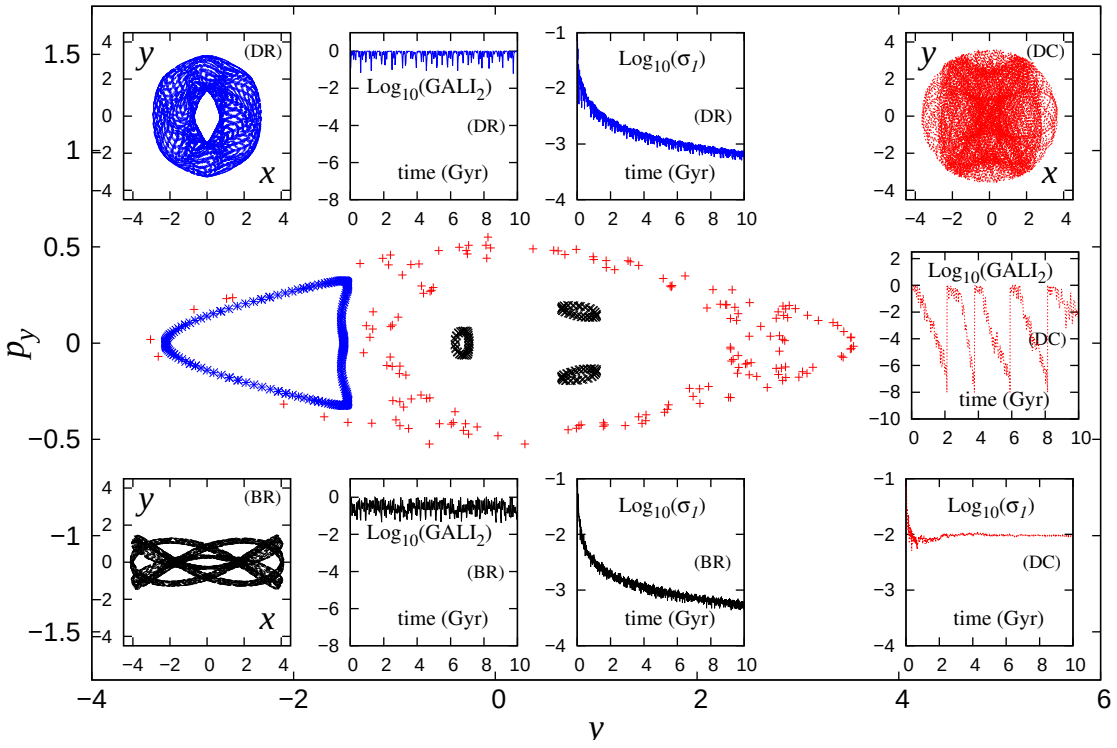

Figure 1.5: The Poincaré Surface of Section defined by $x = 0$, $p_x \geq 0$ with $H = -0.19$, for three typical orbits (two regular and one chaotic) being integrated for 10 Gyr. The set of parameters for the bar, disc and halo components are chosen from the fits with the 3-d.o.f. TD Hamiltonian at $t = 7.0$ Gyr of the N-body simulation. In the insets we depict their projection on the (x, y)-plane together with the $GALI_2$ and MLE σ_1 evolution in time (see Table 1 in [Manos and Machado 2014] for the exact parameters).

sample, we select a subset of representative energies to illustrate typical phase space structures, focusing at this point on the underlying dynamics. Then, we chart the regular and chaotic regimes of the phase space with $GALI_2$. In Fig. 1.6, we have used a grid of 100 000 initial conditions on the (y, p_y)-plane of the corresponding PSS and we have constructed a chart of the chaotic and regular regions similar to the PSS, but with more accuracy and higher resolution, in a similar manner just like in [Manos and Athanassoula 2011], using the $GALI_2$ method. The different colour corresponds to the different final value of the $GALI_2$ after 10 Gyr (10 000 time units) for orbits representing each cell of the grid. The yellow colour corresponds to regular orbits (and areas) where the $GALI_2$ oscillates around to relatively large positive values, the black color represents the chaotic orbits where $GALI_2$ tends exponentially to zero (10^{-16}), while the intermediate colors in the colour-bars between the two represent 'weakly chaotic or sticky' orbits, i.e. orbits that 'stick' onto quasi-periodic tori for long times but their nature is eventually revealed to be chaotic. Note that the model in this case is TI and hence there is no need for re-initialization of the deviation vectors, since the asymptotic dynamical nature of the orbits does not change in time. The first row refers to a set of potential parameter given at $t = 1.4$ Gyr for Hamiltonian values $H = -0.31, -0.28, -0.25, -0.22$, the second row at $t = 4.2$ Gyr for $H = -0.28, -0.25, -0.22, -0.19$, the third row at $t = 7.0$ Gyr for $H = -0.28, -0.25, -0.22, -0.19$ and the fourth row at $t = 11.2$ Gyr for $H = -0.28, -0.25, -0.22, -0.19$.

Using the above approach, we can measure and quantify the variation of the percentage of regular orbits in the phase space as the total energy increases for a specific choice of potential parameters at same fixed times. The chosen values of the Hamiltonian functions cover the range of the available energy interval up to the value of the escape energy which in general is different. Although the main general trend is that this percentage decreases as the energy grows, its behavior changes at high energy values where it is no more monotonic. Note that this happens for energy values $H > -0.19$ out of the range of N-body simulation orbits. In Fig. 1.7 we show the variation of percentages of regular motion as a function of the energy H for the different sets of parameters at $t = 1.4$ Gyr, $t = 4.2$ Gyr, $t = 7.0$ Gyr and $t = 11.2$ Gyr. The threshold $GALI_2 \geq 10^{-8}$ was used to characterize an orbit as regular and $GALI_2 < 10^{-8}$ as chaotic which will also be the chaos criterion/threshold throughout this paper. We should emphasize that these percentages refer to a set of initial conditions that cover uniformly the whole 2-d.o.f. phase space. On the other hand, an ensemble of trajectories extracted from the N-body simulation does not necessarily populate 'democratically' the phase space. By simply inspecting these percentages one can claim that the fraction of regular motion is systematically larger for later times, and for all energies. When looking and comparing the phase space for early times, i.e., $t = 1.4, 4.2$ Gyr (first and second row) and late times, i.e., $t = 7.0, 11.2$ Gyr (third and fourth row) in Fig. 1.6, we may see that the central island of stability, originating bar-like orbits, is becoming larger as the time grows and this is even more evident for the relatively larger energies (see the third and fourth row from top to bottom). This indicates that the bar component becomes gradually more important and dominant.

The 3 D.O.F. Time-Dependent Case

In Fig. 1.8 we show the evolution of an orbit from the ensemble of the N-body simulation with initial condition:

$$(x, y, z, p_x, p_y, p_z) \approx (-4.543100, 0.499639, -0.162627, 0.048798, -0.218718, 0.002898)$$

(we will refer to this orbit from now on as $B1$), which is iterated for 10 Gyr (10 000 time units) for

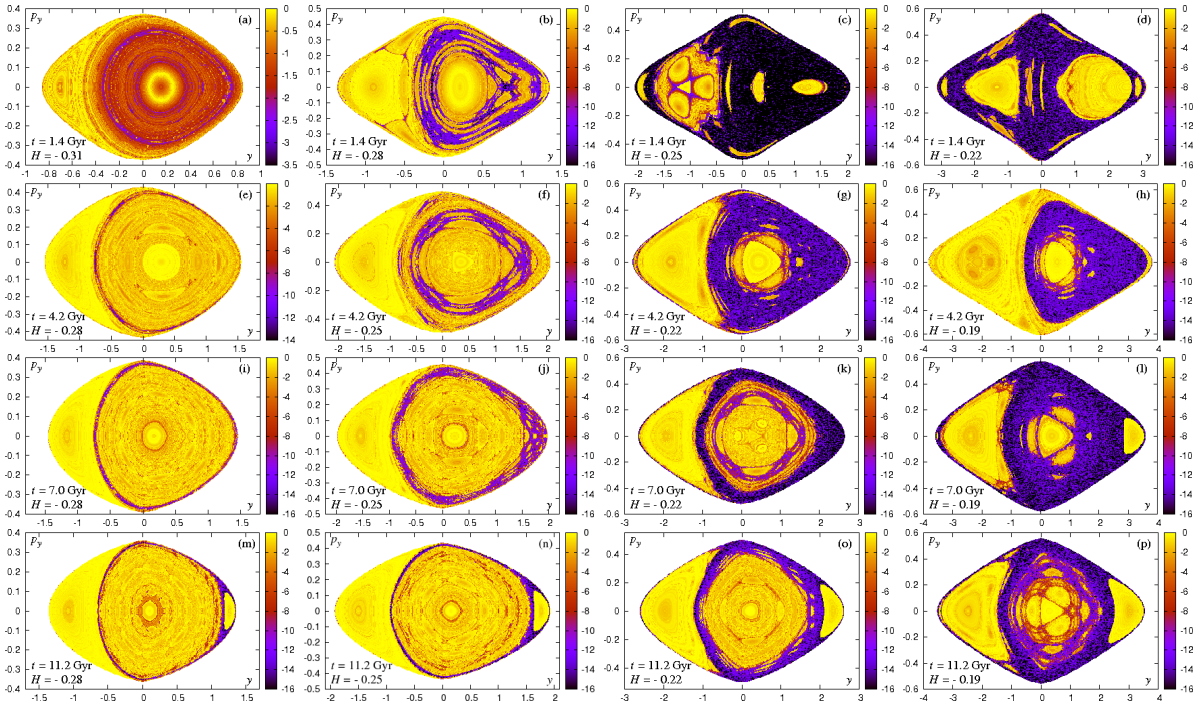

Figure 1.6: The (in)stability map for the 2-d.o.f. frozen potential case using a grid of $\approx$ 100 000 initial conditions on the PSS and integrating them for 10 Gyr. The colour-bar represents the final $GALI_2$ values of each initial condition in the end of the iteration. The first row refers to a set of potential parameter given at $t = 1.4$ Gyr for Hamiltonian values $H = -0.31, -0.28, -0.25, -0.22$, the second row at $t = 4.2$ Gyr for $H = -0.28, -0.25, -0.22, -0.19$, the third row at $t = 7.0$ Gyr for $H = -0.28, -0.25, -0.22, -0.19$ and the fourth row at $t = 11.2$ Gyr for $H = -0.28, -0.25, -0.22, -0.19$. The yellow (light-grey in b/w) colour corresponds to regular orbits where the $GALI_2$ oscillates around to relatively large positive values, the black color represents the chaotic orbits where $GALI_2$ tends exponentially small values, while the intermediate colors in the colour-bars between the two represent 'weakly chaotic or sticky' orbits. The exact set of parameters used at each $t = 1.4, 4.2, 7.0, 11.2$ Gyr are given in [Manos and Machado 2014] (Table 1).

the TD potentials mentioned above. The starting and complete set of parameters for the TD model is taken at $t_0 = 1.4$ Gyr by the fits with the N-body simulation. Note that in all figures' panels, we set everywhere the t_0 equal to zero instead of $t_0 = 1.4$ Gyr.

In the first row of the first block in Fig. 1.8(a,b,c,d), we show its projection on the (x, y)-plane for four successive time intervals of $\Delta t = 2.5$ Gyr, i.e., all the three potential components V_B, V_D, V_H are time-dependent and the total energy is not in general conserved. The colour bar next to each panel corresponds to the time (in Gyr), hence the most recent epochs of the orbit are coloured with yellow while those in the earlier ones with dark blue or black. In Fig. 1.8(e) we show its $GALI_3$, capturing accurately the chaotic nature of the orbit during the first [Fig. 1.8(a)], third [Fig. 1.8(c)] and fourth [Fig. 1.8(d)] time windows by decaying exponentially to zero. On the other hand, in the second [Fig. 1.8(b)] time window its regular (even by just looking its projected morphologically on the (x, y)-plane) behaviour is successfully revealed by the fluctuates to a non-zero value of the

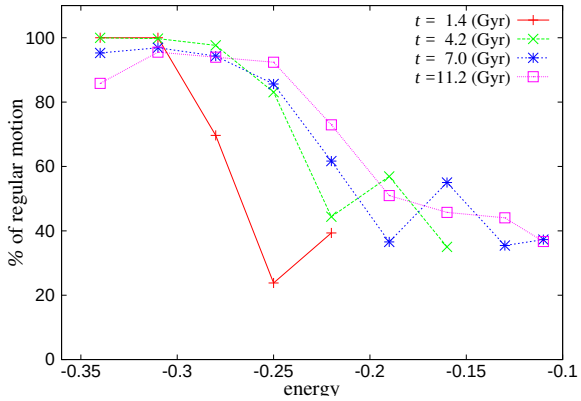

Figure 1.7: Percentages of regular motion for the 2-d.o.f. frozen case as a function of the energy H for the different sets of parameters at $t = 1.4$ Gyr, $t = 4.2$ Gyr, $t = 7.0$ Gyr and $t = 11.2$ Gyr.

index. Note that the plot is in lin-log scale and the deviation vectors are re-initialized, by taking again k new random orthonormal deviation vectors, each time the GALI_3 becomes very small (i.e. $\mathrm{GALI}_3 \leq 10^{-8}$). It turns out that the $B1$ begins as a regular disc-like orbit during the first 2.5 Gyr and, as the bar starts forming and growing, it gradually evolves to a chaotic bar-like orbit until the end of the integration. We may notice how hard it is for the finite time MLE σ_1 [Fig. 1.8(f)] to capture these different dynamical different transitions and epochs due to its time-averaged definition (see also [Manos, T. Bountis, and C. Skokos 2013]). Furthermore, its power law decay for regular time intervals and its tendency to positive values for chaotic ones are of the same order of magnitude making it rather hard to use the temporary value σ_1 as a safe criterion of regular and weak or strong chaotic motion.

In Fig. 1.9, and in a similar manner as in Fig. 1.8, we show another characteristic disc-like orbit for most of the total of integration with initial condition:

$$(x, y, z, p_x, p_y, p_z) \approx (-5.14416, -1.345540, 0.277956, 0.140120, -0.219648, 0.000338)$$

(we will refer to this orbit from now on as '$D1$'). The evolutionary scenarios are again the same as before, i.e., in the first row of the first block in Fig. 1.9(a,b,c,d), we present its projection on the (x, y)-plane for different time windows. The $D1$ orbit experiences a regular epoch during its first 2.5 Gyr, then gradually becomes chaotic switching to a bar-like shape and finally becomes a chaotic but disc-like now orbit. Its regular and chaotic epochs are accurately captured by the GALI_3 [Fig. 1.9(e)], fluctuating to constant value for the first 2.5 Gyr and then successively decaying exponentially to zero for the rest of the integration. The MLE σ_1 [Fig. 1.9(f)] also reveals this dynamical evolution, by decaying with a power law for the regular part and converging to non-zero value for the three last time windows. However, here the motion does not present any further transition and/or interplay between regular and chaotic motion and again (as for the $B1$ orbit) the order of magnitude for the σ_1 is not varying sufficiently enough to lead to a safe conclusion at certain times without seeing its whole time evolution.

In [Manos and Machado 2014], it was found that the overall fraction of chaotic motion in the disc decreases as the bar grows stronger. Figure 1.10 indicates the tight correlation between the decrease

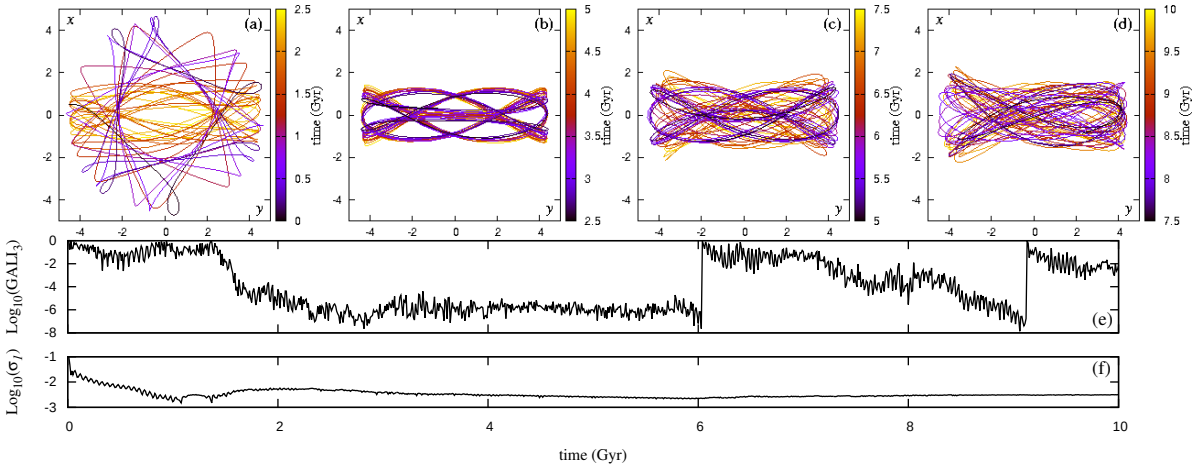

Figure 1.8: The 3-d.o.f. orbit $B1$ different projection on the (x, y)-plane in different time windows is depicted in the first (four-panel) row (from top block-part to the bottom respectively) and the colour bar corresponds to the time (in Gyr). Its $GALI_3$ and MLE σ_1 evolution in time is shown just below them. Note that the orbit starts as a disc-like and gradually its shape turns to barred, displaying the bar's growth through the parameters of the Ferrers' potential.

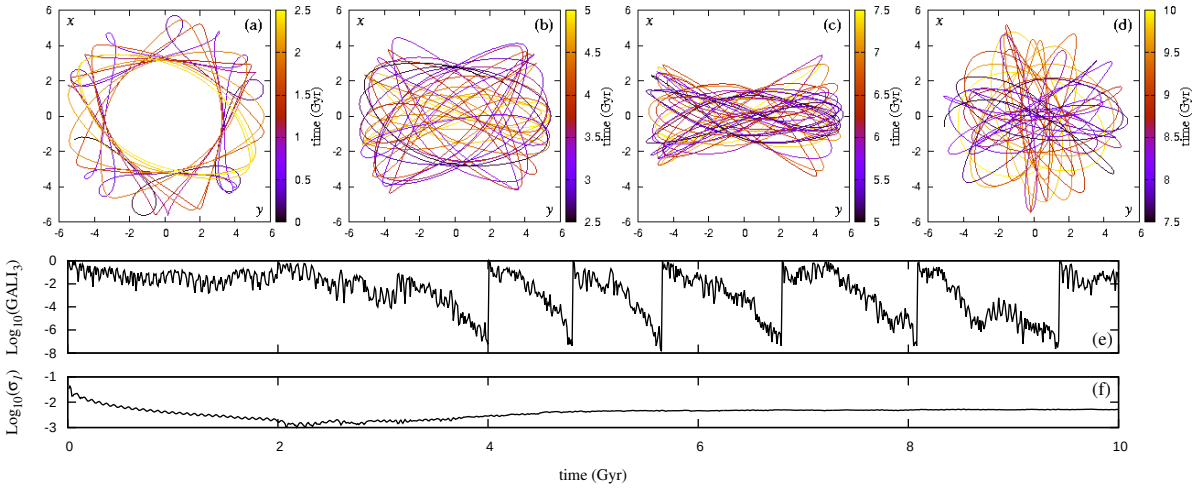

Figure 1.9: Same as in Fig. 1.8 but for the 3-d.o.f. disc-like orbit $D1$. Note, that here the disc-like pattern slightly varies from cases to case. The *different degree of chaoticity* can be accurately captured by the frequency and fast decay to zero of the $GALI_3$ [Fig. 1.9(e)], indicating that the orbits is relatively 'strongly chaotic' . This information can not be revealed in such a way by the MLE σ_1 shown in Figs. 1.9(f).

in chaos and the growth of the bar, as indicated by the fraction of chaotic motion – measured within the bar – as a function of relative bar mass (i.e. the bar-to-disc mass ratio). One also notices that

most of the disappearance of chaos takes place during the first half of the evolution, which is the period of more intense bar growth.

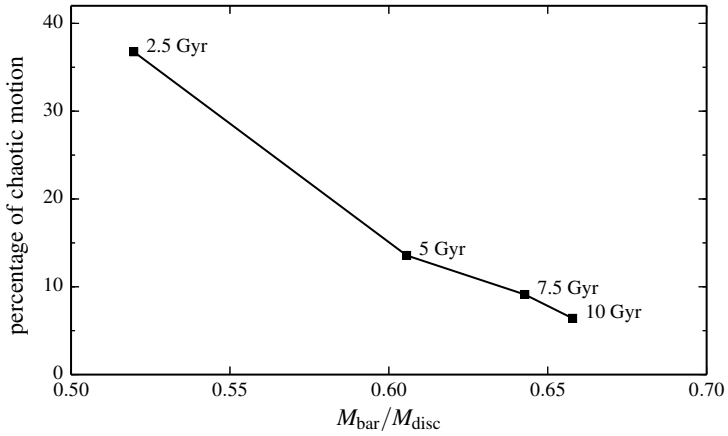

Figure 1.10: Fraction of chaotic motion within the bar as a function of relative bar mass.

If bar growth is partially driving the rise of regular motion, the question then arises as to the spatial distribution of regular versus chaotic motions. In which regions of the stellar disc are regular and chaotic motion predominantly found? Is the global rise of regularity accompanied by some spatially localized increase of chaos? In order to address such questions, we define four distinct morphological regions: (i) the bar; (ii) the ring; (iii) the intermediate low-density region between the bar and the ring, referred to as the *gap* region, for brevity; and (iv) the outer disc. These regions are selected somewhat arbitrarily (via visual inspection of the morphology), but they do reflect distinctive structural components, regarding density, as can be seen in the two upper rows of Fig. 1.11 with face-on and edge-on views, where the ellipses used to define them are shown.[1]

To explore the spatially resolved evolution of chaos throughout the stellar disc, we resort to the analysis of an ensemble of orbits. From the N-body simulation, we select a sample of 1×10^5 disc particles at the time $t_0 = 1.4$ Gyr where the bar has already started to be formed and starts growing from that point on. Then, their coordinates are used as an ensemble of initial conditions to be evolved in the presence of the time-dependent analytical potential. We evolve these orbits for 10 Gyr and study their dynamical behaviour. In order to avoid confusion, from now on we reset the t_0 to be zero (starting point of our simulations). We divide the total integration time in four intervals of $\Delta t = 2.5$ Gyr, re-initializing the GALI_3 index at the beginning of each window [Manos and Machado 2014]. The orbit is considered regular (non-chaotic) if its GALI_3 remains greater than 10^{-8} during a given time window; and it is considered chaotic if it reaches $\mathrm{GALI}_3 \leq 10^{-8}$. In this manner, we are able to compute fractions of chaotic motion within each time window. Additionally, at a given instant in time, we can also compute spatially resolved chaos fractions in different regions of the disc.

A global picture of the spatial distribution of regular and chaotic motion in the disc can be seen in the two bottom rows of Fig. 1.11, which displays the face-on and edge-on views of the ensemble of disc particles at the end of each time window, coloured by the GALI_3 index (being chaotic towards the

[1] In Fig. 1.11 and in all other such projections, the particles and orbits are displayed in the reference frame that rotates with the bar. Thus, the bar major axis always lies along the direction of the x-axis.

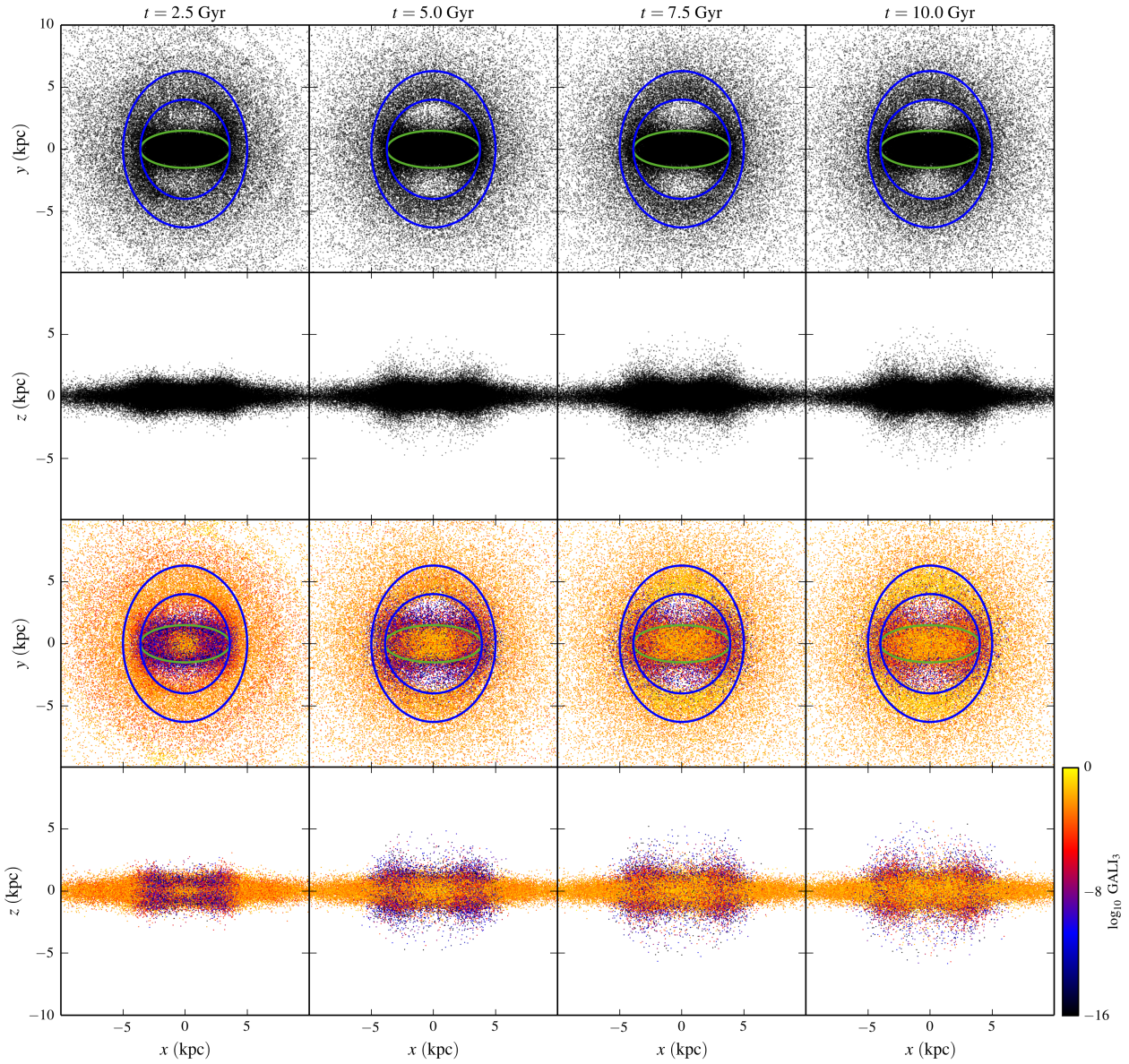

Figure 1.11: Upper rows: face-on and edge-on views of the ensemble of orbits at the end of each time window. Lower rows: face-on and edge-on views of projected $GALI_3$ indices for the disc ensemble. Chaotic orbits are those with $GALI_3 \leq 10^{-8}$. The face-on views also display the ellipses used to define the regions referred to as: bar, ring, gap and outer disc. Each frame is 20 kpc wide, and the particles are displayed in the reference frame that rotates with the bar.

blue, and regular towards the yellow). Some major results are already noticeable even by eye. First, the striking decrease of chaos within the bar region can be clearly seen. Secondly, even though the gap is a very low density region, it seems to hold a good portion of the chaotic orbits. Third, the outer disc – as well as the ring, to a degree – seem quite dominated by regular motion. Finally, another outstanding feature is the peanut-shaped view of the bar seen in the edge-on projection (sometimes

called X-shaped bulge). Remarkably, particles that depart considerably from the $z = 0$ plane are mostly chaotic.

In order to quantify in more detail these results, we measure the fraction of chaotic orbits as a function of time in each region (i.e. at the end of each time window, we obtain the number of particles having $\mathrm{GALI}_3 \leq 10^{-8}$ in a region divided by the total number of particles within that region). The result is shown in Fig. 1.12. The fraction of chaotic motion within the bar drops from nearly 40 per cent to less than 10 per cent. The outer disc remains essentially regular, with a non-zero but negligible appearance of chaos throughout the evolution. The fact that the ring region undergoes an initial increase in chaos can be ascribed in good measure to the edges of the bar. The gap region displays some interesting behaviour. Between the first and second time windows, the gap becomes depleted in terms of total number of particles, but at the same time its fraction of chaotic motion increases. From then on, it decreases, but the gap continues to be the region holding the highest local fraction of chaotic motion in the disc. The large amount of chaotic motion seen in the gap region is not unexpected. In fact it is well known that orbits that oscillate between the Lagrangian points L_1 and L_2 are unstable and therefore the transition zone between the bar and the disk is expected to be chaotic, see e.g. [Harsoula and Kalapotharakos 2009; Athanassoula, Romero-Gómez, and Masdemont 2009].

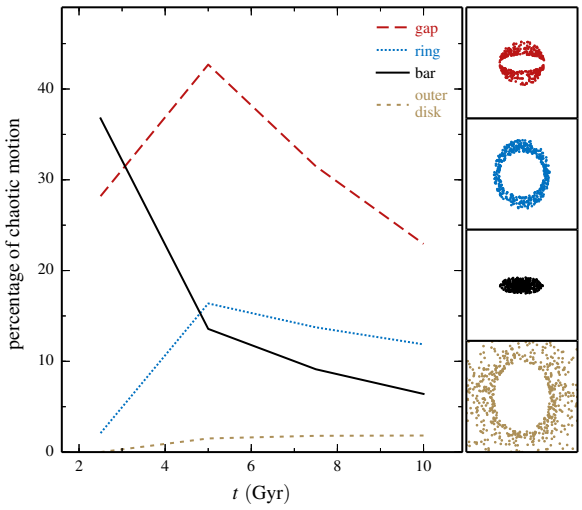

Figure 1.12: Fraction of chaotic motion as a function of time, measured within different regions of the disc. These regions are schematically indicated in the right-hand panels, and more clearly detailed in Fig. 1.11.

Instead of considering the state (chaotic or regular) of each particle at specific instants – the ends of the four time windows, we here account for the changes of their state. For example, one given orbit that was found to be regular at the end of the evolution might have been chaotic at the beginning, or it might have been continuously regular. In either case, where did such particles originate? Do the particles that change dynamical state (and those that don't) share a common locus at the beginning of the evolution? To explore these issues, we will examine separately the orbits that change dynamical behaviour and those that do not. This will allow us, in a sense, to map the origins and the destiny of

regular and chaotic motion.

By selecting those orbits which are permanently regular (64.3 per cent) and those which are permanently chaotic (only 0.9 per cent). The remainder (34.8 per cent) change their nature at least once during the evolution. Let us consider first those orbits that do not undergo any change of regime throughout the evolution (upper rows of Fig. 1.13).

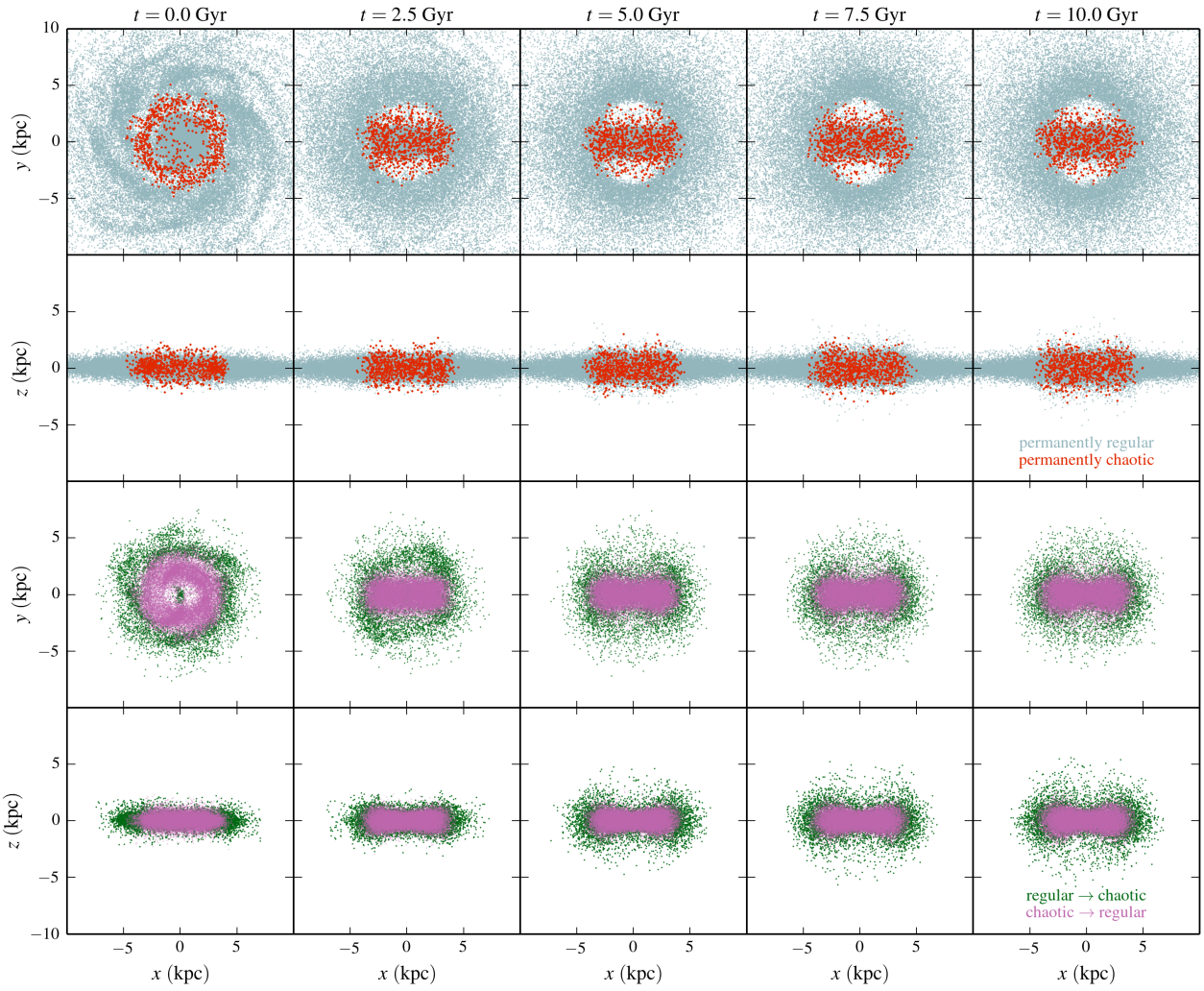

Figure 1.13: Evolution of regular/chaotic regimes separated in different configurations. Upper rows: face-on and edge-on vies of the orbits that are permanently regular (cyan), and those that are permanently chaotic (red). Bottom rows: face-on and edge-on views of the orbits that start regular and end chaotic (green), and those that start chaotic and end regular (purple).

Orbits that are permanently regular. As regards morphology, the permanently regular ones are qualitatively unremarkable, in the sense that they occupy almost any region of the galactic disc. There is thus little qualitative distinction between them and the entire ensemble and they merely map the normal evolution of the galactic disc as a whole. The only noticeable structures that are not quite covered by these orbits are the gap region, and, vertically, the peanut. (Due to the method employed

to create the initial conditions in the N-body simulation of [Machado and Athanassoula 2010], there is a residual transient seen as a vague spiral pattern at $t = 0$ and it subsides on a short time scale.)

Orbits that are permanently chaotic. The permanently chaotic orbits, on the the other hand, display peculiar features. They are tightly restricted to the region of the bar, and partially to the gap. Indeed, they spend nearly the entire evolution confined within this region. There is not one single permanently chaotic orbit to be found in the outer regions of the disc. At the instant $t = 0$, these particles – whose future destiny is to be permanently chaotic – are initially located within a reasonably well-defined ring, i.e. they are mostly found within $2\,\mathrm{kpc} < r < 4\,\mathrm{kpc}$.

For the remainder of the orbits, we will focus on two regimes: those that start regular and end chaotic (6.1 per cent), and those that start chaotic and end regular (20.8 per cent), regardless of the intermediate states (i.e. the transitions in the second and third time windows). Finally, there is a subset of orbits (7.9 percent) that do undergo two changes of regime, but nevertheless finish as they started; these will be disregarded. Let us consider now the two cases where the final state differs from the initial state (lower rows of Fig. 1.13):

Orbits that begin regular and end chaotic. These start at $t = 0$ from a similar locus as the permanently chaotic, but here the ring is slightly larger and more diffuse. This subset also includes some orbits very close to the origin ($r < 0.5$ kpc) in the beginning, which are not present in the permanently chaotic case. The volume occupied by these orbits contracts gradually, but they are more extended than the permanently chaotic ones, encompassing the region of the gap at later times as well. They are also vertically extended, being the major contributors to the structure of the peanut. In fact, this is the only subset of particles which significantly populates the peanut, in the regions of about $2.5\,\mathrm{kpc} < |z| < 5\,\mathrm{kpc}$ of height. The gap region, and mainly the peanut, are regions where chaos is important. However, it is only the initially regular – and finally chaotic – orbits that depart considerably from the plane. The orbits that were already chaotic from the beginning do not visit such heights.

Orbits that begin chaotic and end regular. Interestingly, the initial locus of this subset is approximately the complement of the previous case. Here, the orbits at $t = 0$ occupy the region internal to the ring defined by the previous case, while avoiding the very centre. In the third row of Fig. 1.13, the purple points overlap green points in the $t = 2.5 - 10$ Gyr frames. But in the $t = 0$ frame, the purple points fill precisely an empty region. Subsequently, the initially chaotic orbits evolve to be essentially part of the bar and end regular.

Origin and morphology of boxy orbits

Regular and chaotic two-dimensional and three-dimensional orbits of stars in such models of a galactic potentials provide with *boxy* orbital structures, which are the largest part of the bar galaxy component. *Boxiness* in the equatorial plane is associated either with quasi-periodic orbits in the outer parts of stability islands, or with sticky orbits around them, which can be found in a large range of energies. In the 3D barred models in [Patsis and Katsanikas 2014a; Patsis and Katsanikas 2014c] it has been suggested that *inner* boxy features can be built by means of quasi-periodic orbits at the edges of the stability islands of the x1 family, as well as with sticky orbits just beyond the last invariant torus around the stable x1 periodic orbit (see e.g. [Manos, C. Skokos, and C. Antonopoulos 2012] for applications of the GALI index for periodic orbits of different stability and their vicinity). It has been also proposed that such orbits support boxiness both in face-on, as well as in edge-on projections at the central region of the bar (about within half the way to the end of the bar). A similar dynamical

phenomenon was leading to the boxy features on the galactic plane in the bars of 2D barred-spiral models in [Tsigaridi and Patsis 2015]. By considering snapshots of the $N-$body simulation and for the orbital study we treat each snapshot independently, as an autonomous (TI) Hamiltonian system and calculate regular, sticky and chaotic orbits and hence examine the degree of chaoticity of the bar-supporting orbits.

In [Chaves-Velasquez et al. 2017], the location of *boxy* orbits in diagrams was indicated for certain TI analytical models for snapshots of the TD one. They are always found about the transition region from order to chaos. By perturbing such orbits in the vertical direction a class of 3D non-periodic orbits, which have *boxy* projections both in their face-on and side-on views, was found. Furthermore, the kind of orbits supporting *double boxy* morphologies in the successive snapshots was investigated, and the manner they evolve in time, i.e. from the model of the earlier snapshot to the model for the final one.

In a rotating Ferrers bar, the elliptical periodic orbits of the main families are characterized by a single non-zero initial condition along the minor axis of the bar, namely their position along the y-axis in our models. The curve of zero velocity (ZVC) in a (E_J, y_0) diagram separates the region where orbital motion is allowed from the region where it is not. Since the main family consists of direct periodic orbits, only the $y_0 > 0$ part of such a diagram is of interest for us. An (E_J, y_0) diagram is the projection of a complete (E_J, y_0, p_{y_0}) figure with all possible initial conditions. However, it is sufficient for describing the properties of the orbits we present below. The line that gives the y_0 initial condition of the main family of periodic orbits is the characteristic curve of the model. Since we want to study chaoticity in a large range of energies, we have created such (E_J, y_0) diagrams for the potentials of the three snapshots we study. In order to calculate the degree of chaoticity of the *planar* orbits around the main family of periodic orbit as we move from the center of the system towards corotation, we use the GALI_2 index. We have used the GALI_2 index to color-code each point in the allowed region in the (E_J, y_0) areas. The shade of the color indicates the GALI_2 index that a given orbit, i.e. a point in the (E_J, y_0) diagram, has at the end of the integration. In other words, the color of an (E_J, y_0) point indicates if the orbit with y_0 initial condition at E_J will lead to regular (large $\log_{10}(\mathrm{GALI}_2)$ values) or chaotic (very small $\log_{10}(\mathrm{GALI}_2)$ values) motion. At the borders between these regions we find points with intermediate $\log_{10}(\mathrm{GALI}_2)$ values, which correspond to sticky chaotic orbits.

In Fig. 1.14, we show the chaoticity of the planar orbits on the equatorial plane of a TI model based on the 2nd snapshot (at t=4.2 Gyr from Fig. 1.1). We sample the GALI_2 index at two time windows. First after time t_1, corresponding to 1 Gyr and then after time t_2, corresponding to 10 Gyr. In this way we investigate both the relatively short-term as well as the long-term behaviour of the orbits. Darker shades indicate more chaotic orbits. The color for each orbit is determined according to its $\log_{10}(\mathrm{GALI}_2)$ value and is taken from the colour bars given to the right of the figures.

1.5 Summary and outlook

The adequacy of the TD model and its verification is shown by (i) the similarity of the rotation curve with the one from the N-body simulation, ensuring the global dynamics are well approximated, (ii) the morphological similarity of the disc and bar features with those of the N-body simulation. and, (iii) the very good quantitative agreement of the length and strength of the bar in the resulting mock snapshots with the N-body bar. Such comparisons indicate that the TD model is able to adequately capture both the dynamics and the morphology of the barred galaxy model in question.

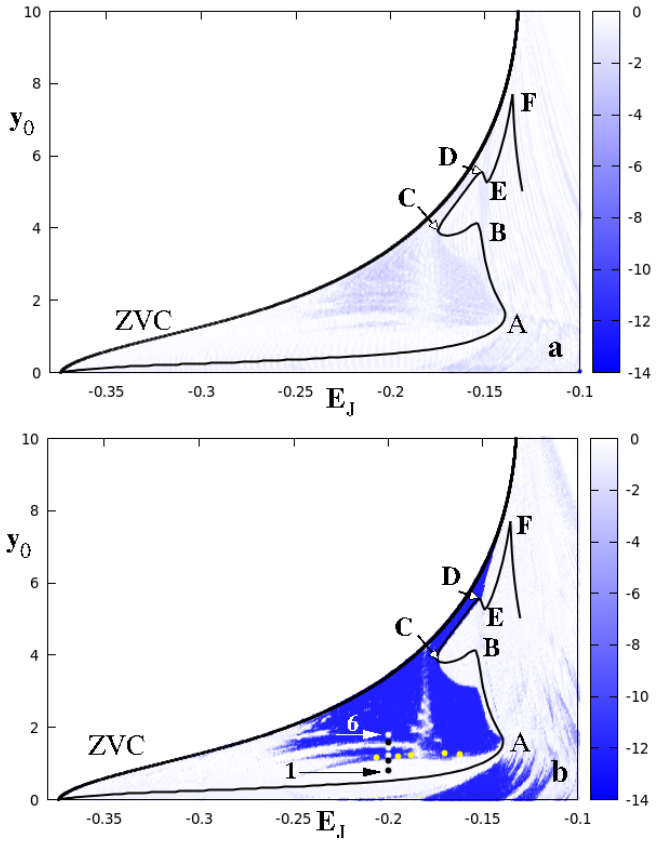

Figure 1.14: The chaoticity of the planar orbits on the equatorial plane of model based on the 2nd snapshot (see Fig. 1.1) is given color coded in (E_J, y_0) diagrams. The colour of each orbit (each point in the figures) corresponds to the value of the $\log_{10}(\mathrm{GALI}_2)$ quantity calculated for it and is taken from the color-bar on the right hand side of the figures. In (a) we calculate $\log_{10}(\mathrm{GALI}_2)$ for $t_1 = 1$ Gyr, while in (b) for $t_2 = 10$ Gyr. In both figures the zero velocity curve is indicated with "ZVC". The continuous black line in the region where motion is allowed is the characteristic of the main family. Capital letters (A,B,...,F) and arrows pointing to the points "C" and "D" are used for facilitating the description of the evolution of the curve (see [Chaves-Velasquez et al. 2017] for more details). We observe that in general the orbits with the smaller GALI_2 index in (a), which reach values $\log_{10}(\mathrm{GALI}_2) \lessapprox -5$, become strongly chaotic in (b). However, in (b) appear also additional features indicating chaotic behavior, that are absent in (a). Such features are the dark blue tails above the characteristic for $-0.27 \lessapprox E_J \lessapprox -0.17$. The six heavy dots at $E_J = -0.2$ indicate the initial conditions of the orbits we use to demonstrate the relation between GALI_2 and their morphology (see [Chaves-Velasquez et al. 2017] for more details). Arrows point to the 1st and 6th of them. The five heavy, yellow dots at $E_J = -0.206, -0.195, -0.18798, -0.17$ and -0.162 indicate the initial conditions of the boxy orbits we presented in [Chaves-Velasquez et al. 2017].

Regarding the TD analytical model, we established *stability trends* in terms of estimating the amount of regular and chaotic motion in different time-windows. In this case, we used a more realistic set of initial conditions coming directly from the simulation itself and iterated them under

the constructed TD potential. Even though, we did not manage to span the whole orbital richness of our ensemble of initial conditions, we have rather achieved to give a flavor of the possible evolutions for individual trajectories. It turns out that the complete set of orbits tends to become relatively more 'regular' in time.

By directly following the dynamical evolution of ensembles of orbits within the analytical potential, we were able to calculate the fractions of chaotic and regular motion resolved in both time and space. With this information we could evaluate not only the global trends in time, but also across several regions of the galactic disc and of the halo, associating them with distinct morphological features. We scrutinized the different changes of regime during the evolution, tracing the types of orbits back to their common origins.

The time-dependence of the analytical model ensures rather realistic dynamical transitions similar to an N-body simulation, i.e. bar formation and growth, development of a ring, a dynamical halo, etc. At the same time, this setup serves ideally to apply the GALI chaos detection method and in this way to determine the current chaotic (or otherwise) dynamical state of any given orbit at a fixed time interval, something that it is extremely hard to do in an N-body simulation. Moreover, the TD model has the advantage over a derived frozen potential from an N-body simulation, from the point of view that it incorporates smooth dynamical evolution via its time-dependent parameters and allows us to follow the both dynamical and morphological transitions.

A recipe for building two- and three-dimensional boxy structures in rotating bars was presented in [Chaves-Velasquez et al. 2017]. The basic idea is based on first starting with the planar backbone of periodic orbits for building a bar, namely with the well known x1 family. Then, instead of populating the model with regular quasi-periodic orbits encountered in the immediate neighborhood of the periodic orbit, one considers either periodic orbits close to the last Kolmogorov-Arnold-Moser torus (see e.g. [Contopoulos 2002]) or, more efficiently, the sticky chaotic orbits that surround the islands of stability, as they appear in the surfaces of section. In this way, such a selection of orbits secures a boxy morphology on the plane.

In a 3D model, when we eject out of the plane particles that follow the 2D boxy orbits by adding a $p_z \neq 0$ perturbation, we find that there is always a Δp_z range of perturbations for which all three projections of the 3D orbits are boxy. A remarkable property of these sticky boxy orbits is the formation of an X feature embedded in the bar in the *face-on* projections. For as long as we have the usual ellipses of the x1 family (or the x1-tree in 3D models according to [Ch. Skokos, Patsis, and Athanassoula 2002]) in a rotating bar, we can find a class of boxy 2D and 3D orbits. They are sticky chaotic orbits as their $GALI_2$ index indicates and they can support the bar, or a part of the bar, for many Gyr.

Observational features that can be reproduced by using such orbits as building blocks, can firstly be the boxy- or peanut-shaped bulges in the central parts of the bars. In these cases in the face-on views of the galaxies, we will observe boxy isophotes in their central parts, inside the bar, as in the sample of galaxies presented by [Erwin and Debattista 2013]. On the other hand, the work in [Chaves-Velasquez et al. 2017] indicates that in cases of slow rotating bars as in the TD models, the 3D boxy structure may constitute a major part of the bar. The presence of the X feature in the face-on views of the orbits, as well as the presence of a ring surrounding the bar, raises the question whether a dynamical mechanism as the one proposed by [Tsigaridi and Patsis 2015], acts in galaxies like IC 5240 presented in [R. J. Buta, Corwin, and Odewahn 2007].

Perspectives

Such an analytical TD model has the advantage of offering a fully time-dependent and astrophysically realistic galaxy model, as indicated by the fact that it was successful in recovering several dynamical and morphological features of a barred galaxy. Similar adequate TD models, exhibiting similar dynamical evolution like N-body simulations, are potentially suited to a broad class of applications in galactic dynamics (e.g. double bars, central mass concentrations and even bar dissolution). Once the output of an N-body simulation has been modeled into a time-dependent analytical potential, a variety of analyses could then be undertaken, particularly regarding orbital studies. Work that generally relied on highly simplified (and usually frozen) analytical potentials could take advantage of more astrophysically realistic galaxy models. This *bridging* would afford an approximation to the richness of detail of an N-body simulation, at a lower computational cost and with the versatility of a simple analytical formulation.

This work focused on one particular galaxy simulation, but the method may be extended to different galaxy types, taking as input the results of other N-body simulations. Here we focused on a strongly barred galaxy to maximise the effects we wished to explore. Clearly a natural extension would be to compare the present results with alternative galaxy models of varying bar strengths, disc masses, halo profiles, etc. Such a systematic exploration would reveal to which parameters the dynamical stability is most sensitive. For example, given the high fraction of chaotic motion found in the inner halo, the question arises as to what is the role of the dark matter profile in determining that behaviour. One might explore whether a more cuspy inner halo would help or rather hinder the rise of regular motion. A further development would be the inclusion of models containing gas [Patsis, Kaufmann, et al. 2009] and star formation. To this end, the hydrodynamical simulations of [Athanassoula, Machado, and Rodionov 2013b] would be ideally suited, since they already offer a systematic grid of models for galaxies with different halo triaxialities and different initial gas fractions, thus resulting in a variety of bar strength evolutions. More broadly, models derived from a fully cosmological hydrodynamical simulation of galaxy formation would offer an even more realistic scenario (e.g. [Valluri et al. 2013]) than the usual models of isolated galaxies. Finally, a specific issue that merits further analysis is the behaviour of the X-shaped (or boxy/peanut) bulge [Patsis and Katsanikas 2014b; Patsis and Katsanikas 2014d], particularly in light of the recent interest in the kinematics and structure of the Milky Way's own bulge [Saito et al. 2011; Zoccali et al. 2014].

In [Marostica D. A., Machado R. E. G., Manos T. and Athanassoula E., "From stellar to halo bars: quantifying the dark matter response", (submitted), 2020.], we aim to characterise the structure and kinematics of the halo bar, with the goal of correlating them with the properties of the stellar bar. Finally, and regarding families of orbits that can contribute to boxy morphologies, one can extend the work in [Chaves-Velasquez et al. 2017] (in frozen time snapshots) and study their robustness in fully TD analytical models [Manos T., Skokos Ch., Patsis P. A., "Orbits supporting bars in 3D, rotating, non-autonomous Hamiltonian systems" (in preparation), 2020].

Chapter 2

Complex phenomena in quantum systems

2.1 Background and introduction

Quantum chaos, or wave chaos, is the study of the phenomena in the quantum domain which correspond to the classical chaos in the Hamiltonian systems [Stöckmann 1999; Haake 2001]. Although quantum motion (time evolution of the wavefunctions) of bound systems with purely discrete energy spectrum is ultimately (after a sufficiently long time, asymptotically) stable and regular, in fact almost periodic, it exhibits many features of the classical motion such as e.g. diffusion in a chaotic domain, for times up to the Heisenberg time. The Heisenberg time, also called break time, is an important time scale in any quantum system, and is given by $t_H = 2\pi\hbar/\Delta E$, where $h = 2\pi\hbar$ is the Planck constant and ΔE is the mean energy level spacing, such that the mean energy level density is $\rho(E) = 1/\Delta E$. For times shorter than approximately t_H the quantum diffusion follows the classical chaotic diffusion, but is stopped at larger times, just due to interference phenomena, which occur due to the wave nature of the underlying system, and are typically destructive.

Pictorially speaking, for times up to t_H the quantum system behaves as if its evolution operator has a continuous spectrum, like the classical one has in the chaotic regime, but at later times it senses the discreteness of the spectrum. If the quantum diffusion stops, while the classical chaotic diffusion continues, we speak about the *dynamical localization*, or *quantum localization* or *Chirikov localization*, first observed in time-dependent systems [Casati, Chirikov, et al. 1979; Stöckmann 1999; Haake 2001]. Through the Fourier transform connection between the time and energy, the dynamical localization reflects itself also in the time-independent eigenfunctions, both in the eigenstates of the Floquet operator in time-periodic systems and in the eigenfunctions of the time-independent, classically chaotic, systems. Namely, if all classical transport times like the diffusion time (time necessary to occupy the entire classically available chaotic part of the phase space) are all shorter than the Heisenberg time t_H, we find extended eigenstates. In the contrary case, one observes localized eigenstates.

Another important aspect of quantum chaos is the statistics of the energy spectra of classically chaotic quantal systems. One of the main cornerstones in the development of quantum chaos [Stöckmann 1999; Haake 2001] is the finding that in classically fully chaotic, ergodic, autonomous Hamiltonian systems with purely discrete spectrum the fluctuations of the energy spectrum around its mean behavior obey the statistical laws described by the Gaussian Random Matrix Theory (RMT) [Mehta 1991; Guhr, Müller-Groeling, and Weidenmüller 1998], provided that we are in the sufficiently deep semiclassical limit. The latter condition means that all relevant classical transport times are smaller than Heisenberg time t_H. This statement is known as the Bohigas - Giannoni - Schmit (BGS) conjecture [Bohigas, Giannoni, and Schmit 1984; Casati, Valz-Gris, and Guarneri 1980]. Since $\Delta E \propto \hbar^f$, where f is the number of degrees of freedom (the dimension of the configuration space), we see that for sufficiently small $\hbar$-value the stated condition will always be satisfied. Alternatively, fixing the $\hbar$,

we can go to high energies such that the classical transport times become smaller than t_H. The role of the antiunitary symmetries that classify the statistics in terms of different ensembles of RMT, namely Gaussian Orthogonal Ensemble (GOE), Gaussian Unitary Ensemble (GUE) or Gaussian Symplectic Ensemble (GSE), has been elucidated in [Robnik and Berry 1986; Stöckmann 1999; Haake 2001; Mehta 1991]. The theoretical foundation for the BGS conjecture has been initiated first by Berry [Berry 1985], and later further developed by Richter and Sieber [Sieber and Richter 2001], arriving finally in the almost-final proof proposed by the group of F. Haake [Müller, Heusler, Braun, et al. 2004; Heusler et al. 2004; Müller, Heusler, Braun, et al. 2005; Müller, Heusler, Altland, et al. 2009].

On the other hand, if the system is classically integrable, then Poisson statistics applies (see e.g. [Stöckmann 1999; Haake 2001] and references therein, and for recent advances [Robnik and Veble 1998]). In the mixed type regime, where classical regular regions coexist in the classical phase space with chaotic regions, being a typical KAM-scenario which is the generic situation, the so-called Principle of Uniform Semiclassical Condensation (of the Wigner functions of the eigenstates; PUSC) applies, see e.g. [Berry 1977]. Consequently the Berry-Robnik statistics [Berry and Robnik 1984; Prosen and Robnik 1999a] is observed, again under the same semiclassical condition stated above, requiring that t_H is larger than all classical transport times. For more details about the mixed type regime, see [Berry and Robnik 1984; Prosen and Robnik 1993; Prosen and Robnik 1994a; Prosen and Robnik 1994b; Prosen and Robnik 1998; Prosen and Robnik 1999b; Grossmann and Robnik 2006] , while some more recent developments in the field were published in [Batistić and Robnik 2010; Batistić, Manos, and Robnik 2013; Batistić and Robnik 2013a; Batistić and Robnik 2013b].

If the couplings between the regular eigenstates and chaotic eigenstates become important, due to the dynamical tunneling, we can use the ensembles of random matrices that capture these effects [Vidmar et al. 2007]. As the tunneling strengths typically decrease exponentially with the inverse effective Planck constant, they rapidly disappear with increasing energy, or by decreasing the value of the Planck constant. In such cases the regular and chaotic eigenstates can be separated and the dynamical localization in the chaotic eigenstates can be studied (see [Prosen 2000] for a review and references therein). In such a situation it turns out that the Wigner functions of the chaotic eigenstates no longer uniformly occupy the entire classically accessible chaotic region in the classical phase space, but are localized on a proper subset of it. Indeed, this has been analyzed with unprecedented precision and statistical significance in [Batistić and Robnik 2010; Batistić and Robnik 2013a; Batistić and Robnik 2013b] for the case of mixed type systems. The important discovery is that the level spacing distribution of the dynamically localized chaotic eigenstates in periodic, as well as time-independent systems, is exceedingly well described by the Brody distribution (see e.g. [Brody et al. 1981] and references therein) with the Brody parameter values β_{BR} within the interval $[0, 1]$, where $\beta_{\mathrm{BR}} = 0$ yields the Poisson distribution in case of the strongest localization, and $\beta_{\mathrm{BR}} = 1$ gives the Wigner surmise (2D GOE, as an excellent approximation of the infinite dimensional GOE). The Brody distribution was found to fit the empirical data much better than the distribution function proposed in [Izrailev 1988; Izrailev 1990] and the references therein, characterized by the parameter β_{IZ}. It is well known that the Brody distribution so far has no theoretical foundation, but there are many empirical results showing that we have to consider it seriously thereby being motivated for seeking its physical foundation.

In this chapter, we review the work published mainly in [Manos and Robnik 2013; Batistić, Manos, and Robnik 2013; Manos and Robnik 2014; Manos and Robnik 2015], where the quantum kicked rotator (QKR) [Casati, Chirikov, et al. 1979] was explored from the classical point of view (the standard map, SM), its quantum analog was analyzed using the N-dimensional model of Izrailev, and the

semiclassical connection between the two pictures was considered. We shall treat the cases with the classical dimensionless kick parameter K in the range $K \in [5, 35]$, and for some purposes even up to $K = 70$, and in the end shall focus on the case $K = 10$, which is the most chaotic one in the sense that it is fully chaotic with minimal (in fact practically undetected) regular regions among all cases $K \in [5, 70]$ and among them best exhibits normal diffusion. Izrailev's N-dimensional model introduced and discussed in [Izrailev 1986; Izrailev 1987; Izrailev 1989; Izrailev 1990] is treated for various $N \leq 3000$ values, which in the limit $N \to \infty$ tends to the QKR. Due to the finiteness of N the observed (dimensionless) localization length of the eigenfunctions in the space of the angular momentum quantum number does not possess a sharply defined value, but has a certain distribution instead. Its reciprocal value is almost Gaussian distributed. This might be expected on the analogy with the finite time Lyapunov exponents in the Hamiltonian dynamical systems. In order to corroborate the theoretical findings on this topics we perform the numerical analysis of the finite time Lyapunov exponents in the SM (classical kicked rotator), especially the decay of the variance. Indeed, in the Shepelyansky picture [Shepelyansky 1986] the localization length can be obtained as the inverse of the smallest positive Lyapunov exponent of a finite $2k$-dimensional Hamiltonian system associated with the band matrix representation of the QKR, where k is the quantum kick parameter (to be precisely defined below) and where N plays the role of time.

However, unlike the chaotic classical maps or products of transfer matrices in the Anderson tight-binding approximation, where the mean value of the finite time Lyapunov exponents is usually equal to their asymptotic value at infinite time and the variance decreases inversely with time, as we also carefully checked, here the distribution is found to be independent of N: It has a nonzero variance even in the limit $N \to \infty$. This happens because the quantum kicked rotator at $N = \infty$ cannot be *exactly* modeled with finite bandwidth (equal to $2k$) band matrices, but only approximately. Hence, the underlying Hamiltonian system of the Shepelyansky picture has a growing dimension with N, implying asymptotically an infinite set of Lyapunov exponents and behavior different from the finite dimensional Hamiltonian systems. The observation of the distribution of the localization length around its mean value with finite variance also explains the strong fluctuations in the scaling laws of the kicked rotator, such as e.g. the entropy localization measure as a function of the theoretical scaling parameter Λ, to be discussed below. On the other hand, the two different empirical localization measures, namely the mean localization length as extracted directly from the exponentially localized eigenfunctions and the measure based on the information entropy of the eigenstates, are perfectly well linearly connected and thus equivalent. Therefore these results call for a refined theory of the localization length in the quantum kicked rotator and similar systems, where we must predict not only the mean value of the inverse localization length but also its (Gaussian) distribution, in particular the variance [Manos and Robnik 2015].

2.2 The classical and quantum kicked rotator models

The classical kicked rotator model: the standard map

The kicked rotator was introduced in [Casati, Chirikov, et al. 1979] and is one of the key model systems in classical and quantum chaos, especially for time-periodic (Floquet) systems. The Hamiltonian

function is:

$$H = \frac{p^2}{2I} + V_0\,\delta_T(t)\,\cos\theta. \tag{2.1}$$

Here p is the (angular) momentum, I the moment of inertia, V_0 is the strength of the periodic kicking, θ is the (canonically conjugate, rotation) angle, and $\delta_T(t)$ is the periodic Dirac delta function with period T. Between the kicks the rotation is free, therefore the Hamilton equations of motion can be immediately integrated, and thus the dynamics can be reduced to the SM, or so-called Chirikov-Taylor map, given by:

$$\begin{cases} p_{n+1} = p_n + V_0 \sin\theta_{n+1}, \\ \theta_{n+1} = \theta_n + \dfrac{T}{I} p_n, \end{cases} \tag{2.2}$$

where the quantities (θ_n, p_n) refer to their values just immediately after the n-th kick. Then, by introducing new dimensionless momentum $P_n = p_n T/I$, we get:

$$\begin{cases} P_{n+1} = P_n + K \sin\theta_{n+1}, \\ \theta_{n+1} = \theta_n + P_n, \end{cases} \tag{2.3}$$

where the system is now governed by a single classical *dimensionless* kick parameter $K = V_0 T/I$, and the mapping is area preserving.

The generalized diffusion process of the SM [Eq. (2.3)] is defined by:

$$\langle (\Delta P)^2 \rangle = D_\mu(K) n^\mu, \tag{2.4}$$

where n is the number of iterations (kicks), and the exponent μ is in the interval $[0, 2]$, and all variables P, θ and K are dimensionless. Here $D_\mu(K)$ is the generalized classical diffusion constant. In the case $\mu = 1$ we have the *normal diffusion*, and $D_1(K)$ is then the normal diffusion constant, whilst in the case of anomalous diffusion we observe *subdiffusion* when $0 < \mu < 1$ or *superdiffusion* if $1 < \mu \leq 2$. In the case $\mu = 2$ we have the *ballistic transport* which is associated strictly with the presence of accelerator modes.

In the case of the normal diffusion $\mu = 1$ the theoretical value of $D_1(K)$ is given in the literature, e.g. in [Izrailev 1990]:

$$D_1(K) = \begin{cases} \frac{1}{2}K^2\left[1 - 2J_2(K)\left(1 - J_2(K)\right)\right], \text{if } K \geq 4.5 \\ 0.15(K - K_{cr})^3, \text{if } K_{cr} < K \leq 4.5 \end{cases}, \tag{2.5}$$

where $K_{cr} \simeq 0.9716$ and $J_2(K)$ is the Bessel function. Here we neglect higher terms of order K^{-2}. However, there are many important subtle details in the classical diffusion further discussed below.

The dependence of the diffusion constant for the growth of the variance of the momentum on K is very sensitive, and described in the theoretical result [Eq. (2.5)], and fails around the period 1 accelerator mode intervals

$$(2\pi n) \leq K \leq \sqrt{(2\pi n)^2 + 16}, \tag{2.6}$$

n any positive integer. In these intervals for the accelerator modes $n = 1$ we have two *stable fixed points* located at $p = 0$, $\theta = \pi - \theta_0$ and $p = 0$, $\theta = \pi + \theta_0$, where $\theta_0 = \arcsin(2\pi/K)$. There are two

unstable fixed points at $p = 0,\ \theta = \theta_0$ and $p = 0,\ \theta = 2\pi - \theta_0$. For example, in the case $K = 6.5$ we have $\theta_0 \approx 1.31179$. Moreover, as the diffusion might even be anomalous, we have recalculated the *effective* diffusion constant $D_{\text{eff}} = \langle(\Delta P)^2\rangle/n$ numerically, which in general is not equal to the D_μ defined in Eq. (2.4). In Fig. 2.1 we show the D_{eff} for the SM as a function of K for three discrete times n, i.e., the number of the iterations of the SM, $n = 1000$ (lower red dashed line), $n = 5000$ (intermediate blue solid) and $n = 10000$ (upper black dot-dashed). In the background we have plotted the theoretical diffusion constant D_1 taking into account only the normal diffusion (gray dotted line) [Eq. (2.5)]. The presence of accelerator modes at certain intervals of K (and the sticky objects around) generates anomalous diffusion which is rendered by peaks. Here we used ≈ 100000 (314×314) initial conditions uniformly distributed in a grid on the entire phase space $[0, 2\pi] \times [0, 2\pi]$. We see that the dotted theoretical curve stemming from Eq. (2.5) describes the diffusion constant well outside the accelerator mode intervals. In general, however, the diffusion might be non-normal, described in Eq. (2.4). There are also accelerator modes of higher period (2,3,4...) observed and examined in this work.

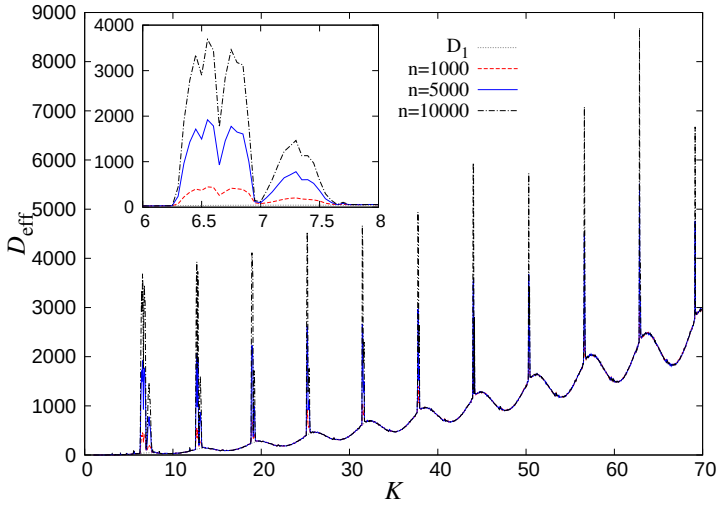

Figure 2.1: The classical diffusion constant $D_{\text{eff}} = \langle(\Delta P)^2\rangle/n$ for the SM as a function of K ($\delta K = 0.05$) for three discrete times n, i.e., the number of the iterations of the SM, $n = 1000$ (lower red dashed line), $n = 5000$ (intermediate blue solid) and $n = 10000$ (upper black dot-dashed). In the background we have plotted the classical diffusion constant D_1 (gray dotted line) [Eq. (2.5)]. The presence of accelerator modes at certain intervals of K (and the sticky objects around) generate anomalous diffusion which is rendered by peaks. Here we used $\approx$100000 (314×314) initial conditions uniformly distributed in a grid on the entire phase space $[0, 2\pi] \times [0, 2\pi]$.

In Fig. 2.2 we show the variance of the momentum P in the SM [Eq. (2.3)] with $K = 6.5$ (red crosses) where small islands and accelerator mode of period 1 are present and $K = 10.0$ (blue stars) where the phase space is fully chaotic for the same initial conditions as in Fig. 2.1 as a function of the discrete time n (number of iterations), in log-log representation. The two slopes associated with different types of diffusion are $\mu(K = 6.5) = 1.61252$ (dotted), $\mu(K = 10.0) = 0.991334$ (solid) with standard deviation errors ± 0.01271 (0.7881%) and ± 0.0009537 (0.0962%) respectively.

In this manner we have calculated the diffusion exponent μ for all K on the interval $K \in [K_{cr}, 70]$ and the result is shown in Fig. 2.3. We show the diffusion exponent μ as a function of K after $n = 5000$

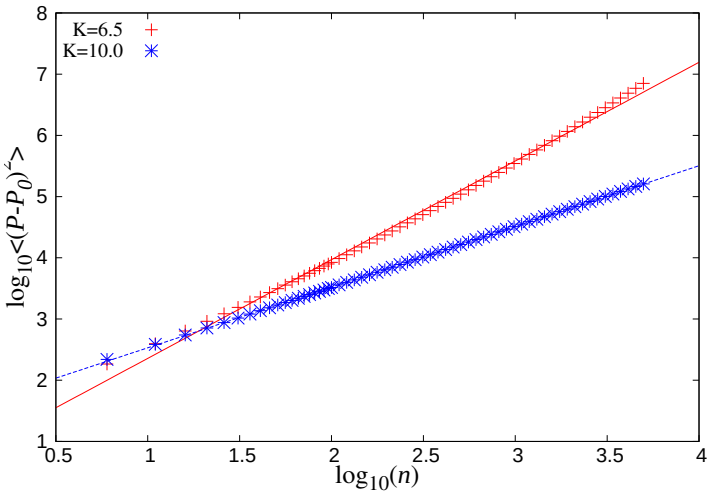

Figure 2.2: The variance of the momentum P in the SM [Eq. (2.3)] with $K = 6.5$ (red crosses) where small islands and accelerator mode of period 1 are present and $K = 10.0$ (blue stars) where the phase space is fully chaotic for the same initial conditions as in Fig. 2.1 as a function of the discrete time n (number of iterations), in log-log representation. The two slopes associated with different types of diffusion are $\mu(K = 6.5) = 1.61252$ (dotted), $\mu(K = 10.0) = 0.991334$ (solid) with standard deviation errors ± 0.01271 (0.7881%) and ± 0.0009537 (0.0962%) respectively.

iterations, using a fine grid of 314×314 (≈ 100000) initial conditions on the plane $(\theta, P) = (0, 2\pi)$. The μ is calculated by the slopes, of the lines of the variance of the momentum P as a function of iterations, as it is described in [Eq. (2.4)] and for a grid of cells on the entire phase space. The intervals on the black horizontal line $\mu = 0.9$ indicate the intervals of stable accelerator modes of period 1 [Eq. (2.6)]. All intervals of K with exponent $\mu \approx 1$ are associated with normal diffusion processes. The large peaks (appearing mainly for $K > 2\pi$ marked with full black circles) reflect the anomalous diffusion due to accelerator modes [of period 1, being located inside the intervals predicted by the Eq. (2.6)]. However, there is a number of relatively smaller peaks for $K < 2\pi$ (more clearly presented in the inset panel of Fig. 2.3), whose origin is accelerator modes of higher period as we will see later, and also for $2\pi < K < 4\pi$, both these sets are marked with empty circle. With the symbol ($\times$) we mark few typical examples, close to those peaks, for which the diffusion is normal and are studied in detail in [Manos and Robnik 2014].

All the large peaks for $K > 2\pi$, marked with full black circles in Fig. 2.3, correspond to regimes with accelerator modes of period 1 and they decrease monotonically as a power law:

$$f(x) = ax^b, \tag{2.7}$$

where $a = 2.41645$ and $b = -0.195896$ [blue dotted line in Fig. 2.3, with asymptotic standard error ± 0.04294 (1.777%) and ± 0.00537 (2.741%) respectively] indicating that for $K > 70$ their effect decreases significantly. On the other hand, the size of the successive accelerator modes of period 1 intervals decays with a power law defined simply and analytically by the Eq. (2.6).

In order to understand the effect of the presence of accelerator modes in the diffusion and transport properties of the phase space in the SM, we first picked an, as much as possible, representative sample of K-values. In more detail, we included in our test-cases all the K-values which correspond to all

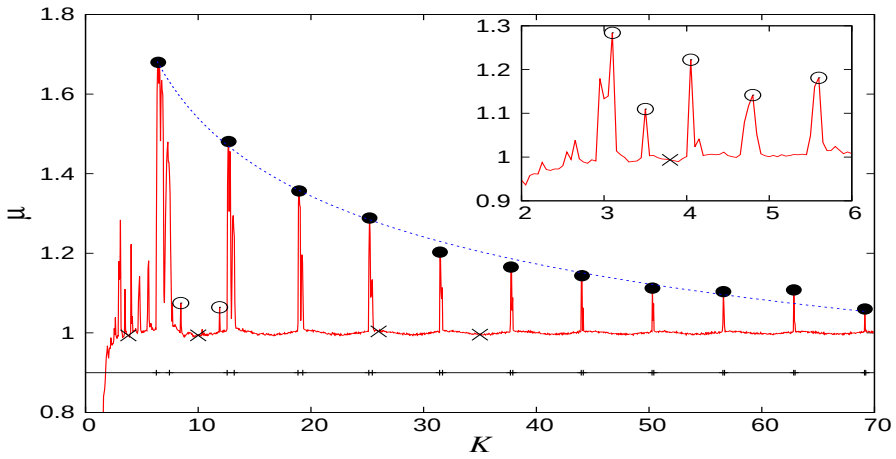

Figure 2.3: The diffusion exponent μ as a function of K after $n = 5000$ iterations and for ≈100000 (314×314) initial conditions on the plane $(\theta, P) = (0, 2\pi)$. The intervals on the black horizontal line $\mu = 0.9$ indicate the intervals of stable accelerator modes of period 1 [Eq. (2.6)]. All intervals of K with exponent $\mu \approx 1$ are associated with normal diffusion processes. The large peaks (appearing mainly for $K > 2\pi$ marked with full black circles) reflect the anomalous diffusion accelerator modes (mainly of period 1). The smaller peaks for $K < 2\pi$ (more clearly presented in the inset panel) originate by accelerator modes of higher period together with those for $2\pi < K < 4\pi$ marked with empty circle and a few typical examples close to those peaks [marked with the symbol (×)], for which the diffusion is normal, are studied thoroughly in [Manos and Robnik 2014]. The blue dotted line corresponds to the power law which describes the decay of the exponent μ of the main peaks' amplitude due to accelerator modes of period 1.

the main peaks appearing in Fig. 2.3 with $K > 2\pi$ together with a few cases from the 'plateaus' of this curve. Furthermore, we took into account the peaks occurring for $1 \lesssim K \lesssim 2\pi$ (see the empty black circles in the inset zoom in Fig. 2.3) which are associated with accelerator modes of higher periodicity, as it will be seen thereupon. The case with $K = 3.8$, whose μ value is ≈ 1, is chosen for comparison reasons from the plateau and as it turns out has no accelerator modes in its phase space causing anomalous diffusion. Here we should stress that we repeated the same procedure for larger number of iterations $n = 10000$ and it turns out that the exponent μ has well converged to the values shown in Fig. 2.3.

The distribution of the momenta in the case of normal diffusion is found to be perfect Gaussian, whilst for anomalous diffusion a strong departure from the Gaussian distribution is observed, being well fitted by a stable Lévy distribution, characterized by the parameter $\alpha \in [0, 2]$. The details are given in reference [Manos and Robnik 2014]. For each one of the K-values of the nonlinearity kick parameter of Fig. 2.3, we have performed a thorough study by calculating and comparing the following quantities:

(a) The index of stability α-parameter of the Lévy stable distribution.

(b) The diffusion exponent μ as described in Eq. (2.4).

In the case of normal diffusion (Gaussian statistics) for the above quantities, one expects to find $\alpha = 2$ for the Lévy stable distribution and diffusion exponent $\mu = 1$, while in the general case we find other values. We have calculated the μ exponent emerging from a small box/ensemble

of initial conditions in the phase space and thus produced the μ-landscape in the phase space of the SM. Furthermore, we have also employed the GALI-method [Ch. Skokos, T. Bountis, and Ch. Antonopoulos 2007; C. Skokos and Manos 2016] to calculate the GALI-index in order to identify the regular and chaotic regions in the phase space of the SM, which also quantifies the degree of chaos (indirectly). The GALI-landscape and the μ-landscape are found to correspond very well to each other, where it seems that the μ-plot contains more information than GALI-plot [Manos and Robnik 2014]. Hence, the SM exhibits normal diffusion for most of the K values on the interval $[K_{cr}, 70]$, except for the accelerator mode intervals where anomalous diffusion is observed, with the exponent μ typically being larger than 1. Using these plots and the described methodology we found that the case $K = 10$ is the closest to full chaos (no regular islands present) and exhibits the normal diffusion for all initial conditions in the phase space of the SM.

The quantum kicked rotator model

The quantum kicked rotator (QKR) is the quantized version of Eq. (2.1), namely:

$$\hat{H} = -\frac{\hbar^2}{2I}\frac{\partial^2}{\partial\theta^2} + V_0\,\delta_T(t)\,\cos\theta. \tag{2.8}$$

The Floquet operator $\hat{F}$ acting on the wavefunctions (probability amplitudes) $\psi(\theta)$, $\theta \in [0, 2\pi)$, upon each period (of length T) can be written as (see [Stöckmann 1999]):

$$\hat{F} = \exp\left(-\frac{iV_0}{\hbar}\cos\theta\right)\exp\left(-\frac{i\hbar T}{2I}\frac{\partial^2}{\partial\theta^2}\right), \tag{2.9}$$

where now we have two *dimensionless* quantum control parameters:

$$k = \frac{V_0}{\hbar}, \quad \tau = \frac{\hbar T}{I}, \tag{2.10}$$

which satisfy the relationship $K = k\tau = V_0 T/I$, K being the classical *dimensionless* control parameter of Eq. (2.3). By using the angular momentum eigenfunctions:

$$|n\rangle = a_n(\theta) = \frac{1}{\sqrt{2\pi}}\exp(i\,n\,\theta), \tag{2.11}$$

where n is any integer, we find the matrix elements of $\hat{F}$, namely:

$$F_{m\,n} = \langle m|\hat{F}|n\rangle = \exp\left(-\frac{i\tau}{2}n^2\right) i^{n-m} J_{n-m}(k), \tag{2.12}$$

where $J_\nu(k)$ is the ν-th order Bessel function. For a wavefunction $\psi(\theta)$ we shall denote its angular momentum component (Fourier component) by:

$$u_n = \langle n|\psi\rangle = \int_0^{2\pi} a_n^*(\theta)\psi(\theta)\,d\theta = \frac{1}{\sqrt{2\pi}}\int_0^{2\pi}\psi(\theta)\exp(-in\theta)\,d\theta. \tag{2.13}$$

The QKR has very complex dynamics and spectral properties. As the phase space is infinite (cylinder), $p \in (-\infty, +\infty), \theta \in [0, 2\pi)$, the spectrum of the eigenphases of $\hat{F}$, denoted by ϕ_n, or the associated

quasienergies $\hbar\omega_n = \hbar\phi_n/T$, can be continuous, or discrete. It is quite well understood that for the resonant values of τ:

$$\tau = \frac{4\pi r}{q}, \tag{2.14}$$

q and r being positive integers without common factor, the spectrum is continuous, as rigorously proven by Izrailev and Shepelyansky [Izrailev and Shepelyansky 1980], and the dynamics is (asymptotically) ballistic, meaning that starting from an arbitrary initial state the mean value of the momentum $\langle\hat{p}\rangle$ increases *linearly* in time, and the energy of the system $E = \langle\hat{p}^2\rangle/(2I)$ grows *quadratically* without limits. For the special case $q = r = 1$ this can be shown elementary. Such behavior is a purely quantum effect, called the quantum resonance. Also, the regime of quadratic energy growth manifests itself only after very large time, which grows very fast with the value of the integer q from Eq. (2.14), such that for larger q this regime practically cannot be observed.

For generic values of $\tau/(4\pi)$, being irrational number, the spectrum is expected to be discrete but infinite. But the picture is very complicated. Casati and Guarneri [Casati and Guarneri 1984] have proven that for $\tau/(4\pi)$ sufficiently close to a rational number, there exists a continuous component in the quasienergy spectrum. So, the absence of dynamical localization for such cases is expected as well. Without a rigorous proof, we finally believe that for all other ("good") irrational values of $\tau/(4\pi)$ we indeed have discrete spectrum and quantum dynamical localization. In such case the quantum dynamics is almost periodic, and because of the effective finiteness of the relevant set of components u_n and of the basis functions involved, just due to the exponential localization (see below), it is even effectively quasiperiodic (effectively there is a finite number of frequencies), and any initial state returns after some recurrence time arbitrarily close to the initial state. Thus the energy cannot grow indefinitely.

2.3 Localization and Diffusion Properties

The asymptotic localized eigenstates are *exponentially localized*. The (dimensionless) theoretical localization length in the space of the angular momentum quantum numbers is given below, and is equal (after introducing some numerical correction factor α_μ) to the dimensionless localization time t_{loc} [Eq. (2.16)]. We here denote it by $\mathcal{L}$ unlike in reference [Izrailev 1990] and [Manos and Robnik 2013]. Therefore, an exponentially localized eigenfunction centered at m in the angular momentum space [Eq. (2.11)] has the following form:

$$|u_n|^2 \approx \frac{1}{\mathcal{L}} \exp\left(-\frac{2|m-n|}{\mathcal{L}}\right), \tag{2.15}$$

where u_n is the probability amplitude [Eq. (2.13)] of the localized wavefunction $\psi(\theta)$. The argument leading to t_{loc} in Eq. (2.16) originates from the observation of the dynamical localization (see e.g. [Casati, Chirikov, et al. 1979]), and is well explained in [Stöckmann 1999], in case of normal diffusion $\mu = 1$, whilst for general μ we gave a theoretical argument in [Manos and Robnik 2013]. We shall denote $\sigma = 2/\mathcal{L}$, and will later on determine the σ's directly from the individual numerically calculated eigenstate.

But where one is able to observe such phenomena (spectral statistics, namely Brody-like level spacing distribution) analogous in the quantum chaos of time-independent bound systems with discrete spectrum? To see these effects the system must have effectively finite dimension, because in

the infinite dimensional case we simply observe Poissonian statistics. Truncation of the infinite matrix F_{mn} in Eq. (2.12) in *tour de force* is not acceptable, even in the technical case of numerical computations, since after truncation the Floquet operator is no longer unitary.

The only way to obtain a quantum system which shall in this sense correspond to the classical dynamical system [Eqs. (2.1), (2.2) and (2.3)] is to introduce a finite N-dimensional matrix, which is symmetric unitary, and which in the limit $N \to \infty$ becomes the infinite dimensional system with the Floquet operator [Eq. (2.9)]. The semiclassical limit is $k \to \infty$ and $\tau \to 0$, such that $K = k\tau =$ constant. As it is well known [Izrailev 1990], for the reasons discussed above, the system behaves very similarly for rational and irrational values of $\tau/(4\pi)$. Such a N-dimensional model [Izrailev 1988] will be introduced below.

Following [Manos and Robnik 2013] and references therein, we find that the dimensionless Heisenberg time (also called break time or localization time and denoted by $t_{\rm loc}$ in units of kicking period T) is equal to the dimensionless localization length $\mathcal{L}$ (see Eq. (2.20 below). Here we repeat briefly the main steps to derive this result:

$$\mathcal{L} \approx t_{\rm loc} = \left(\alpha_\mu \frac{D_\mu(K)}{\tau^2} \right)^{\frac{1}{2-\mu}} . \tag{2.16}$$

where α_μ is a numerical constant to be determined empirically, and in case of normal diffusion $\mu = 1$ is close to $1/2$. Since this semiclassical approach and derivation is quite important, we repeat the arguments given in [Manos and Robnik 2013].

The generalized diffusion process of the SM [Eq. (2.3)] is defined by Eq. (2.4). As the real physical angular momentum p and P are connected by $P = pT/I$ we have for the variance of p the following equation:

$$\langle (\Delta p)^2 \rangle = \frac{I^2}{T^2} D_\mu n^\mu . \tag{2.17}$$

Now we argue as follows: The general rule in quantum chaos is that the quantum diffusion follows the classical diffusion up to the Heisenberg time (or break time, or localization time), defined as:

$$t_H = \frac{2\pi\hbar}{\Delta E}, \tag{2.18}$$

where ΔE is the mean energy level spacing. In our case we have the quasienergies and $\Delta E = \hbar\Delta\omega$, where $\Delta\omega = \Delta\phi/T$, and $\Delta\phi$ is the mean spacing of the eigenphases. This might be estimated at the first sight as $\Delta\phi = 2\pi/N$, but this is an underestimate, as effectively we shall have due to the localization only $\mathcal{L}$ levels on the interval $[0, 2\pi)$. Therefore $\Delta\phi = 2\pi/\mathcal{L}$ and we find:

$$t_H = \frac{2\pi T}{\Delta\phi} = T\mathcal{L}. \tag{2.19}$$

Since T is the period of kicking, and t_H is the real physical continuous time, we get the result that the discrete time [number of iterations of Eq. (2.3) at which the quantum diffusion stops], the localization time $t_{\rm loc}$ is indeed equal to the localization length in momentum space, i.e.:

$$t_{\rm loc} \approx \mathcal{L}. \tag{2.20}$$

Since our derivation is not rigorous, we use the approximation symbol rather than equality, in particular as the definition depends linearly on the definition of the Heisenberg time. Now the final

step: By inspection of the dynamics of the Floquet quantal system [Eqs. (2.8),(2.9)] one can see (the derivation can be found in [Stöckmann 1999]) that the value of the variance of the angular momentum at the point of stopping the diffusion $\langle(\Delta p)^2\rangle$ is proportional to $\hbar^2\mathcal{L}^2$, and to achieve equality we introduce a dimensionless numerical (empirical,correction) factor α_μ by writing $\langle(\Delta p)^2\rangle = \hbar^2\mathcal{L}^2/\alpha_\mu$, which on the other hand must be equal just to the classical value at stopping time $t_{\rm loc}$, namely equal to $(I/T)^2 D_\mu \mathcal{L}^\mu$. From this it follows immediately Eq. (2.16). The numerical constant α_μ is found empirically by numerical calculations, for instance in the literature the case $K = 5$ with $\mu = 1$ is found to be $\alpha_1 = 0.5$ (however, we find numerically $\alpha_1 = 0.45$, taking into account Eq. (2.16) when studying the model's localization properties). Thus, we have the theoretical formula for the localization length in the case of generalized classical diffusion [Eqs. (2.4),(2.17)], which we use in defining the scaling parameter Λ below.

2.4 The Floquet (Izrailev) model

The motion of the QKR [Eq. (2.8)] after one period T of the ψ wavefunction can be described also by the following symmetrized Floquet mapping, describing the evolution of the kicked rotator from the middle of a free rotation over a kick to the middle of the next free rotation, as follows:

$$\psi(\theta, t+T) = \hat{U}\psi(\theta, t), \tag{2.21}$$
$$\hat{U} = \exp\left(i\frac{T\hbar}{4I}\frac{\partial^2}{\partial\theta^2}\right)\exp\left(-i\frac{V_0}{\hbar}\cos\theta\right)\exp\left(i\frac{T\hbar}{4I}\frac{\partial^2}{\partial\theta^2}\right).$$

Thus, the $\psi(\theta, t)$ function is determined in the middle of the rotation, between two successive kicks. The evolution operator $\hat{U}$ of the system corresponds to one period. Due to the instant action of the kick, this evolution can be written as the product of three non-commuting unitary operators, the first and third of which correspond to the free rotation during half a period $\hat{G}(\tau/2) = \exp\left(i\frac{\tau}{4}\frac{\partial^2}{\partial\theta^2}\right)$, $\tau \equiv \hbar T/I$, while the second $\hat{B}(k) = \exp(-ik\cos\theta)$, $k \equiv V_0/\hbar$, describes the kick. Like before, we have only two dimensionless parameters, namely τ and k, and $K = k\tau = V_0 T/I$. In the case $K \equiv k\tau \gg 1$ the motion is well known to be strongly chaotic, for $K = 10$ certainly without any regular islands of stability, as mentioned, and also there are no accelerator modes, so that the diffusion is normal ($\mu = 1$). We have carefully checked that the case $K = 10$ is the closest to the normal diffusion $\mu = 1$ for all $K \in [K_{cr}, 70]$. The transition to classical mechanics is described by the limit $k \to \infty$, $\tau \to 0$ while $K = \text{const}$. We shall consider the regimes on the interval $3 \le k \le 20$, but will concentrate mostly on the semiclassical regime $k \ge K$, where $\tau \le 1$.

In order to study how the localization affects the statistical properties of the quasienergy spectra, we use the model's representation in the momentum space with a finite number N of levels [Izrailev 1988; Izrailev 1990; Izrailev 1986; Izrailev 1987; Izrailev 1989], which we refer to as Izrailev model:

$$u_n(t+T) = \sum_{m=1}^{N} U_{nm} u_m(t), \;\; n, m = 1, 2, ..., N \;\; . \tag{2.22}$$

The finite symmetric unitary matrix U_{nm} determines the evolution of an N-dimensional vector, namely the Fourier transform $u_n(t)$ of $\psi(\theta, t)$, and is composed in the following way:

$$U_{nm} = G_{nn'} B_{n'm'} G_{m'm} \tag{2.23}$$

where $G_{ll'} = \exp\left(i\tau l^2/4\right)\delta_{ll'}$ is a diagonal matrix corresponding to free rotation during a half period $T/2$, and the matrix $B_{n'm'}$ describing the one kick has the following form:

$$B_{n'm'} = \frac{1}{2N+1}\times \sum_{l=1}^{2N+1}\left\{\cos\left[\left(n'-m'\right)\frac{2\pi l}{2N+1}\right] - \cos\left[\left(n'+m'\right)\frac{2\pi l}{2N+1}\right]\right\}\times\exp\left[-ik\cos\left(\frac{2\pi l}{2N+1}\right)\right]. \tag{2.24}$$

The Izrailev model [Eqs. (2.22-2.24)] with a finite number of states is considered as the quantum analogue of the classical SM on the torus with closed momentum p and phase θ, where U_{nm} describes only the odd states of the systems, i.e. $\psi(\theta) = -\psi(-\theta)$, provided we have the case of the quantum resonance, namely $\tau = 4\pi r/(2N+1)$, where r is a positive integer, as in Eq. (2.14). The matrix (2.24) is obtained by starting the derivation from the odd-parity basis of $\sin(n\theta)$ rather than the general angular momentum basis $\exp(in\theta)$.

Nevertheless, we shall use this model for any value of τ and k, as a model which in the resonant and in the generic case (irrational $\tau/(4\pi)$) corresponds to the classical kicked rotator, and in the limit $N \to \infty$ approaches the infinite dimensional model [Eq. (2.21)], restricted to the symmetry class of the odd eigenfunctions. It is of course just one of the possible discrete approximations to the continuous infinite dimensional model.

The difference of behavior between the generic case and the quantum resonance shows up only at very large times, which grow fast with $(2N+1)$, as explained above. It turns out that also the eigenfunctions and the spectra of the eigenphases at finite dimension N of the matrices that we consider do not show any significant differences in structural behavior for the rational or irrational $\tau/(4\pi)$, which we have carefully checked. Indeed, although the eigenfunctions and the spectrum of the eigenphases exhibit *sensitive dependence on the parameters* τ and k, their statistical properties are stable against the small changes of τ and k. This is an advantage, as instead of using very large single matrices for the statistical analysis, we can take a large ensemble of smaller matrices for values of τ and k around some central value of $\tau = \tau_0$ and $k = k_0$, which greatly facilitates the numerical calculations and improves the statistical significance of our empirical results. Therefore our approach is physically meaningful. Similar approach was undertaken by Izrailev (see [Izrailev 1990] and references therein). In Figs. 2.4 and 2.5 (from [Manos and Robnik 2013]), we show the examples of strongly exponentially localized eigenstates by plotting the natural logarithm of the probabilities $w_n = |u_n|^2$ versus the momentum quantum number n, for two different matrix dimensions N. By calculating the localization length $\mathcal{L}$ from the slopes $\sigma = 2/\mathcal{L}$ of these eigenfunctions using Eq. (2.15) we can get the first quantitative empirical localization measure to be discussed and used later on. The new finding in [Manos and Robnik 2015] is that σ has a distribution, which is close to the Gaussian (but cannot be exactly that, because σ is a positive definite quantity). It does not depend on N and survives the limit $N \to \infty$. Therefore also $\mathcal{L}$ has a distribution whose variance does not vanish in the limit $N \to \infty$.

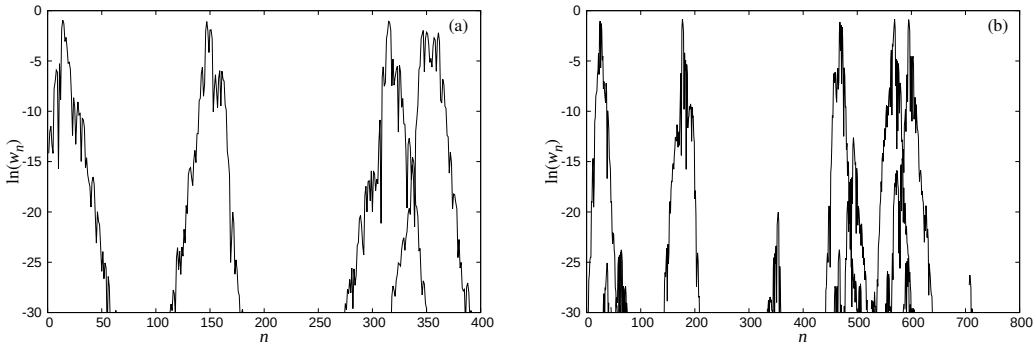

Figure 2.4: (a) A sample of strong localized eigenstates for $K = 7$, $r = 222$, $k \approx 2.00$ and $N = 398$ (b) Same for $K = 7$, $r = 444$, $k \approx 2.00$ and $N = 796$.

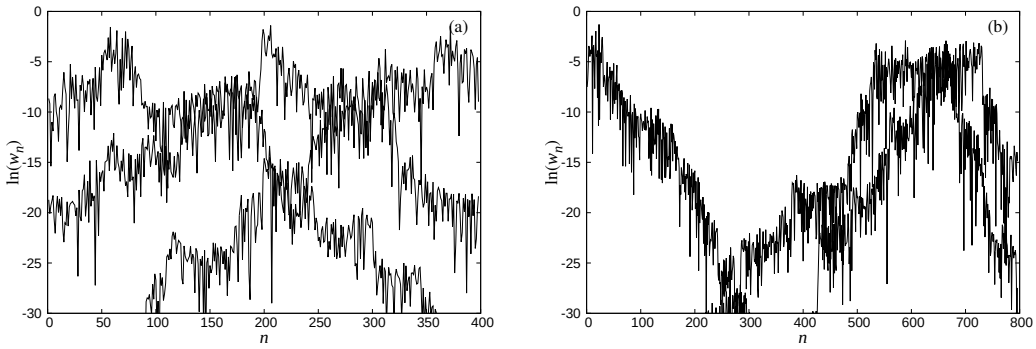

Figure 2.5: (a) A sample of weak localized eigenstates for $K = 7$, $r = 63$, $k \approx 7.05$ and $N = 398$ (b) Same for $K = 7$, $r = 127$, $k \approx 6.99$ and $N = 796$.

2.5 Dynamical (Chirikov) Localization

Following [Manos and Robnik 2013] and [Izrailev 1990] we introduce another measure of localization. For each N-dimensional eigenvector of the matrix U_{nm} the information entropy is:

$$\mathscr{H}_N(u_1, ..., u_N) = -\sum_{n=1}^{N} w_n \ln w_n, \tag{2.25}$$

where $w_n = |u_n|^2$, and $\sum_n |u_n|^2 = 1$.

In case of the random matrix theory being applicable to our system [Eqs. (2.21) and (2.22-2.24)], namely the Circular orthogonal ensemble (COE) (or GOE), due to the isotropic distribution of the eigenvectors of a COE of random matrices, we have the probability density function of $|u_n|$ on the interval $[0, 1]$:

$$w_N(|u_n|) = \frac{2\Gamma(N/2)}{\sqrt{\pi}\Gamma((N-1)/2)}(1 - |u_n|^2)^{(N-3)/2}. \tag{2.26}$$

It is easy to show that in the limit $N \to \infty$ this becomes a Gaussian distribution:

$$w_N(|u_n|) = \sqrt{\frac{2N}{\pi}} \exp\left(-\frac{N|u_n|^2}{2}\right), \tag{2.27}$$

and the corresponding information entropy [Eq. (2.25)] is equal to:

$$\mathscr{H}_N^{GOE} = \psi\left(\frac{1}{2}N+1\right) - \psi\left(\frac{3}{2}\right) \simeq \ln\left(\frac{1}{2}Na\right) + O(1/N), \tag{2.28}$$

where $a = \frac{4}{\exp(2-\gamma)} \approx 0.96$, while ψ is the digamma function and γ the Euler constant ($\simeq 0.57721...$). For a uniform distribution over M states $w_n = 1/M$ we get $\mathscr{H}_N \approx \log M$, and thus $M \approx \exp(\mathscr{H}_N)$. Thus, we get the insight that the correct measure of localization must be proportional to $\exp(\mathscr{H}_N)$, but properly normalized, such that in case of extendedness (GOE/COE) it is equal to N.

Therefore the *entropy localization length* l_H is defined as:

$$l_H = N \exp\left(\mathscr{H}_N - \mathscr{H}_N^{GOE}\right). \tag{2.29}$$

Indeed, for entirely extended eigenstates $l_H = N$. Thus, l_H can be calculated for every eigenstate individually. However, all eigenstates, while being quite different in detail, are exponentially localized, and thus statistically very similar. Therefore, in order to minimize the fluctuations one uses the *mean localization length* $d \equiv \langle l_H \rangle$, which is computed by averaging the entropy over all eigenvectors of the same matrix (or even over an ensemble of similar matrices):

$$d \equiv \langle l_H \rangle = N \exp\left(\langle \mathscr{H}_N \rangle - \mathscr{H}_N^{GOE}\right). \tag{2.30}$$

The *localization parameter* $\beta_{\rm loc}$ is then defined as:

$$\beta_{\rm loc} = \frac{d}{N} \equiv \frac{\langle l_H \rangle}{N}. \tag{2.31}$$

The parameter that determines the transition from weak to strong quantum chaos is neither the strength parameter k nor the localization length $\mathcal{L}$, but the ratio of the localization length $\mathcal{L}$ to the size N of the system in momentum p:

$$\Lambda = \frac{\mathcal{L}}{N} = \frac{1}{N}\left(\frac{\alpha_\mu D_\mu(K)}{\tau^2}\right)^{\frac{1}{2-\mu}}, \tag{2.32}$$

where $\mathcal{L} \approx t_{\rm loc}$, the theoretical localization length Eq. (2.16), was derived in [Manos and Robnik 2013]. Λ is the scaling parameter of the system. The relationship of Λ to $\beta_{\rm loc}$ is discussed e.g. in [Casati, Guarneri, et al. 1990; Izrailev 1990] and further developed in [Manos and Robnik 2013] (Sect. VII). Here we just summarize by showing the empirical scaling property of Λ versus $\beta_{\rm loc}$ in Fig. 2.6, where the approximate analytical description is given by the function:

$$\beta_{\rm loc} = \frac{\gamma\Lambda}{1+\gamma\Lambda}, \quad \gamma = 4.04, \tag{2.33}$$

which is similar to the scaling law in in [Casati, Guarneri, et al. 1990], but not the same. Namely, the value $\gamma = 4.04$ differs somewhat from $\gamma \approx 3.2$ in [Casati, Guarneri, et al. 1990], where $\beta_{\rm loc}$ is plotted versus $x \approx 4\Lambda$.

In producing this plot we have used Eqs. (2.16),(2.32) for Λ, which is just a rough estimate. Indeed, as we shall show below, following [Manos and Robnik 2015], Λ is not a number in a given system, at fixed K, k and N, but has a distribution, whose reciprocal is approximately Gaussian distributed, and Eq. (2.16) is just a rough estimate of the mean value of Λ. Therefore we should not be surprised any more to see large fluctuations in the scaling law of Fig. 2.6, an observation entirely unexplained so far, but clarified in [Manos and Robnik 2015]. The statistical properties of the localization measure will be discussed below.

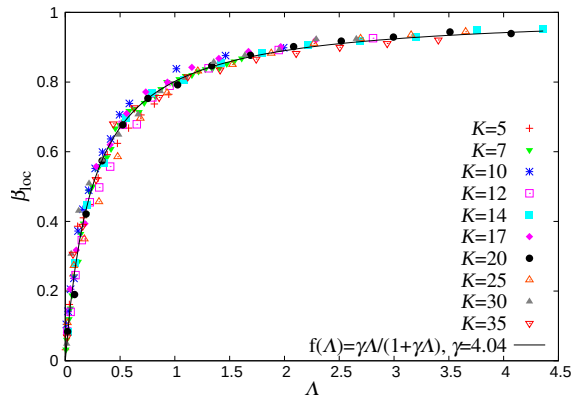

Figure 2.6: The parameter $\beta_{\rm loc}$ vs. Λ for 161×398 elements for various values of K and for a wide range of k values, where the scaling law [Eq. (2.33)] is shown with the black line.

2.6 Level spacing distribution: $P(S)$, $W(S)$ and $U(S)$

To study the eigenvalue statistics of quantum Floquet systems and quantum maps one considers the eigenphases $\phi_n \in [0, 2\pi)$ defined by $\lambda_n = e^{i\phi_n}$. In such case the spectral unfolding procedure is very easy, as the mean level density is $N/(2\pi)$, i.e. the mean level spacing is $2\pi/N$. The histogram of the level spacing distribution $P(S)$ is the distribution of the spacings $S_n := \frac{N}{2\pi}(\phi_{n+1} - \phi_n)$ with $n = 1, ..., N$ and $\phi_{N+1} := \phi_1$, in the bins of certain suitable size ΔS. The factor $N/2\pi$ ensures that the average of all spacings S_n is 1, and thus $P(S)$ is supported on the interval $[0, N]$, and its upper limit goes to ∞ when $N \to \infty$.

The cumulative distribution $W(S)$, or integrated level spacing distribution, preserving the full accuracy of all numerical eigenvalues/spacings, useful especially when the number of levels N is small, is defined as:

$$W(S) = \int_0^S P(x)dx \equiv \frac{\#\{n|S_n \leq S\}}{N}. \tag{2.34}$$

Finally, we shall use also the so-called U-function (see Appendix A in [Manos and Robnik 2015]):

$$U(S) = \frac{2}{\pi} \arccos \sqrt{1 - W(S)}. \tag{2.35}$$

The U-function has the advantage that its expected statistical error δU is independent of S, being constant for each S and equal to $\delta U = 1/(\pi\sqrt{N_s})$, where N_s is the total number of objects in the $W(S)$ distribution. The numerical pre-factor $2/\pi$ in Eq. (2.35) is determined in such a way that $U(S) \in [0, 1]$ when $W(S) \in [0, 1]$. The U-function is an excellent and refined criterion used to assess the goodness of the fit of the theoretical level spacing distribution.

The important special level spacing distributions that we are using are the following:

- The Poisson distribution:

$$P_{\rm Poisson}(S) = e^{-S}, \quad W_{\rm Poisson}(S) = 1 - e^{-S}. \tag{2.36}$$

- The COE or GOE distribution:

$$P_{\rm COE}(S) \approx P_{\rm Wigner}(S) = \frac{\pi}{2} \exp\left(-\frac{\pi}{4}S^2\right), \quad W_{\rm COE}(S) = 1 - \exp\left(\frac{-\pi S^2}{4}\right). \tag{2.37}$$

- The Brody distribution, [Brody et al. 1981]:

$$P_{\rm BR}(S) = C_1 S^{\beta} \exp\left(-C_2 S^{\beta+1}\right), \tag{2.38}$$

where the two parameters C_1 and C_2 are determined by the two generic normalization conditions that must be obeyed by any $P(S)$:

$$\int_0^{\infty} P(S)dS = 1, \quad \langle S\rangle = \int_0^{\infty} SP(S)dS = 1, \tag{2.39}$$

thus with $\langle S\rangle = 1$ being the mean distance between neighboring levels (after unfolding). Hence:

$$C_1 = (\beta+1)C_2, \quad C_2 = \left[\Gamma\left(\frac{\beta+2}{\beta+1}\right)\right]^{\beta+1}, \tag{2.40}$$

where $\Gamma(x)$ denotes the Gamma function. In the strongly localized regime $\beta = 0$ we observe Poissonian statistics while in the fully chaotic one $\beta = 1$ and the RMT applies. The Brody cumulative level spacing distribution is:

$$W_{\rm BR}(S) = 1 - \exp(-C_2 S^{\beta+1}). \tag{2.41}$$

- Izrailev distribution: In [Izrailev 1988; Izrailev 1989], Izrailev suggested the following distribution in order to describe the intermediate statistics, i.e. the non-integer β in the following PDF could be associated with the statistics of the quasienergy states with chaotic localized eigenfunctions, also approximating the level spacing distribution arising from the Dyson COE joint probability distribution [Porter 1965]:

$$P_{\rm IZ}(S) = A\left(\frac{1}{2}\pi S\right)^{\beta} \exp\left[-\frac{1}{16}\beta\pi^2 S^2 - \left(B - \frac{1}{4}\pi\beta\right)S\right], \tag{2.42}$$

where again the two parameters A and B are determined by the two normalization conditions $\langle 1\rangle = \langle S\rangle = 1$ given above.

Of course, we must be fully aware of the fact that both, Brody and Izrailev distributions, are approximations. It is clear that at $\beta_{\rm BR} = 1$ we get precisely Wigner surmise [Eq. (2.37)], which is the exact GOE only for two-dimensional Gaussian random matrices, and thus only an (excellent) approximation for the infinite dimensional GOE case. Indeed, if we try to fit the exact infinite dimensional GOE level spacing distribution with the Brody distribution, we do not get $\beta_{\rm BR} = 1$, but instead $\beta_{\rm BR} = 0.953$, see [Brody et al. 1981]. Also, we should mention that Izrailev *et al.* have published an improved distribution function [Casati, Izrailev, and Molinari 1991], which we have also tested, and is defined by:

$$P_{\rm IZ}^{\rm new}(S) = AS^{\beta}(1 + B\beta S)^{f(\beta)} \exp[-\frac{\pi^2}{16}\beta S^2 - \frac{\pi}{2}(1 - \frac{\beta}{2}S)] \tag{2.43}$$

where $f(\beta) = \frac{2^{\beta}(1-\frac{\beta}{2})}{\beta} - 0.16874$ and A, B are the normalization parameters. We found (see below) that in our applications it is even worse than the original version [Eq. (2.42)].

2.7 Lévy stable distribution

The physical origin and relevance of the Lévy stable distribution to this kind of problems, like the SM, is well summarized in e.g. [Zaslavsky 2007; Zaslavsky, Edelman, and Niyazov 1997; Klafter and Zumofen 1994; Geisel, Nierwetberg, and Zacherl 1985; Zaslavsky and Edelman 2000]. In probability theory, an α-Lévy skew stable distribution is a four parameter family of continuous probability distributions, characterizing the location, scale, skewness and kurtosis. Following [Nolan 2013], for a random variable X with distribution function $F(x)$, the characteristic function is defined by $\phi(u) = E\exp(\mathrm{i}uX) = \int_{-\infty}^{\infty}\exp(\mathrm{i}ux)dF(x)$. Then, a random variable X is *stable* if and only if $X \stackrel{\delta}{=} aZ + b$, with $a > 0$, $b \in \mathbb{R}$ and Z is a random variable with characteristic function:

$$E\exp(\mathrm{i}uZ) = \begin{cases} e^{-|u|^{\alpha}[1-\mathrm{i}\beta\tan\frac{\pi\alpha}{2}(\mathrm{sign}u)]}, & \alpha \neq 1 \\ e^{-|u|[1+\mathrm{i}\beta\tan\frac{2}{\pi}(\mathrm{sign}u)]\log|u|}, & \alpha = 1 \end{cases}, \tag{2.44}$$

where $0 < \alpha \leq 2$ and $-1 \leq \beta \leq 1$ (the symbol $\stackrel{\delta}{=}$ indicates that both expressions have the same probability law). We then adopt the parametrization $k = 0$, $S(\alpha, \beta, \gamma, \delta; 0)$ for which the random variable X given by:

$$X \stackrel{\delta}{=} \begin{cases} \gamma(Z - \beta\tan(\frac{\pi\alpha}{2})) + \delta, & \alpha \neq 1 \\ \gamma Z + \delta, & \alpha = 1 \end{cases}, \tag{2.45}$$

has characteristic function:

$$S(\alpha, \beta, \gamma, \delta; 0) \equiv E\exp(\mathrm{i}uX) = \begin{cases} e^{\mathrm{i}u\delta - \gamma^{\alpha}|u|^{\alpha}(1+\mathrm{i}\beta(-1+|u\gamma|^{1-\alpha})\mathrm{sign}(u)\tan(\frac{\pi\alpha}{2}))}, & \alpha \neq 1 \\ e^{\mathrm{i}u\delta - \frac{\gamma|u|(\pi+2\mathrm{i}\beta\log(|u\gamma|))\mathrm{sign}(u)}{\pi}}, & \alpha = 1 \end{cases}, \tag{2.46}$$

where $Z = Z(\alpha, \beta)$ is defined as described in Eq. (2.44), $\alpha \in (0, 2]$ is the index of stability or characteristic exponent, $\beta \in [-1, 1]$ the skewness parameter, $\gamma > 0$ the scale parameter and $\delta \in \mathbb{R}$ location parameter. For the fits with data we used the *Stable Distribution* package of *Mathematica* [Rimmer and Nolan 2005]. Two important special cases are the Gaussian distribution with $\alpha = 2$ and the Cauchy-Lorentz with $\alpha = 1$ which are the only ones with an explicit closed formula.

2.8 Results

In Fig. 2.7, we present the probability distribution function of the momentum P after $n = 5000$ iterations (black filled circles) and the fits with the α-Lévy stable distribution (solid blue line) for a sample of K-values associated with the principal peaks (presence of accelerator modes of period 1) of the Fig. 2.3, i.e., $K = 6.50, 11.90, 13.20, 18.95$. In Fig. 2.7(a),(d),(e),(f) α is generally not equal to 2 and two K-values without accelerator modes, i.e., $K = 7.0, 10.0$, are shown in Fig. 2.7(b),(c) where α is equal to 2. Here, and for comparison reasons with the best-fit function depicted in the figures, the Gaussian distribution (red dashed line) is derived by the $S(\alpha, \beta, \gamma, \delta; 0)$ probability distribution by setting $\alpha = 2$ and keeping all the remaining parameters the same as given by the fits generally for $\alpha \neq 2$. The total number of initial conditions is $\approx$100000 (314×314) on a uniform grid in the entire phase plane $(\theta, P) \in [0, 2\pi] \times [0, 2\pi]$. For larger K-values with accelerator modes of period 1, their effect in the diffusion process is becoming gradually weaker, as can also be seen by the decay of the μ

value in Fig. 2.3, and the probability distributions tend to Gaussian-like ones. We have also calculated the χ^2-test for all the density distributions of Fig. 2.7. However, the derived quantitative information turns out, not to differ much to what the panels show. Let us also stress that the goodness of the several fits is not the main point here but rather the deviation from the Gaussian profile which is evident when the effect of the accelerator mode is relatively strong as shown in panel (a) and expressed by α parameter value far from 2. Moreover, due to our main motivation, i.e., to focus on the relevant quantum time scales, we do not expect to capture very accurately the tails, which are expected to follow the theoretical curve at much larger times. More examples and the details regarding the whole set of parameters can be found in [Manos and Robnik 2014]. Note that, for $K < 2\pi$ the fit was done for an ensemble in a cell around the origin $(\theta, P) = (0, 0)$ instead of a grid uniform in the entire phase space, in order to exclude the data coming from islands of stability whose momenta do not diffuse at all and mix up the distribution.

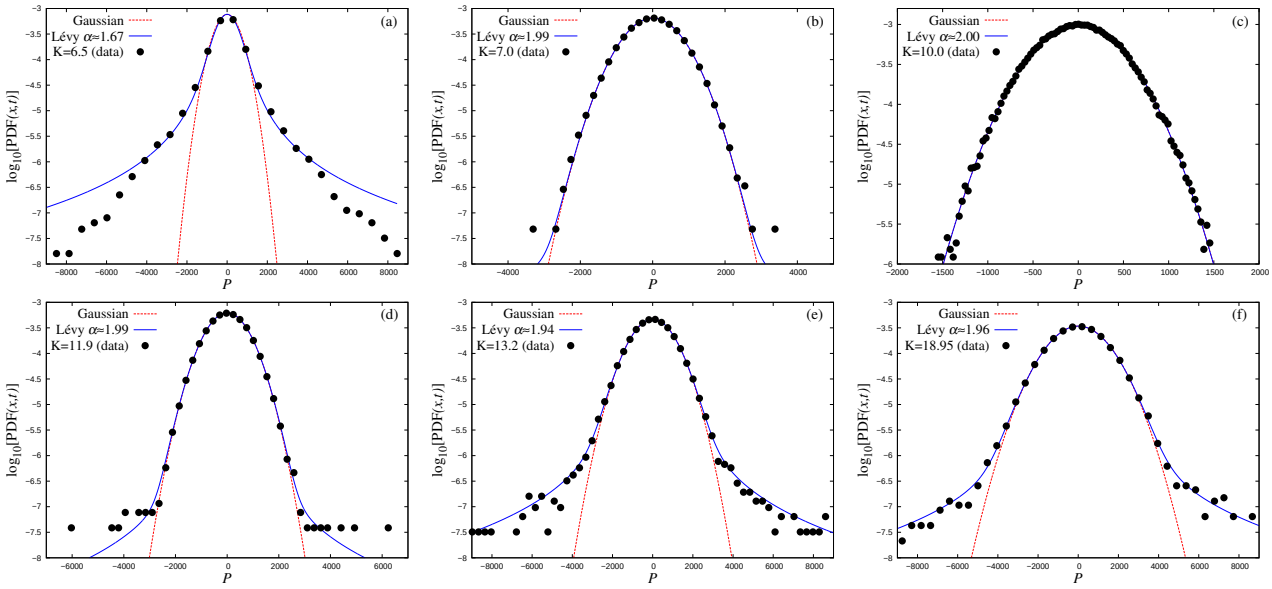

Figure 2.7: The probability distribution function of the momentum P after $n = 5000$ iterations (black filled circles) and the fits with the stable α-Lévy distribution for a sample of K-values associated with the principal peaks (presence of accelerator modes of period 1) of the Fig. 2.3, i.e., $K = 6.5, 11.9, 13.2, 18.95$ (a),(d),(e),(f) where α is generally not equal to 2 and two K-values without accelerator modes, i.e., $K = 7.0, 10.0$ (b),(c) where α is equal to 2. Here, the Gaussian distribution (red dashed line) for comparison reasons with the best-fit function, depicted in the figures, is derived by the $S(\alpha, \beta, \gamma, \delta; 0)$ probability distribution by setting $\alpha = 2$ and keeping all the rest parameters same as the given by the fits in general $\alpha \neq 2$. The total number of initial conditions is ≈100000 (314×314) on a uniform grid in the entire phase plane $(\theta, P) \in [0, 2\pi] \times [0, 2\pi]$. For larger K-values with accelerator modes of period 1, their effect in the diffusion process is becoming gradually weaker, as can be seen also by the decay of the μ value in Fig. 2.3, and the probability distributions tend to Gaussian-like ones.

In Fig. 2.8(a) we present the outcome of the calculation of the $GALI_2$ on the whole phase plane $(\theta, P) \in [0, 2\pi] \times [0, 2\pi]$ for $K = 3.1$, for 500×500 initial conditions uniformly distributed. Each initial condition is colored according to the color scale seen at the right side of the panel. For chaotic orbits,

having small GALI_2 value ($\approx 10^{-8}$) are colored black, while the yellow color corresponds to regular motion, found here to be $\approx 13.52\%$ of the whole plane, with high - close to zero - values (the color bar is in a logarithmic scale). Thus, we can clearly identify even tiny regions of regular motion which are not easily seen in the phase space portraits given often by simple Poincaré surface of sections. Having located the stable region of the phase space, the next point of interest is to distinguish among them, those that are due to accelerator modes from those due to islands of stability.

The distinction can be efficiently achieved with the use of the diffusion exponent μ color-plot in Fig. 2.8(b), where we first consider again a grid of 500×500 cells (on the entire phase space $(\theta, P) \in [0, 2\pi] \times [0, 2\pi]$) with 50×50 initial conditions in each and evolve all of them together for $n = 5000$ iterations. Then, for each ensemble of each cell separately, we calculate numerically the diffusion coefficient $D_\mu(K)$ as a function of the iterations n and perform a fit procedure just like in Fig. 2.2 to calculate the diffusion exponent μ [represented in the color bar of Fig. 2.8(b)] that *characterizes* the different kind of diffusion of this small area. Depending on the relative location of each ensemble one may expect to find: (i) *normal diffusion* ($\mu = 1$) inside chaotic regimes without the presence of accelerator modes, (ii) *subdiffusion* ($0 < \mu < 1$) inside islands of stability, (iii) *superdiffusion* ($1 < \mu < 2$) inside chaotic regimes with the presence of accelerator modes in the phase space and (iv) *ballistic transport* ($\mu \approx 2$) inside and in the very close vicinity of accelerator modes.

It turns out that the stable regions around $(\pi/2, 0)$, $(3\pi/2, 0)$, $(\pi/2, \pi)$, $(3\pi/2, \pi)$ and $(\pi/2, 2\pi)$, $(3\pi/2, 2\pi)$ are indeed islands of stability since their diffusion exponent μ is smaller than 1. The remaining tiny stable areas correspond to stable higher period accelerator modes with $\mu \approx 2$. Here we manage to locate the accelerator modes of higher periods 2,3,4,... which in general are not so easy to be calculated analytically. In Fig. 2.8(c) we show two examples (marked with an empty square and empty circle in panel b) following different diffusion processes, i.e., for a trajectory oscillating between islands of stability (empty dotted boxes) and for one transported ballistically (with $P < 0$) by the effect of an accelerator mode (full circles). The period of both is 4 (when projected on the $(\theta, P) \in [0, 2\pi]$), as it can be seen by iterating them for a few steps.

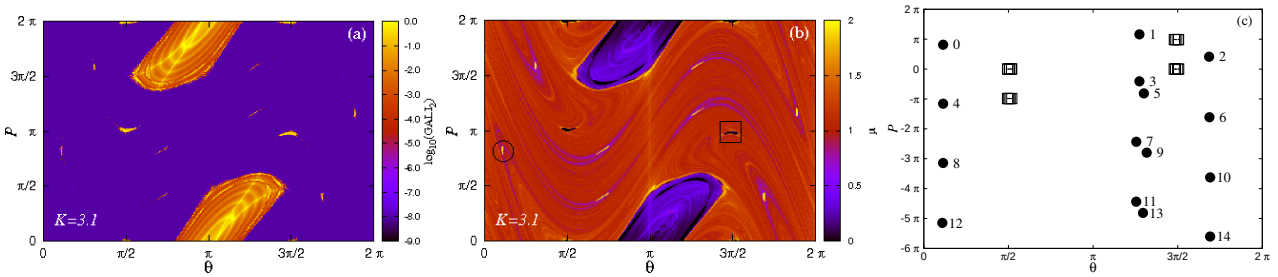

Figure 2.8: (a) The GALI_2 for $K = 3.1$ with 50×50 initial conditions on a grid 500×500 on the entire phase space $(\theta, P) \in [0, 2\pi] \times [0, 2\pi]$. (b) the diffusion exponent μ for the same kick parameter value for 50×50 initial conditions on a 500×500 cell grid of the entire phase space calculated after $n = 5000$ iterations (see text for more details). (c) Two examples (marked with an empty square and empty circle in panel b) following different diffusion processes: a trajectory transported ballistically (with $P < 0$) by the effect of an accelerator mode of period 4 (•) and one oscillating between islands of stability (⊡) of period 4 too.

Analysis of the level spacing distribution of numerical spectra

For the numerical calculations and results regarding the spacing distributions $P(S)$ (and $W(S)$) for the eigenphases ϕ_j, we have considered a range of 41-values of the quantum parameter k ($= 2, 3, ..., 42$) keeping fixed the classical parameter $K = 7$, where the phase space is fully chaotic (see [Manos and Robnik 2013]). In order to ameliorate the statistics we considered a sample of 161 matrices U_{nm} of size $N = 398$ ($\approx 64,000$ elements), in a similar manner as in [Izrailev 1988]) with slightly different values of k (with the step size $\Delta k = \pm 0.00125 \ll k$). For some samples we reached up to 641 matrices U_{nm} of size $N = 398$ acquiring qualitatively the same results.

For the ensemble of $M = 641$ matrices of size $N = 398$, in case $K = 7$ and $k = 11$, using the χ^2 best fitting procedure (described in more detail below) we found $\beta_{\rm BR} = 0.421$ and all three representations clearly show excellent agreement with the best fitting Brody distribution. In Fig. 2.9a

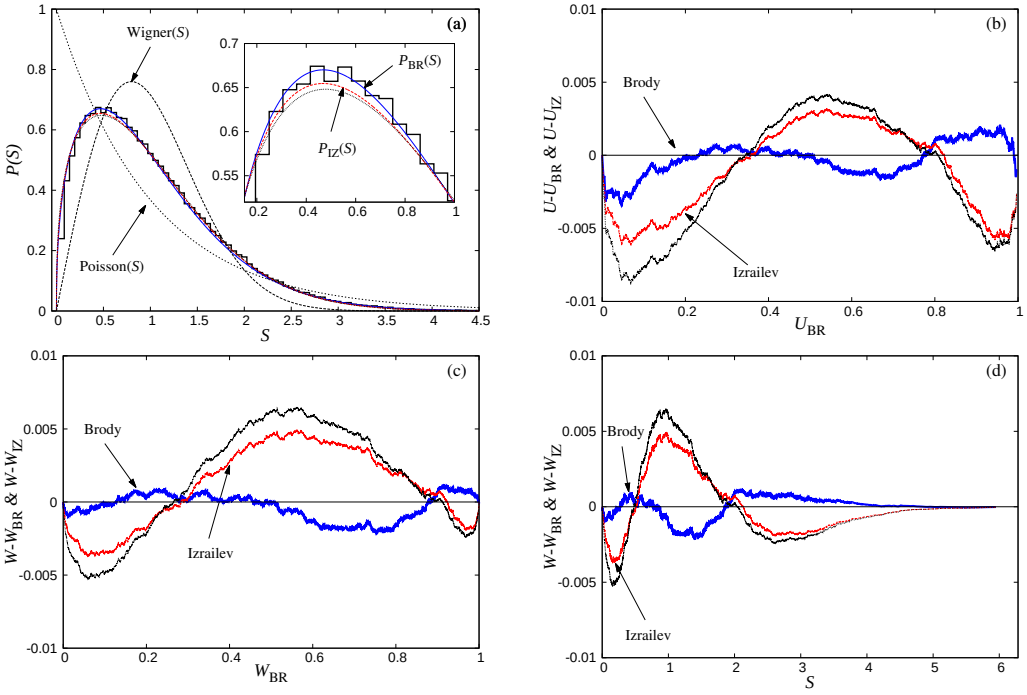

Figure 2.9: Intermediate statistics (panel (a)) for distribution $P(S)$ (histogram - black line) of the model fitted with distribution $P_{\rm BR}$ (blue-solid line), $P_{\rm IZ}$ (red-dashed line pointed by the arrow in the inset figure) and $P_{\rm IZ}^{\rm new}$ (black-dotted line) for $M \times N = 641 \times 398$, $K = 7$ and $k = 11$ (see text for discussion). In panels (b),(c),(d) we show the difference of the numerical data and the best fitting Brody (blue-thick line), "old" Izrailev (red-medium line) and Izrailev "new/improved" (black-thin line; always the outer one) PDFs by using the U-function and W-distribution. Thus, in case of the ideal fitting the data would lie on the abscissa. In this case, based on the $P(S)$ fit we get $\beta_{\rm BR}$=0.421, $\beta_{\rm IZ}$(old)=0.416 and $\beta_{\rm IZ}$(new)=0.376, and based on the $W(S)$ fit we get $\beta_{\rm BR}$=0.421, $\beta_{\rm IZ}$(old)=0.401, $\beta_{\rm IZ}$(new)=0.350.

we show the histogram. It is seen that Brody distribution is better fitting the data than the Izrailev distribution. Since the deviations are really small, the statistical significance very high, we plot in Fig. 2.9b the differences U(data) $-$ U(Brody/Izrailev) versus $U_{\rm BR}$. Thus if data are on the abscissa

the agreement is perfect. As can be seen, the deviations from that are really small, and clearly smaller for Brody. In Fig. 2.9c we show the fine differences of $W(\text{data}) - W(\text{Brody/Izrailev})$ versus W_{BR}, and again we clearly see that Brody is better. Finally, in Fig. 2.9d we show the same thing as in Fig. 2.9c, except not versus W but versus S instead.

Residues and χ^2 test:

In the best fitting procedure we have calculated both the residues and the χ^2 as follows:

- PDFs residues: $R_{\text{PDFs}} = \sum_{i=1}^{N}(P_{\text{BR,IZ}}(i) - \text{data}(i))^2$.
- χ^2: $\chi^2_{\text{PDFs}} = \sum_{i=1}^{N} \frac{(P_{\text{BR,IZ}}(i) - \text{data}(i))^2}{P_{\text{BR,IZ}}(i)}$.

In Fig. 2.10 we show three examples for the χ^2 as a function of the fitted parameter β_{BR} or β_{IZ}. It is clearly demonstrated that Brody fit is significantly better than Izrailev. In Fig. 2.11 we show the

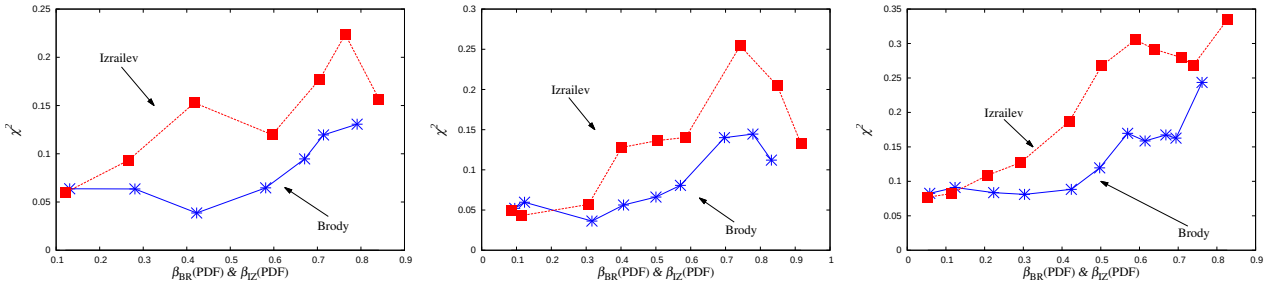

Figure 2.10: χ^2 for P_{BR} and P_{IZ} for $N = 398$ (a), $N = 796$ (b) and $N = 4000$ (c) for various values of the best fits for β_{BR} (black line) and β_{IZ} (gray line) using 150 subintervals in S.

scaling of the Brody spectral parameter β_{BR} vs. the localization parameter β_{loc}. They are linearly related almost like identity, but we also observe rather large fluctuations, probably due to the fact that β_{BR} is difficult to calculate accurately enough with small matrices.

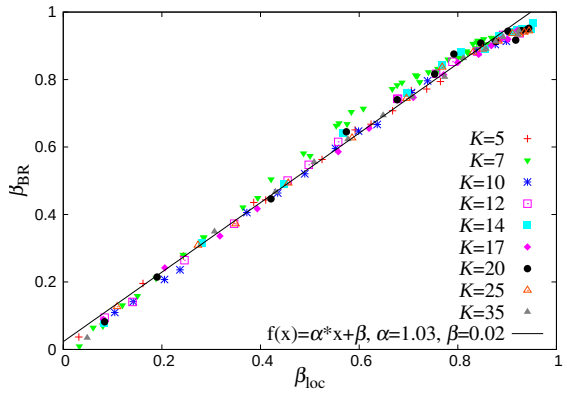

Figure 2.11: The fit parameter β_{BR} as a function of β_{loc} for 161×398 elements for various values of K and for a wide range of k values. The best fitting straight line is very close to identity.

The distribution of the localization measures

Following [Manos and Robnik 2015], we here present the results about the distribution of the localization measures. We restricted our analysis exclusively to the case $K = 10$, as this case is the closest to the normal diffusion regime $\mu = 1$. First we demonstrate that the localization measures $\mathcal{L} = 2/\sigma$ and l_H are very well defined, linearly related and thus equivalent. In Fig. 2.12 we showed this in the diagram of the mean $\langle\sigma\rangle$ versus $2/\langle l_H\rangle$, where both averagings are over all eigenfunctions for matrices of dimension $N = 3000$, for 7 nearby values of k around k_0, namely $k = k_0 \pm j\delta k$, where $j = 0, 1, 2, 3$ and $\delta k = 0.00125$, for $k_0 = 3, 4, 5, \ldots, 19$.

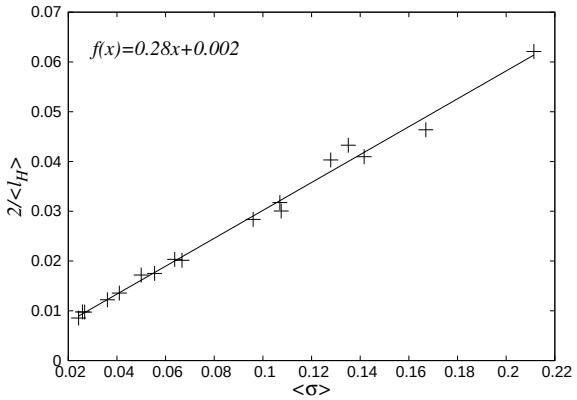

Figure 2.12: $\langle\sigma\rangle$ versus $2/\langle l_H\rangle$ for matrices of dimension $N = 3000$, for 7 nearby values of k, namely $k = k_0 \pm j\delta k$, where $j = 0, 1, 2, 3$ and $\delta k = 0.00125$, for $k_0 = 3, 4, 5, \ldots, 19$. The two empirical localization measures are clearly well defined, linearly related and thus equivalent.

In the Fig. 2.13, we show the relationship of the theoretical $\mathcal{L}$ in Eq. (2.16) and the mean value of the empirical $2/\langle\sigma\rangle$ for $k_0 = 3, 4, 5, ..., 19$. It is clearly seen in Fig. 2.13(a) that there are strong fluctuations which we attribute to the fact that $2/\sigma$ has a certain distribution with nonvanishing variance, to be presented and described below, and that the theory of $\mathcal{L}$ resulting in Eq. (2.16) is too simple, as it corresponds only roughly to the value of $2/\langle\sigma\rangle$. On the other hand, in Fig. 2.13(b) we see again that the two empirical localization measures are exactly linearly related. We should mention that in the cases of larger $k > 19$ the slopes σ are so small, and the localization too weak, that we cannot get reliable results. Therefore we limit ourselves to the interval $3 \leq k \leq 19$.

We have thereby demonstrated that the empirical localization measures are well defined, while the theoretical prediction for their mean values is not good enough. The reason is that the localization measures of a given fixed system (with fixed $K = 10$ and k) have a distribution with nonvanishing variance, which is out of the scope of current semiclassical theories, as they do not predict this distribution and the corresponding variance. This finding, as the central result of the paper [Manos and Robnik 2015], is demonstrated in Fig. 2.14. The distributions are clearly seen to be close to a Gaussian, but cannot be exactly that, as σ is always a positive definite quantity. Its inverse, the localization length equal to $\mathcal{L} = 2/\sigma$, has a distribution whose empirical histograms are much further away from a Gaussian, so that in this sense σ is the fundamental quantity. Indeed, it corresponds to the finite time Lyapunov exponent known in the theory of dynamical systems.

As l_H and $2/\sigma$ are equivalent localization measures, the former one is expected also to have a distribution, which we demonstrate in the histograms of Fig. 2.15. We have also analyzed how the

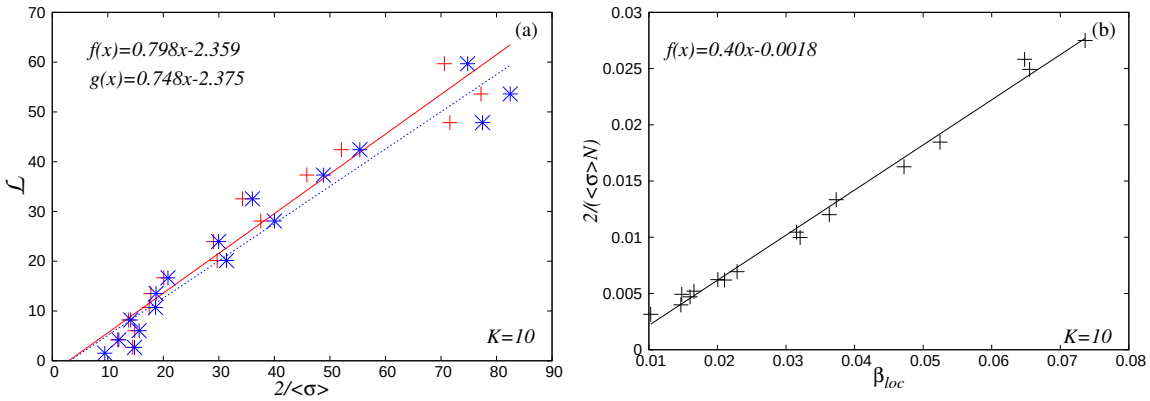

Figure 2.13: (a) $\mathcal{L}$ versus $2/\langle\sigma\rangle$ for matrices of dimension $N = 1000$ (crosses and solid fit line) and for matrices of dimension $N = 3000$ (stars and dashed fit line), for 7 nearby values of k, namely $k = k_0 \pm j\delta k$, where $j = 0, 1, 2, 3$ and $\delta k = 0.00125$, for $k_0 = 3, 4, 5, ..., 19$. (b) We plot the mean value of $2/(N\langle\sigma\rangle)$ versus $\beta_{\rm loc}$ for $k_0 = 3, 4, 5, \ldots, 19$ and 7 matrices of dimension $N = 3000$ with $k = k_0 \pm j\delta k$, where $j = 0, 1, 2, 3$ and the step size $\delta k = 0.00125$.

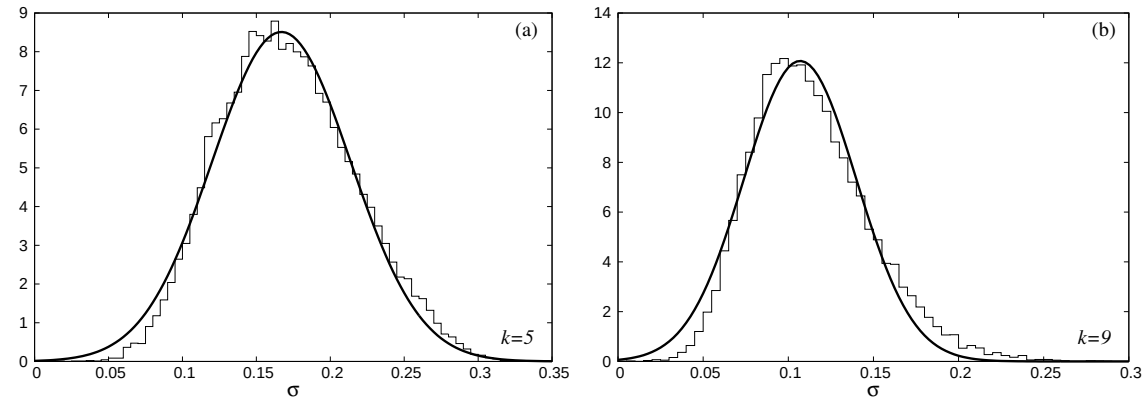

Figure 2.14: The histograms of the slopes σ for four systems, matrices of dimension $N = 3000$, for each of them with seven different values of k close to $k_0 = 5, 9, 13, 17$, namely $k = k_0 \pm j\delta k$, where $j = 0, 1, 2, 3$ and $\delta k = 0.00125$: (a) $k_0 = 5$, (b) $k_0 = 9$.

localization measures vary in the semiclassical limit of the increasing value of the quantum parameter k, at fixed classical parameter $K = 10$. Indeed, the theoretical estimate of $\mathcal{L}$ in Eq. (2.16), at fixed K, and remembering $k = K/\tau$, shows that approximately the mean value of the localization length should increase quadratically with k, or equivalently, the slope σ should decrease inversely quadratically with k. This prediction is observed, and is demonstrated in Fig. 2.16.

This is also in agreement with the prediction based on the tight-binding approximations in reference [Kottos et al. 1996] [Eq. (6)]. We give, in [Manos and Robnik 2015] (Table I), the mean slope σ and the standard deviation of σ, as well as the mean value of the related quantity $2/l_H$ and its standard deviation for various $k = k_0 = 3, 4, 5, \ldots, 19$, for each of them taking seven nearby values of k, namely $k = k_0 \pm j\delta k$, where $j = 0, 1, 2, 3$ and $\delta k = 0.00125$, for matrices of dimension $N = 3000$. Each histogram for all k_0 was fitted with the Gaussian distribution and then the mean values and the standard deviations were extracted. All four quantities decrease to zero with increasing k, meaning

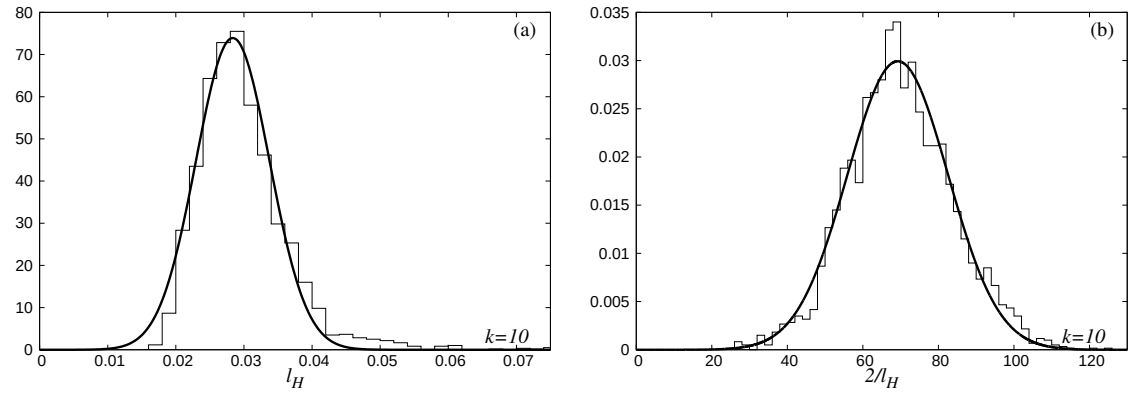

Figure 2.15: Histograms of l_H in (a) and $2/l_H$ in (b) for the system $k = 10$ described by the matrices of dimension $N = 3000$. In both cases we show the Gaussian best fit.

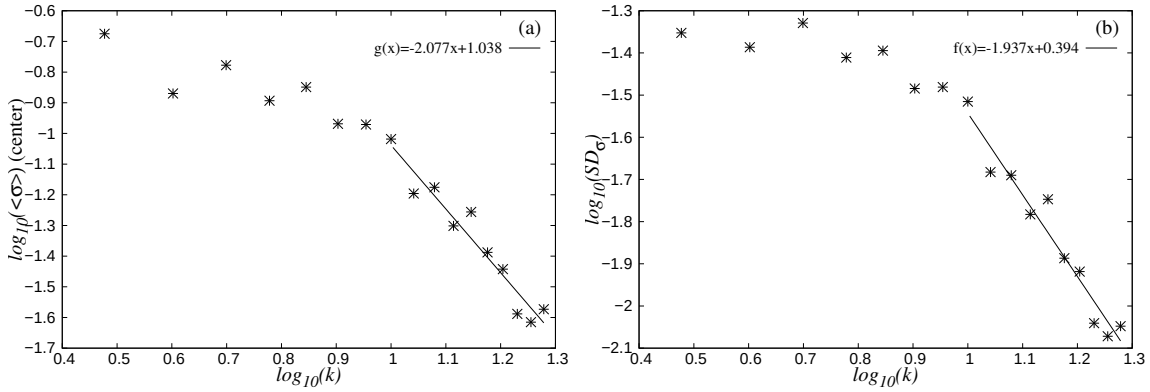

Figure 2.16: Log-log plots in (a) the mean slope $\langle\sigma\rangle$ as a function of k, and in (b) the standard deviation of σ as a function of k. The fitting by a straight line is only on the semiclassical interval $10 \leq k \leq 19$. In the former case the behavior is roughly as $1/k^2$, in agreement with the theoretical estimate $1/k^2$ of Eq. (2.16), and in the latter case also like $1/k^2$, surely not as the theoretical estimate $1/k$ based on the Lyapunov exponents method in [Kottos et al. 1996] [Eq. (9)].

that in the semiclassical limit the localization lengths monotonically increase to infinity, so that in this limit we have asymptotically extended states (no localization), and their standard deviation also goes to zero as $1/k^2$, which is different from the tight-binding approximations in reference [Kottos et al. 1996] [Eq. (9)].

Next we studied how does the distribution of the localization measure σ behaves as a function of the dimension N of the Izrailev model Eqs. (2.22-2.24). Since in the limit $N \to \infty$ the model converges to the infinitely dimensional quantum kicked rotator, we would at first sight expect that following the Shepelyansky picture [Shepelyansky 1986] σ should converge to its asymptotic value, which is sharply defined in the sense that the variance of the distribution of σ goes to zero inversely with N. Namely, at fixed K and k Shepelyansky reduces the problem of calculating the localization length to the problem of the finite time Lyapunov exponents of the approximate underlying finite dimensional Hamilton system with dimension $2k$. The localization length is then found to be equal to the inverse value of the smallest positive Lyapunov exponent. In our case, the dimension of the

matrices N of the Izrailev model plays the role of time. As it is known, and analyzed in detail in [Manos and Robnik 2015], the finite time Lyapunov exponents have a distribution, which is almost Gaussian, and its variance decays to zero inversely with time. Thus on the basis of this we would expect that the variance of σ decays inversely with N.

However, this is not what we observe. In [Manos and Robnik 2015] (Table II) we clearly see that at constant $K = 10$ and $k = 10$ the mean value of σ is constant and obviously equal to its asymptotic value of $N = \infty$, while the variance of σ does not decrease with N, as $1/N$, but is constant instead, independent of N. This is in disagreement with the banded-matrix models of the tight-binding approximations and thus disagrees with the Eq. (9) of reference [Kottos et al. 1996], and also disagrees with the Shepelyansky picture. The reason is that the associated Shepelyansky's Hamilton system is only approximate construction, because with increasing N the matrix elements of the Floquet propagator (matrix) outside the diagonal band of width $2k$ become important, and thus the dimension of the Hamilton system cannot be considered finite, constant and equal to $2k$, but increases with N. As a consequence we have the constant value of the variance of σ, and thus constant variance of the localization length $\mathcal{L} = 2/\sigma$, and therefore the localization length has a distribution with nonvanishing variance even in the limit $N = \infty$. This is precisely the reason why the semiclassical prediction of the localization length in Eq. (2.16) fails in detail and we find strong fluctuations in the plot of $\mathcal{L}$ against the $2/\sigma$ of Figs. 2.6 and 2.13. The proper theory of the localization length must predict its distribution rather than just its approximate mean value. The problem of quantum or dynamical localization is related to the Anderson localization model, within the framework of the tight-binding approximation, with hopping transitions between the nearest neighbors only [Fishman, Grempel, and Prange 1982].

In [Manos and Robnik 2015], we have numerically analyzed the behavior of the finite time Lyapunov exponents for a classical Hamilton system exemplified by the SM, following Fujisaka [Fujisaka 1983] and Ott [Ott 1993] and also for the 2×2 random transfer matrices of the tight-binding approximation to describe the Anderson localization. In both cases we have shown that the distribution of the positive Lyapunov exponent is excellently described by a Gaussian distribution, whose mean value converges with time to the asymptotic value of the infinite time, while the variance decays inversely with time t (the number of iterations in the case of the SM), and n, the number of random matrices in the product. The latter are random unimodular transfer matrices of the tight-binding approximation, of the form:

$$T_n = \begin{pmatrix} W & -1 \\ 1 & 0 \end{pmatrix} \tag{2.47}$$

where $W = E - E_n^0$ is drawn from a distribution, defined by a given model. E is the eigenenergy of the system, and E_n^0 is the fluctuating on-site potential. We have tested three quite different distributions for W, namely Gaussian, box distribution and the Cauchy-Lorentz distribution [Manos and Robnik 2015], and found that the shape of the distribution of the positive Lyapunov exponent for any n (=number of matrices in the product) depends very weakly on the overall shape of the W-distribution, while the mean value and the variance depend only on the variance of W. Indeed, the evidence for the predicted decay of the variance of the finite time Lyapunov exponents is overwhelming, as shown in Fig. 2.17, where we plot the standard deviation as a function of time in log-log plot, showing that it decays inversely with the square root of time.

In the context of our Izrailev model the dimension N of the matrix plays the role of time. The width of the diagonal band is equal to $2k$. Shepelyansky reduces the problem of the localization

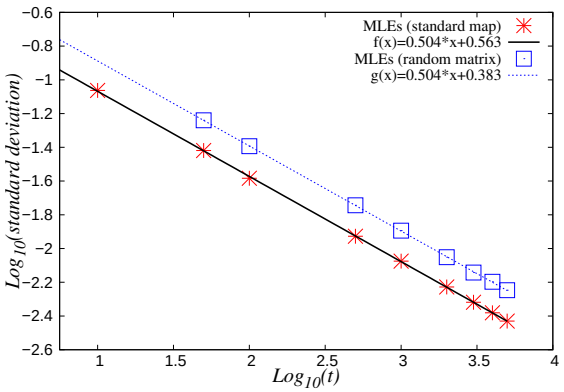

Figure 2.17: The standard deviation of the positive finite time Lyapunov exponents for the SM (stars) and for the product of random transfer matrices with the box distribution of W (empty boxes), as a function of time in log – log presentation, and their best fits. The slope is exactly -1/2.

length to the determination of the smallest positive Lyapunov exponent (its inverse is the localization length) of the underlying finite dimensional Hamilton system with dimension $2k$. Then, the finite time Lyapunov exponent should have some almost Gaussian distribution, whose mean tends to the asymptotic Lyapunov exponent with $N \to \infty$ and the variance should decrease to zero as $1/N$.

If this picture were exact, then the mean localization length as a function of N should converge to the asymptotic value, while the variance does *not* decay to zero, but rather remains constant, independent of N as clearly demonstrated in [Manos and Robnik 2015]. From this we conclude that even in the limit $N \to \infty$ the localization length has a certain distribution with nonvanishing variance, or more precisely, its inverse (the slope σ) has an almost Gaussian distribution with nonvanishing variance. We believe that this is the cause of the strong fluctuations observed for example in Figs. 2.6 and 2.13(a).

2.9 Summary and outlook

We have reviewed some recent results [Manos and Robnik 2013; Batistić, Manos, and Robnik 2013; Manos and Robnik 2014; Manos and Robnik 2015] on the dynamical localization in the N-dimensional Izrailev model. The analysis of the classical system (SM) and of the quantum kicked rotator has been performed for many different values of the classical kick parameter K on the interval $[K_{cr}, 70] \approx [0.97, 70]$, of the quantum parameter k and matrix dimensions N in the interval $[400, 3000]$. The aspects of classical generally anomalous diffusion have been studied and the important relevance of the accelerator modes were elucidated, and the semiclassical approximation for the average localization length $\mathcal{L}$ has been derived. The entropy localization measure l_H [Eq. 2.29] has been calculated, and the corresponding parameter $\beta_{\rm loc} = \langle l_H \rangle / N$ was defined. The scaling law of $\beta_{\rm loc}$ versus $\Lambda = \mathcal{L}/N$ was found, in agreement with previous results, e.g. see [Izrailev 1990] and references therein. However, even after a great numerical effort in maximally improving the statistical relevance of this scaling law, large fluctuations around the mean value have been observed. Also, we have shown, that the Brody distribution describes the energy level spacing distribution very well, and the spectral Brody parameter $\beta_{\rm BR}$, determining the level spacing distribution, was found to be linearly related to $\beta_{\rm loc}$.

The main conclusion of our analysis is the empirical fact based on numerical computations of the

eigenfunctions of the N-dimensional Izrailev model, that the localization length has a distribution with nonvanishing variance not only for finite N, but even in the limit $N \to \infty$. This is the reason, we believe, for the strong fluctuations in the scaling laws which involve the empirical localization measures and the theoretical semiclassical value of the localization length. In the Shepelyansky picture [Shepelyansky 1986] this might seem to be a contradiction, but the resolution of the puzzle is that in the limit of large N the finite dimensional Hamiltonian system extracted from the Floquet propagator of the quantum kicked rotator is not good enough, and therefore the matrix elements outside the main diagonal band of width $2k$ play a role, even if they are small, but nevertheless plentiful, making the Hamiltonian system effectively infinite dimensional, with infinitely many Lyapunov exponents. This finding is a challenge for the improved semiclassical theory of the localization length, to derive and explain the discovered distribution function.

On the other hand, the simple model of the Anderson localization based on the tight-binding approximation, with only nearest neighbor interactions, described by the product of 2×2 unimodular matrices, has a finite dimension, as the transfer matrices are exactly two-dimensional, and therefore the variance vanishes in the limit of large times n (number of matrices in the product) as $1/n$. The same conclusion applies to such a model with a finite number of interacting neighbors. Indeed, according to e.g. [Kottos et al. 1996] the variance of σ should vanish as $Var(\sigma) \propto 1/(Nk^2)$, but our work shows that in the quantum kicked rotator this is not observed: the variance does not depend on N, and decays with k faster than $1/k^2$, namely as $1/k^4$. Thus, we found some important differences between the dynamical localization in the quantum kicked rotator and the Anderson tight-binding model of localization, and the Shepelyansky picture, which rest upon the banded matrix models with rigorously finite bandwidth.

Perspectives

The problem of calculating the distribution of the localization length (or its inverse) in the semiclassical framework is open for the future work. Also, the theoretical derivation of the Brody distribution to explain the level spacing distribution of the energies [Batistić and Robnik 2010; Batistić and Robnik 2013a; Batistić and Robnik 2013b] in time-independent systems, and of the quasienergies [Izrailev 1990; Manos and Robnik 2013; Batistić, Manos, and Robnik 2013] in time-periodic systems, of chaotic eigenstates, is still open for the future.

Furthermore, in the classical kicked rotor model, one can extend these findings on diffusion properties and potential scaling laws for 1D and 2D lattices and investigate how the fraction of the chaotic, regular motion along with the presence of accelerator modes may impact systems with more complex configurations, e.g. when varying the system size, the kick parameter per rotor and coupling type and strength within the lattice [Moges H., Manos T. and Skokos Ch., "Anomalous diffusion and chaotic motion in standard map lattices" (in preparation), 2020].

Chapter 3

Complex neuronal activity patterns in the human brain

3.1 Background and introduction

Synchronization of oscillations is a generic mechanism in animate and inanimate systems (see e.g. [A. Pikovsky, Rosenblum, and Jürgen Kurths 2003]). In fact, oscillators of qualitatively different type may share fundamental synchronization mechanisms. Synchronization processes may occur within as well as between different systems of the human body, e.g. between heartbeat intervals and respiratory cycles [Bartsch et al. 2012]. Neuronal synchronization processes are relevant under normal as well as abnormal conditions. A number of brain disorders are associated with abnormal neuronal synchrony, for example Parkinson's disease (see e.g. [Lenz et al. 1994; Nini et al. 1995; Hammond, Bergman, and Brown 2007]), tinnitus (see e.g. [Ochi and Eggermont 1997; Eggermont and P. A. Tass 2015; Elgoyhen et al. 2015]), migraine (see e.g. [Angelini et al. 2004; Bjørk and Sand 2008]) and epilepsy (see e.g. [Wong, Traub, and Miles 1986]). Neuronal dynamics and, in particular synchronization processes, crucially depend on the patterns and types of neuronal connections [Sporns 2011]. For instance, according to computational studies it makes a significant difference whether neurons interact through gap-junctions or synapses. This is relevant for the emergence of different kinds of synchronization patterns [Esfahani, Gollo, and Valizadeh 2016] and epileptic seizures [Volman, Perc, and Bazhenov 2011].

Connectivity and function are strongly connected and may undergo plastic changes throughout the life course [Hübener and Bonhoeffer 2014]. The timing pattern of neuronal activity may strongly determine the strength of neuronal connections [Bliss and Lømo 1973]. Spike-timing-dependent plasticity (STDP) is a pivotal mechanism by which neurons adapt the strength of their synapses to the relative timing of their action potentials (see e.g. [H. Markram, W. Gerstner, and Sjostrom 2012]). Based on seminal experimental studies [Henry Markram et al. 1997] a series of computational studies focused on how adaptive coupling and activity dependent synaptic strength influence the collective neuronal dynamics was performed. In the presence of STDP a plethora of qualitatively different stable dynamical regimes emerge [Zhang et al. 2013]. In fact, multistability (the coexistence of multiple attractors in the phase space) is a typical feature of neuronal networks and oscillator networks equipped with STDP. Multistability was found in different neural network models comprising different STDP models, e.g. in phase oscillator networks with both symmetric and asymmetric phase difference-dependent plasticity, a time continuous approximation of STDP [Maistrenko et al. 2007] as well as in phase oscillator networks with STDP and in different types of neuronal networks with STDP [Pfister and P. Tass 2010; O.V. Popovych and P. Tass 2012; Ebert, Hauptmann, and P. Tass 2014] and other types of neural network models (e.g. [Proix et al. 2017] and references therein).

A number of computational studies were dedicated on desynchronizing synchronized ensembles or

networks of oscillators or neurons [Winfree 1980; P. A. Tass 1999]. The clinical need for stimulation techniques that cause desynchronization irrespective of the network's initial state [P. A. Tass 2001], thereby being reasonably robust against variations of system parameters and, hence, not requiring time-consuming calibration, motivated the design of the so-called Coordinated Reset (CR) stimulation [P. A. Tass 2003b; P. A. Tass 2003a]. CR stimuli aim at disrupting in-phase synchronized neuronal populations by delivering phase resetting stimuli typically equidistantly in time, separated by time differences T_s/N_s, where T_s is the duration of a stimulation cycle, and N_s is the number of active stimulation sites [P. A. Tass 2003b; P. A. Tass 2003a]. The spatiotemporal sequence by which all stimulation sites are activated exactly once in a CR stimulation cycle is called the stimulation site sequence, or briefly sequence. Taking into account STDP in oscillatory neural networks qualitatively changed the scope of the desynchronization approach: Computationally it was shown that CR stimulation reduces the rate of coincident firing and, mediated by STDP, also decreases the average synaptic weight, ultimately preventing the network from generating abnormally increased synchrony. This *anti-kindling*, i.e., unlearning of abnormally strong synaptic connectivity and of excessive neuronal synchrony, causes long-lasting sustained effects that persist cessation of stimulation. As shown computationally, anti-kindling can robustly be achieved in networks with plastic excitatory and inhibitory synapses, no matter whether CR stimulation is administered directly to the soma or through synapses [O.V. Popovych and P. Tass 2012; P. A. Tass and O. Popovych 2012]. In line with these computational findings, long-lasting CR-induced desynchronization and/or therapeutic effects were accomplished with invasive as well as non-invasive stimulation modalities.

Long-lasting desynchronization was induced by electrical CR stimulation in rat hippocampal slices rendered epileptic by magnesium withdrawal [P. Tass, A. Silchenko, et al. 2009]. Electrical CR deep brain stimulation (DBS) caused long-lasting therapeutic after-effects in parkinsonian non-human primates. Bilateral therapeutic after-effects for at least 30 days were caused by unilateral CR stimulation delivered to the subthalamic nucleus (STN) of parkinsonian MPTP monkeys for only 2 h per day during 5 consecutive days. In contrast, standard permanent high-frequency deep brain stimulation did not induce any sustained after-effects (see e.g. [P. Tass, Adamchic, et al. 2009]). In patients with Parkinson's disease electrical CR-DBS delivered to the STN caused a significant and cumulative reduction of abnormal beta band oscillations along with a significant improvement of motor function [Adamchic, Hauptmann, et al. 2014]. Non-invasive, acoustic CR stimulation was developed for the treatment of patients suffering from chronic subjective tinnitus [P. A. Tass and O. Popovych 2012; P. A. Tass, Qin, et al. 2012a]. In a proof of concept-study acoustic CR stimulation caused a statistically and clinically significant sustained reduction of tinnitus symptoms [P. A. Tass, Qin, et al. 2012a; Adamchic, Langguth, et al. 2012] together with a concomitant decrease of abnormal neuronal synchrony [Adamchic, Toth, Hauptmann, and P. A. Tass 2014], abnormal effective connectivity [A. N. Silchenko et al. 2013] as well as abnormal cross-frequency coupling [Adamchic, Langguth, et al. 2014] within a tinnitus-related network of brain areas (see [Manos, Zeitler, and P. A. Tass 2018a] and references therein).

So far, the pre-clinical [P. Tass, A. Silchenko, et al. 2009; P. A. Tass, Qin, et al. 2012a] and clinical [P. Tass, Adamchic, et al. 2009; Adamchic, Hauptmann, et al. 2014] proof of concept studies for invasive and non-invasive CR stimulation were driven by computationally derived hypotheses and predictions. Theoretically predicted phenomena and mechanisms, such as long-lasting stimulation effects [Peter A. Tass and Majtanik 2006; O.V. Popovych and P. Tass 2012; Hauptmann and P. A. Tass 2007], cumulative stimulation effects [Hauptmann and P. A. Tass 2009], and improvement by weak stimulus intensity [Lysyansky, O. V. Popovych, and P. A Tass 2011], were verified based on

dedicated theory-driven study protocols for pre-clinical and clinical proof of concepts [P. Tass, A. Silchenko, et al. 2009; P. Tass, Adamchic, et al. 2009; P. A. Tass, Qin, et al. 2012a; Adamchic, Hauptmann, et al. 2014].

3.2 Investigation goals, hypotheses and protocols

In this chapter, we set out to investigate the impact of the CR stimulation frequency and intensity on the effects during stimulus delivery (so-called *acute effects*), on transient effects emerging directly after cessation of stimulation (so-called *acute after-effects*), and on effects outlasting cessation of stimulation (so-called *sustained after-effects*). The ultimate goal of this study is to improve the calibration of CR stimulation, in particular, by providing computationally generated predictions that can be tested in subsequent pre-clinical and clinical studies. The computational study presented here is organized around three hypotheses:

- Hypothesis #1: Due to the inherently periodic structure of CR stimulation the relation between CR stimulation frequency and the spontaneous neuronal firing rates (prior to stimulation) matters. Periodic delivery of CR stimuli with fixed sequence basically constitutes a time-shifted entrainment of the different neuronal subpopulations [P. A. Tass 2003b; P. A. Tass 2003a]. A particular closed loop embodiment of CR stimulation, periodic stimulation with demand-controlled length of high-frequency pulse train, is basically a time-shifted entrainment of the different neuronal subpopulations with stimulus intensities adapted to the amount of undesired synchrony. Accordingly, the duration of a stimulation cycle was selected to be reasonably close to the mean period of the synchronized neuronal oscillation. In STDP-free networks of Kuramoto [Kuramoto 1984] and FitzHugh-Nagumo [Fitzhugh 1961] model neurons the impact of CR stimulation intensity and frequency on the desynchronizing outcome of CR was studied in detail [Lysyansky, O. V. Popovych, and P. A Tass 2011].

- Hypothesis #2: Different embodiments of CR stimulation may differ with respect to effect size and robustness. In a series of computational studies (see e.g. [P. A. Tass 2003b; P. A. Tass 2003a] and references therein) and in all pre-clinical [P. Tass, A. Silchenko, et al. 2009; P. Tass, Adamchic, et al. 2009] and clinical studies [P. A. Tass, Qin, et al. 2012b; Adamchic, Langguth, et al. 2012; damchic et al. 2012; Adamchic, Hauptmann, et al. 2014; Adamchic, Toth, Hauptmann, and P. A. Tass 2014; A. N. Silchenko et al. 2013] performed so far, CR was applied either with fixed sequences or rapidly varying sequences (RVS), where the sequence was randomly varied from cycle to cycle. In a recent computational study, it was shown that at intermediate stimulation intensities the CR-induced anti-kindling effect may significantly be improved by CR with slowly varying sequences (SVS), i.e. by appropriate repetition of the sequence with occasional random switching to the next sequence [Zeitler and P. A. Tass 2015]. However, this study was not performed for a larger range of CR stimulation frequencies. By definition, SVS CR stimulation features significantly more periodicity of the stimulus pattern. Accordingly, the dependence of resonance and/or anti-resonance effects on the CR stimulation frequency might be more pronounced for SVS CR as opposed to RVS CR.

- Hypothesis #3: Pronounced acute effects might provide a necessary, but not sufficient condition for pronounced sustained after-effects. In a pre-clinical study in Parkinsonian monkeys with CR-DBS delivered at an optimal and a less favorable intensity, it was shown that long

and pronounced acute therapeutic after-effects coincide with long-lasting, sustained after-effects [P. A. Tass, Qin, et al. 2012a]. However, according to computational studies the relationship between acute after-effects and sustained long-lasting effects might be more involved, at least for particular parameter combinations [Zeitler and P. A. Tass 2015].

Related to these hypotheses, to assess the robustness of CR stimulation against initial network conditions we performed our numerical simulations for different network initializations. Here, we did not systematically vary the stimulation duration. Rather, based on a pre-series of numerical simulations, we here used a fixed stimulation duration that is reasonably short, but nevertheless enabled to robustly achieve an anti-kindling for properly selected values of stimulation frequency and intensity. In fact, our goal was to find stimulation parameters enabling short, but notwithstanding effective CR stimulation. Keeping the stimulation duration at moderate levels may be beneficial for applying the CR approach to different invasive as well as non-invasive stimulation modalities. For instance, standard high frequency (HF) DBS, i.e. permanent electrical high-frequency pulse train stimulation delivered to dedicated target areas through implanted depth electrodes, used for the treatment of, e.g. Parkinson's disease [Benabid et al. 1991; Krack et al. 2003; Deuschl et al. 2006] may cause side effects. If side effects are caused by stimulation of non-target tissue, they may be reduced by adapting the spatial extent of the current spread to the target's anatomical borders by appropriate electrode designs as introduced, e.g. by [Martens et al. 2011; Dijk et al. 2015; Bour et al. 2015], in particular, to spatially tailor stimuli by means of directional DBS (see e.g. [Contarino et al. 2014]). However, some side effects may, at least partly, be caused by stimulating the target region itself (see e.g. [Jahanshahi et al. 2015]. Accordingly, no matter how precisely stimuli are delivered to DBS targets, the amount of stimulation should be decreased as much as possible.

HF DBS may not only cause side effects by electrical current spreading outside of the target region, but also by chronic stimulation of the target itself or by functional disconnection of the stimulated structure (see e.g. [Ferraye et al. 2008]). Accordingly, it is key to reduce the integral stimulation current. Electrical CR stimulation of the STN employs significantly less current compared to HF DBS [P. A. Tass, Qin, et al. 2012b; Adamchic, Hauptmann, et al. 2014; J. Wang et al. 2016]. However, to further improve the CR approach, in a previous computational study the spacing principle [Ebbinghaus, Bussenius, and Ruger 1913] was used to achieve an anti-kindling at subcritical intensities, i.e. particularly weak intensities rendering permanently delivered CR stimulation ineffective [O. V. Popovych, Xenakis, and P. A. Tass 2015]. According to the spacing principle [Ebbinghaus, Bussenius, and Ruger 1913], learning effects can be improved by repeated stimuli spaced by pauses as opposed to delivering a massed stimulus in a single long stimulation session. Spaced CR stimulation at subcritical intensities might possibly be applied to CR DBS. However, for clinical applications, in particular, for non-invasive applications of CR stimulation, such as acoustic CR stimulation for tinnitus or vibrotactile stimulation for PD, it is crucial to achieve therapeutic effects within a reasonable amount of time. Applications of non-invasive *medtech* devices typically rely on the patients' compliance and should favorably require short stimulation durations. Accordingly, we here set out to apply the spacing principle to CR stimulation at supercritical intensities, i.e. intensities that enable an anti-kindling for moderate stimulation duration and properly selected stimulation frequencies. The overall goal is to design short-term dosage regimen that improve CR stimulation efficacy, while keeping the integral amount of stimulation as well as the overall duration of the protocols at comparably low levels.

To come up with favorable combinations of stimulation parameters, in our numerical study we

used different data analysis methods, e.g. macroscopic measures assessing the average amount of the population's synchrony and synaptic connectivity. These measures are appropriate to demonstrate relevant stimulation effects, such as stimulation-induced transitions from pronounced neuronal synchrony to desynchronized states.

To establish a pharmacological treatment for clinical use, in humans typically a 4-phase sequence of clinical trials is performed [Friedman, Furberg, and Demets 2010]. In pre-clinical studies pharmacokinetic, toxicity and efficacy are studied in non-human subjects. In human-studies (*phase I*) safety and tolerability of a drug are studied in healthy volunteers. Proof of concept studies (*phase IIA*) determine whether a drug can have any efficacy, whereas dose-finding studies (*phase IIB*) are performed to reveal optimum dose at which a drug has biological activity with minimal side-effects. Effectiveness and the clinical value of a new intervention are studied in a randomized controlled trial (*phase III*), compared with state of the art treatment, if available. Finally, post-marketing surveillance trials (*phase IV*) are performed to detect rare or long-term adverse effects within a much larger patient population and over longer time periods. There might also be combinations of different phases.

In principle, this 4-phase pattern is also valid for medical technology, e.g. neuromodulation technologies. However, if neuromodulation technologies aim at the control of complex dynamics of e.g. neural networks, different parameters and dosage regimens may have complex, non-linear and even counterintuitive effects, see e.g. [O. V. Popovych, Xenakis, and P. A. Tass 2015]. The latter work illustrates how computational modelling can be used to generate hypotheses for dose-finding studies. In general, performing dose-finding studies simply by trial and error may be impossible because of the substantial parameter space to be tested, with trial durations and related costs getting out of hands.

The development of proper dosage strategies and regimens enables favorable compromises between therapeutic efficacy and detrimental factors such as side-effects or treatment duration. This is relevant, e.g. for the development of pharmaceutical [Dash, Singh, and Tolman 2014] or radiation therapy [Symonds et al. 2012]. DBS is the standard treatment of medically refractory movement disorders [Benabid et al. 1991; Krack et al. 2003; Deuschl et al. 2006]. The clinical [Temperli et al. 2003] and electrophysiological [Kühn, Kempf, et al. 2008] effects of standard HF DBS occur only during stimulation and cease after stimulation offset.

In [Manos, Zeitler, and P. A. Tass 2018a], we studied the influence of the CR stimulation frequency and the intensity on the outcome of CR stimulation with RVS and SVS [Zeitler and P. A. Tass 2015]. CR stimulation consists of sequences of stimuli delivered to each sub-population. For RVS CR stimulation, the CR sequence is randomly varied from one CR stimulation period to another [Peter A. Tass and Majtanik 2006]. Conversely, SVS CR stimulation is characterized by repeating a sequence for a number of times before randomly switching to the next sequence. In [Manos, Zeitler, and P. A. Tass 2018a], we demonstrated that the efficacy of singleshot CR stimulation with moderate stimulation duration depends on the stimulation parameters, in particular, on the intensity as well as the relationship between CR stimulation frequency and intrinsic firing rates. RVS CR stimulation turned out to induce pronounced long-lasting desynchronization, e.g. at weak intensities and CR stimulation frequencies in a certain range around the neurons' intrinsic firing frequencies. In contrast, SVS CR stimulation enabled even more pronounced anti-kindling, however, at the cost of a significantly stronger dependence of the stimulation outcome on the CR stimulation frequency. Dosage regimen design is an integral part of pharmacokinetic methodology, aiming at an optimization of drug delivery and effects [Williams 1992]. By a similar token, we hypothesize that appropriate dosage regimens might further enhance the efficacy of RVS and SVS CR stimulation. To probe different dosage regimens, we considered different stimulation singleshot and multishot

CR stimulation protocols. Protocols A and B have identical integral stimulation duration, whereas Protocols C and D may require less stimulation.

Protocol A: Spaced multishot CR stimulation with fixed stimulation parameters. Instead of one singleshot CR stimulation we deliver the identical CR shot five times, where the duration of each single pause equals the duration of each identical singleshot. Intersecting singleshot stimuli by pauses to increase stimulation efficacy, resembles the so-called spacing principle, a learning-related mechanism that is well-established in psychology [Ebbinghaus, Bussenius, and Ruger 1913], education [Kelley and Whatson 2013], and neuroscience [Naqib, Sossin, and Farah 2012]. According to the spacing principle, learning effects can be enhanced by delivering a stimulus in a spaced manner, as opposed to administering a massed stimulus in a single long stimulation session. Computationally, it was shown that subcritical CR stimulation at subcritical (ineffective) intensities may become effective if intersected by rather long pauses and delivered sufficiently often, e.g. eight times [O. V. Popovych, Xenakis, and P. A. Tass 2015]. However, shorter pauses were not sufficient. As yet, spaced CR stimulation at supercritical intensities was not studied. Here, we focus on comparably short stimulation protocols. Accordingly, we use CR stimulation of sufficient intensity and deliver five single CR shots intersected by pauses. We consider a symmetric dosage regimen, with identical duration of single shots and pauses.

Protocol B: Long singleshot CR stimulation with fixed stimulation parameters. To assess the impact of the spacing principle, as a control condition we simply stimulate five times longer, without any pause and with stimulation parameters kept constant. Protocol B is shorter, but employs the same integral stimulation duration as Protocol A.

Protocol C: Spaced multishot CR stimulation with demand-controlled variation of the CR stimulation frequency and intensity. As in Protocol A, we deliver spaced CR stimulation comprising five identical CR shots, intersected by pauses, where all shots and pauses are of equal duration. However, at the end of each CR shot we monitor the stimulation effect and perform a three-stage control: (i) If no pronounced desynchronization is achieved, the CR stimulation frequency of the subsequent CR shot is mildly varied by no more than $\pm 3\%$. (ii) If an intermediate desynchronization is observed, the CR stimulation frequency remains unchanged and CR stimulation is continued during the subsequent shot. (iii) If a pronounced desynchronization is achieved, no CR stimulation is delivered during the subsequent shot. Note, for stage (i) we do not adapt the CR stimulation frequency to a measured quantity. We consider two different variation types employed for stage (i): with regular and with random variation of the CR stimulation frequency. Regular variation means to increase or decrease the CR stimulation frequency in little unit steps. In contrast, random variation stands for randomly picking the CR stimulation frequency from a restricted interval.

Protocol D: Long singleshot CR stimulation with demand-controlled variation of the stimulation frequency. To assess the specific pausing-related impact of the evolutionary spacing principle, as a direct control condition we perform Protocol C without pauses. To this end, we string five CR shots together, without pauses, and evaluate the stimulation effect at the end of each CR shot. If no pronounced desynchronization is achieved, the CR stimulation frequency is slightly varied by no more than $\pm 3\%$ for the subsequent CR shot. During each single CR shot stimulation parameters are kept constant. Only from one CR shot to the next the CR stimulation frequency can be varied. Overall, Protocol D is shorter than Protocol C, but uses the same integral stimulation duration as in Protocols A-C.

CR stimulation and, especially, SVS CR stimulation has pronounced periodic characteristics. Accordingly, the CR stimulation frequency turned out to be a sensitive parameter, in particular, for

SVS CR stimulation (see [Manos, Zeitler, and P. A. Tass 2018a]). For this reason, for stage (i) of Protocol C and D we perform a demand-controlled variation of the CR stimulation frequency to prevent from, e.g. unfavorable resonances or phase locking dynamics. Note these demand-controlled changes of the CR stimulation frequency are mild and hardly change the networks' firing rates.

In [Manos, Zeitler, and P. A. Tass 2018b], we tested the performance of the different Protocols A-D by selecting unfavorable stimulation parameters, which render CR stimulation ineffective according to [Manos, Zeitler, and P. A. Tass 2018a]. By design, Protocols C and D work well for all parameter pairs (K, T_s) related to effective singleshot CR stimulation. In that case, CR stimulation actually ceases due to lack of demand. Note, in all four stimulation protocols we keep the stimulation intensity fixed. Only Protocols C and D require feedback of the stimulation outcome.

3.3 The Hodgkin-Huxley spiking neuron model

In this study we use the conductance-based Hodgkin-Huxley neuron model [Hodgkin and Huxley 1952] for the description of an ensemble of spiking neurons. The set of equations and parameters read (see [Hansel, Mato, and Meunier 1993; O.V. Popovych and P. Tass 2012]):

$$C\frac{dV_i}{dt} = I_i - g_{Na}m_i^3 h_i(V_i - V_{Na}) - g_K n_i^4(V_i - V_K) - g_l(V_i - V_l) + S_i + F_i \tag{3.1}$$

$$\frac{dm_i}{dt} = \alpha_m(V_i)(1 - m_i) - \beta_m(V_i)m_i \tag{3.2}$$

$$\frac{dh_i}{dt} = \alpha_h(V_i)(1 - h_i) - \beta_h(V_i)h_i \tag{3.3}$$

$$\frac{dn_i}{dt} = \alpha_n(V_i)(1 - n_i) - \beta_n(V_i)n_i \tag{3.4}$$

The variable V_i with $i = 1, \ldots, N$, describes the membrane potential of neuron i, and:

$$\alpha_m(V) = (0.1V + 4)/[1 - \exp(-0.1V - 4)], \tag{3.5}$$

$$\beta_m(V) = 4\exp[\frac{-V - 65}{18}], \tag{3.6}$$

$$\alpha_h(V) = 0.07\exp[\frac{-V - 65}{20}], \tag{3.7}$$

$$\beta_h(V) = \frac{1}{[1 + \exp(-0.1V - 3.5)]}, \tag{3.8}$$

$$\alpha_n(V) = \frac{0.01V + 0.55}{[1 - \exp(-0.1V - 5.5)]}, \tag{3.9}$$

$$\beta_n(V) = 0.125\exp[\frac{-V - 65}{80}]. \tag{3.10}$$

The total number of neurons is $N = 200$, while $g_{Na} = 12$ mS/cm^2, $g_K = 36$ mS/cm^2, $g_l = 0.3$ mS/cm^2 are the maximum conductance per unit area for the sodium, potassium and leak currents respectively. The constants $V_{Na} = 50$ mV, $V_K = -77$ mV and $V_l = -54.4$ mV refer to the sodium, potassium and leak reversal potentials respectively. C is the constant membrane capacitance ($C = 1$ μF/cm^2), I_i the constant depolarizing current injected into neuron i, determining the intrinsic firing rate of the uncoupled neurons. For the realization of different initial networks, we used random initial

conditions drawn from uniform distributions, i.e. $I_i \in [I_0 - \sigma_I, I_0 + \sigma_l\ ]$ ($I_0 = 11.0\ \mu\text{A/cm}^2$ and $\sigma_l = 0.45\ \mu\text{A/cm}^2$), $h_i, m_i, n_i \in$ [0,1] and $V_i \in [-65, 5]$ mV. The initial values of the neural synaptic weights c_{ij} are picked from a normal distribution $N(\mu_c = 0.5\ \mu\text{A/cm}^2, \sigma_c = 0.01\ \mu\text{A/cm}^2)$. Hence, in this setup the neurons are not identical. The S_i term refers to the internal synaptic input of the neurons within the network to neuron i, while F_i represents the current induced in neuron i by the external CR stimulation. In addition, in order to model variations of the model parameters, we add a sinusoidal external current input of the form $I_{var} = A \cdot \sin(2\pi \cdot f \cdot t)$ to the right-hand side of Eq. (3.2), where f and A are the frequency and the amplitude of the signal respectively.

3.4 Network and neuron coupling description

The $N = 200$ spiking Hodgkin-Huxley neurons are placed on a ring and the $N_s = 4$ stimulations sites are equidistantly placed in space at the positions of neurons $i = 25, 75, 125, 175$. The neurons interact via excitatory and inhibitory chemical synapses by means of the postsynaptic potential (PSP) s_i which is triggered by a spike of neuron i [Wulfram Gerstner et al. 1996; Izhikevich 2005] and modelled using an additional equation:

$$\frac{ds_j}{dt} = \frac{0.5\,(1 - s_j)}{1 + \exp\left[-\left(V_j + 5\right)/12\right]} - 2s_j. \tag{3.11}$$

Initially we draw $s_i \in [0\ ,\ 1\ ]$ (randomly from a uniform distribution). The coupling term S_i from Eq. (3.1) (see [O.V. Popovych and P. Tass 2012]) contains a weighted ensemble average of all postsynaptic currents received by neuron i from the other neurons in the network:

$$S_i = N^{-1} \sum_{j=1}^{N} \left(V_{r,j} - V_i\right) c_{ij} |M_{ij}| s_j, \tag{3.12}$$

where $V_{r,j}$ is the reversal potential of the synaptic coupling (20 mV for excitatory and –40 mV for inhibitory coupling), and c_{ij} is the synaptic coupling strength from neuron j to neuron i. There are no neuronal self-connections within the network ($c_{ii} = 0\ \text{mS/cm}^2$). The variable:

$$M_{ij} = \left(1 - \frac{d_{ij}^2}{\sigma_1^2}\right) \exp\left(-\frac{d_{ij}^2}{\left(2\sigma_2^2\right)}\right) \tag{3.13}$$

describes the spatial profile of coupling between neurons i and j and is of a Mexican hat-type [Wilson H. R 1973; Dominguez et al. 2006; Rocha et al. 2008] with strong short-range excitatory ($M_{ij} > 0$) and weak long-range inhibitory interactions ($M_{ij} < 0$). Here $d_{ij} = d|i - j|$ is the distance between neurons i and j, while:

$$d = \frac{d_0}{N - 1} \tag{3.14}$$

determines the distance on the lattice between two neighboring neurons within the ensemble. d_0 is the length of the neuronal chain $d_0 = 10$. $\sigma_1 = 3.5$, and $\sigma_2 = 2.0$. In order to limit boundary effects, we consider that the neurons are distributed in such a way that the distance d_{ij} is taken as: $d \cdot min\left(|i - j|, N - |i - j|\right)$ for $i, j > N/2$.

Spike-Timing-Dependent Plasticity

The synaptic weights c_{ij} are dynamical variables that depend on the time difference, $\Delta t_{ij} = t_i - t_j$, between the onset of the spikes of the post-synaptic neuron i and the pre-synaptic neuron j, denoted by t_i and t_j , according to [Bi and Poo 1998; O.V. Popovych and P. Tass 2012]:

$$\Delta c_{ij} = \begin{cases} \beta_1 e^{\frac{-\Delta t_{ij}}{\gamma_1 \tau}}, & \Delta t_{ij} \geq 0 \\ \beta_2 \frac{\Delta t_{ij}}{\tau} e^{\frac{\Delta t_{ij}}{\gamma_2 \tau}}, & \Delta t_{ij} < 0 \end{cases} \tag{3.15}$$

with parameters $\beta_1 = 1$, $\beta_2 = 16$, $\gamma_1 = 0.12$, $\gamma_2 = 0.15$, $\tau = 14$ ms and $\delta = 0.002$, According to the value of Δt_{ij}, the synaptic weight c_{ij} is updated in an event-like manner, i.e. we add or subtract an increment $\delta \dot{c}_{ij}$ for excitatory or inhibitory connections respectively, with learning rate $\delta > 0$ every time a neuron spikes. Furthermore, we restrict the values of c_{ij} on the interval [0,1] mS/cm^2 for both excitatory and inhibitory synapses, ensuring in this way that their strengthening or weakening remains bounded. The maximal inhibitory synaptic weight cmax was set to be 1 in all our stimulations.

The time window of the plasticity is adjusted with respect to the intrinsic firing rate of the neuron population in order to exhibit multistability. There, different time-windows (via different choices of parameters) were selected for the STDP for two different neuron models, i.e. one with bursting neurons (FitzHugh-Rinzel) and one for spiking neurons (Hodgkin-Huxley). In our simulations, the STDP tends to simply stabilize the ongoing ensemble evolution and does not, by itself, (de-)synchronize the network. The parameters were, in general, chosen such that the ratio $\frac{\Delta t_{ij}}{\gamma_{1,2}\tau}$ is normalized, and the plasticity takes place within a time interval associated with the spiking period of the individual neurons. We analyzed two additional cases for small variation of the plasticity time-window ($\tau = 12$ and $\tau = 16$) and obtained very similar general effects. The selected fixed value $\tau = 14$, used throughout the entire study, also allows us to compare our results with previously published studies.

Coordinated Reset Stimulation

Coordinated Reset (CR) stimulation was applied to the neuronal ensemble of N spiking Hodgkin-Huxley neurons. This was done sequentially via N_s (= 4 in this study) equidistantly spaced stimulation sites [P. A. Tass 2003a]: one stimulation site was active during T_s/N_s , while the other stimulation sites were inactive during that period. After that another stimulation site was active during the next T_s/N_s period. All N_s stimulation sites were stimulated exactly once within one stimulation ON-cycle. Therefore, the duration of each ON-cycle is T_s (in ms). The spatiotemporal activation pattern of stimulation sites is represented by the indicator functions $\rho_k(t)(k \in [1, \ldots, N])$, taking the value 1 when the k^{th} stimulation site is active at t and 0 else.

The stimulation signals induced single brief excitatory post-synaptic currents. The evoked time-dependent normalized conductances of the postsynaptic membranes are represented by α-functions as follows [O.V. Popovych and P. Tass 2012]:

$$G_{stim}(t) = \frac{t - t_k}{\tau_{stim}} e^{-(t-t_k)/\tau_{stim}}, t_k \leq t \leq t_{k+1}. \tag{3.16}$$

Here $\tau_{stim} = \frac{T_s}{6N_s}$ denotes the time-to-peak of G_{stim}, and t_k is the onset of the k^{th} activation of the stimulation site. Note that the period (or frequency) through the τ_{stim} parameter of the CR

stimulation determines not only the random onset timing of each single signal but also its temporal duration. The spatial spread of the induced excitatory postsynaptic currents in the network is defined by a quadratic spatial decay profile given as a function of the difference in index of neuron i and the index x_k of the neuron at stimulation site k:

$$D\left(i, x_k\right) = \frac{1}{1 + d^2 \left(i - x_k\right)^2 / \sigma_d^2}, \tag{3.17}$$

with d the lattice distance between two neighboring neurons as defined in Eq. (3.14) and $\sigma_d = 0.8$ the spatial decay rate of the stimulation current. Thus the total stimulation current is expressed by the following equations:

$$F_i = \left[V_r - V_i\left(t\right)\right] \cdot K \sum_{k=1}^{N_s} D\left(i, x_k\right) \rho_k\left(t\right) G_{stim}\left(t\right), \tag{3.18}$$

where $V_r = 20$ mV denotes the excitatory reversal potential, V_i the membrane potential of neuron i, K the stimulation intensity, and ρ, G, D as described above.

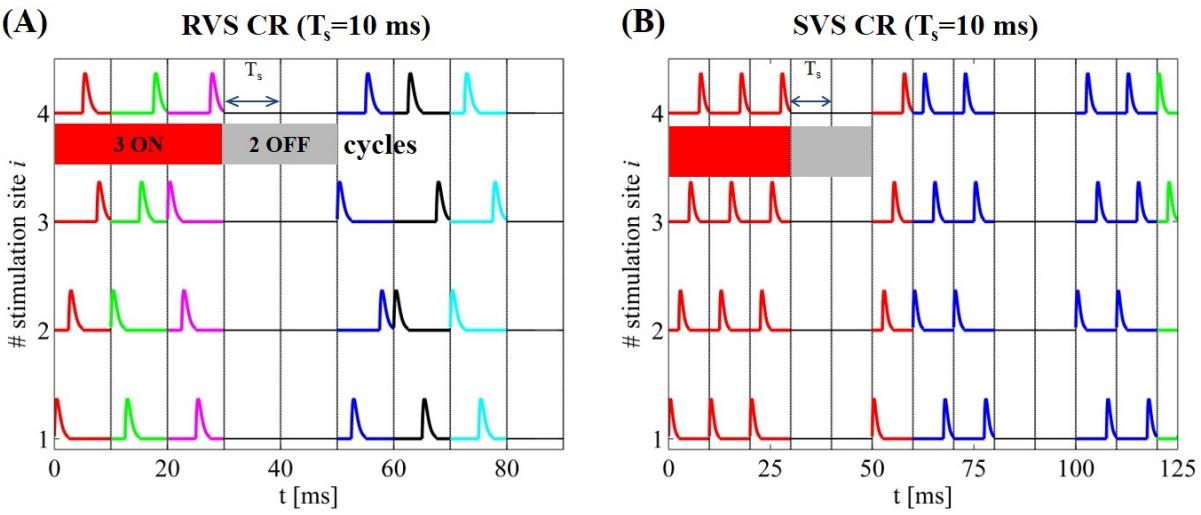

Figure 3.1: Time evolution of CR stimulation signals. (A) RVS CR stimulation signal with period $T_s = 10$ ms for the first 90 ms of an activated CR period. The vertical lines indicate the successive ON- and OFF cycles and the temporal distance between two successive vertical lines correspond to the period T_s of each cycle (every stimulation site is activated exactly once during the ON cycles). A change of color indicates a change of sequence. (B) SVS-4 CR stimulation signal with the same period but here the total time spans up to two completed ON-and OFF cycles ($\sim$ 125 ms) while the color changes as a new sequence is drawn.

For the RVS CR stimulation, sequences are randomly chosen from a set of $N_s!(= 24)$ different possible sequences during each ON-cycle (an example is shown in Fig. 3.1A for CR stimulation period $T_s = 10$ ms for the first 90 ms of an activated CR period). Each newly drawn sequence is indicated by a different color and lasts exactly one ON cycle. On the other hand, for the SVS$-l$ CR stimulation, one first randomly picks a sequence and repeats it l times before switching to another

one, as shown by the example in Fig. 3.1B (again for $T_s = 10$ ms) for $l = 4$. The administered stimulation protocol consists of $m : n = 3 : 2$ CR ON-OFF cycles (see [O.V. Popovych and P. Tass 2012; Lysyansky, O. V. Popovych, and P. A Tass 2011; Zeitler and P. A. Tass 2015]). Depending on the T_s value, more (or less) ON-cycles may be administered within a fixed time interval. In this panel, the total time spans up to two completed ON-and OFF cycles (up to ∼125 ms in this case) and the color changes at each new sequence.

Macroscopic measurements and statistical tools

The synaptic weights, being affected by the STDP and the different intrinsic periods of the neurons, change dynamically in time. One efficient way to measure the strength of the coupling within the neuronal population at time t is given by the following synaptic weight (averaged over the neuron population):

$$C_{av}(t) = N^{-2} \sum_{i,j} sgn(M_{ij}) c_{ij}(t), \tag{3.19}$$

where M_{ij} is defined in Eq. (3.13) and sgn is the sign-function. Furthermore, one may additionally measure the degree of the neuronal synchronization within the ensemble, using the order parameter [Haken 1983; Kuramoto 1984]:

$$R(t) = |N^{-1} \sum_{j} e^{i\varphi_j(t)}| \tag{3.20}$$

where $\varphi_j(t) = \frac{2\pi(t-t_{j,m})}{t_{j,m+1}-t_{j,m}}$ for $t_{j,m} \leq t < t_{j,m+1}$ is a linear approximation of the phase of neuron j between its m^{th} and $(m+1)^{th}$ spikes at spiking times $t_{j,m}$ and $t_{j,m+1}$. $R(t)$ is influenced by the synaptic weights, as the latter are time dependent due to the STDP. The order parameter R measures the extent of phase synchronization in the neuronal ensemble and takes values between 0 (absence of in-phase synchronization) and 1 (perfect in-phase synchronization).

In our numerical calculations, we estimate C_{av} [see Eq. (3.19)] and R_{av}. The latter quantity is averaged over the last $100 \cdot T_s$. Whenever we plot the order parameter versus time, we determine the moving average $< R >$ over a time window of $400 \cdot T_s$, because of the presence of strong fluctuations. For the statistical description and analysis of the non-Gaussian distributed C_{av} and R_{av} data ($n = 11$ samples), we use the median as well as the Inter-Quartile Range (IQR).

3.5 Results

Initial simulation setup

For each initial network of $N = 200$ non-identical-neurons and parameter conditions (or simply "network"), we apply RVS and SVS CR signals (different per network). For each network, the initial conditions for each neuron were randomly drawn from random distributions as given in the Hodgkin-Huxley Spiking Neuron Model subsection. We start the simulation with an equilibration phase, which lasts 2 s. Later on, we evolve the network under the influence of STDP (which will be present until the end of the simulation). We then integrate the network for 60 s with STDP without any external stimulation yet, where a rewiring of the connections takes place, resulting in a strongly synchronized state. Next, we apply CR stimulation for 128 s (resetting the starting time to t = 0 s). During this CR-on period three stimulation ON-cycles (the stimulation is on) alternated with two OFF-cycles (the stimulation is off) as in the example stimulation signals shown in Fig 2. Each ON- and OFF-cycle lasts Ts. After 128 s the CR stimulation ceases permanently and we continue the evolution of the CR-off period for extra 128 s.

In order to probe and chart the CR stimulation intensity and frequency parameter space, we restrict the CR stimulation intensity to values in the interval ($K \in [0.20, ..., 0.50]$). This particular

choice is based on our previous experience and numerical studies (see e.g. [O.V. Popovych and P. Tass 2012; Zeitler and P. A. Tass 2015]) where it was found that weaker intensities were not able to sufficiently desynchronize the neuron ensemble while larger intensities did not significantly improve (or sometimes even worsen) the outcome of RVS and SVS CR stimulation signals. We then set an initial-central value for the CR stimulation period (that defines the initial/starting frequency) which in principle is selected close to the intrinsic firing rate of the strongly synchronized network. In this case, and before applying the CR stimulation, the intrinsic firing rate of the network is ≈71 Hz which corresponds to $T_s \approx 14$ ms. Hence, we begin with the CR stimulation period $T_0 = 16$ ms which gives an initial stimulation frequency $f_0 = 1/T_0$ (in a similar manner just like in [O.V. Popovych and P. Tass 2012; Zeitler and P. A. Tass 2015] and adjusted to a value close to the intrinsic one). Then we define such a period interval $[T_{smin}, T_{smax}]$ in ms (T_s: integer) that allows us to create an "approximately" equidistant grid on the frequency space: $f_{stim} \in [25\% f_0, ..., 175\% f_0]$. This initial T_0-value is also well studied for different types of signal patterns aiming to optimize the CR effect with the use of different type of CR stimulation sequences (see e.g. [Zeitler and P. A. Tass 2015]). Then, we define the ratio (%) of CR sequence frequency per ON-cycle (f_{stim}) over the frequency of the reference stimulation frequency ($f_0 = 62.5$ Hz, $T_0 = 16$ ms) as $r_0 = (f_{stim}/f_0) \cdot 100$ and we end up in studying the intensity and frequency-ratio (K, r_0)– parameter space. In Table 1 in [Manos, Zeitler, and P. A. Tass 2018a], we show the conversion between the stimulation frequency-ratio and period. For comparison reasons, we also give the corresponding ratios r_{int} (%) of CR stimulation frequency per ON-cycle (f_{stim}) over the frequency of the intrinsic firing rate of the network frequency ($f_{int} = 71.4$ Hz, $T_{int} = 14$ ms) without any external stimulation.

Impact of CR Stimulation Duration and Signals on Different Initial Networks

Before presenting the core of our findings, let us first start by discussing how the RVS CR stimulation duration affects the long-lasting anti-kindling of different initial randomly chosen networks. In Fig. 3.2, we show the evolution of the mean synaptic weight C_{av} as a function of time for different total CR-on time durations: $t = 64$ s (Fig. 3.2A), $t = 128$ s (Fig. 3.2B), and $t = 256$ s (Fig. 3.2C). 128 s is the standard CR-on period used throughout the paper. The CR stimulation intensity is $K = 0.20$, and the period $T_s = 10$ ms. A general trend appears in this sequence of panels, i.e. the longer the CR stimulation lasts, less spread of the C_{av} regarding the long-lasting anti-kindling effect is observed after stimulation offset. This is shown in Fig. 3.2D with boxplots. The last box (corresponding to $t = 256$ s of total CR-on period) has no outliers and shows a more "uniform" long-lasting effect (as shown in Fig. 3.2C) for all 11 network initializations, not only during the CR-on period but also afterwards during the CR-off period. However, there is no statistically significant decrease of the median of the C_{av} from $t = 64$ s to $t = 128$ s (right-sided Wilcoxon rank sum test, $p = 0.0209$, 5% significance level). Moreover, the median value of the C_{av} does not change significantly between $t = 128$ s (Fig. 3.2B) and $t = 256$ s (Fig. 3.2C, both-sided Wilcoxon rank sum test, $p = 0.8955$). Hence, the intermediate stimulation duration $t = 128$ s provides fairly good results. Furthermore, for considerably larger stimulation durations the anti-kindling is typically, but not always more pronounced. From a clinical standpoint, it is desirable to achieve reasonably pronounced stimulation effects without excessive stimulation durations. Accordingly, in this computational study we choose $t = 128$ s as total CR-on time, and $t = 256$ s as total CR-on/off time.

For the different simulations, we use different random initial networks and CR signals. For the sake of generality, we do not pick any optimal combination of random initial network and RVS CR

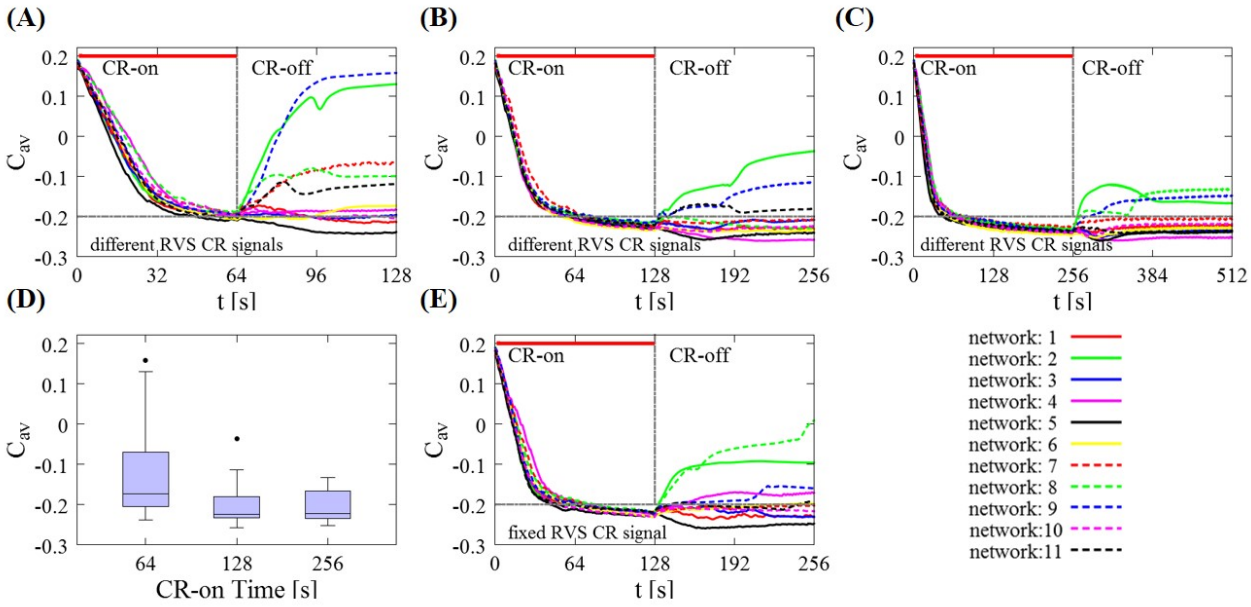

Figure 3.2: Impact of the total CR-on time on the mean synaptic weight C_{av} for different initial random networks and RVS CR. (A) Time evolution of the C_{av} for different total CR-on time durations, $t = 64$ s, (B) $t = 128$ s (this is the standard CR-on period used throughout the paper) and (C) $t = 256$ s. In all these cases, 11 different initial networks were stimulated with different RVS CR stimulation signals during the CR-on period. The thick red horizontal lines indicate the CR-on/off stimulation periods (the end is marked with a vertical gray line) while the horizontal gray dashed lines are visual cues for mutual comparison. (D) Boxplots of the mean synaptic weights presented in (A)-(C), showing the median values (black lines within the boxes). The box frames depict the middle 50%, the upper and lower whiskers the first and last 25% respectively while the outliers (black dots) are set as 1.5 times the length of the box (above/below). There is no statistically significant difference between the data sets at $t = 128$ s and $t = 256$ s ($p = 0.8955$ two-sided Wilcoxon rank sum test). The total CR-on/off time is twice as long as the CR-on period. (E) An identical RVS CR stimulation signal (the one of network 1) was used for all 11 initial networks for $t = 128$ s [comparison with (B)]. In all cases, the CR stimulation intensity is $K = 0.20$ with period $T_s = 10$ ms.

stimulation signal that would induce a favorable or biased behavior. This is to assess whether CR effects are robust with respect to different initial conditions. Fig. 3.2B shows a typical example where 11 different random stimulation signals where applied to 11 different initial networks during the CR-on period, with CR stimulation intensity $K = 0.20$ and stimulation period $T_s = 10$ ms. The CR-on/off period lasts 128 ms respectively. During the CR-on period the mean synaptic weights C_{av} evolve in a similar manner for all networks, with little deviations between the different curves. They reach approximately the same small value at the end of the CR-on period. The latter corresponds to weak excitatory synaptic connectivity and, in most cases in this paper, to globally well-desynchronized states. However, the post-stimulation dynamics of C_{av} may be quite diverse. Some networks retain their weak average connectivity while others, like network 2 and 9 (Fig. 3.2B) relapse back to states with strong synaptic connectivity. Next, we study what happens if we fix the CR stimulation signal for the 11 different initial networks (Fig. 3.2E). The results are similar to

Fig. 3.2B: The outcome at the end of the CR-on period is fairly uniform, while the post-stimulation dynamics of C_{av} is diverse. Replacing one random external stimulation signal by another one may improve the long-term outcome in some cases (e.g. network 8 – green dotted line), but worsen the outcome in others (e.g. network 3 – blue solid line). These plots indicate that both the random initialization of the network and the different stimulation signals during the CR-on period impact on the final outcome at the end of the CR-off period in a complex manner.

Impact of RVS CR Stimulation Intensity and Frequency on Sustained After-Effects

Fig. 3.3 presents a global overview of the long-lasting impact of CR at the end of the CR-off period. Fig. 3.3A shows the median of the mean synaptic weight C_{av}, and Fig. 3.3B the median of the order parameter R_{av}. Figs. 3.3C and 3.3D display the corresponding IQRs, showing that the dispersion around the median of the C_{av} results is very small in large parts of the parameter plane. In contrast, small IQRs are found only for small R_{av}, in regions with strong desynchronization. Figs 3.3A and 3.3B display two main bands in the $(K, r_0)-$parameter space associated with small dispersion: The first band is aligned along the horizontal axis, for weak stimulation intensities (i.e. $K = 0.20$ and $K = 0.25$) and stimulation frequencies greater than 40% of the standard f_0 corresponding to a stimulation period of $T_0 = 16$ ms. The second band runs along the vertical stimulation intensity K axis, and for relatively high frequencies, i.e. for $f_{stim} = 160\% f_0$ ($T_s = 10$ ms) and $f_{stim} = 175\% f_0$ ($T_s = 9$ ms) which correspond to $\approx 155\%$ and $\approx 140\%$ of the firing rate of the synchronized neurons, respectively. For these (bottom-horizontal and right-hand-side-vertical bands) the dispersion around the median values is quite small for both C_{av} and R_{av} (Figs. 3.3C and 3.3D). In addition, the vertical stripe at the reference frequency value f_0 ($100\%, T_s = 16$ ms), studied in [Zeitler and P. A. Tass 2015], but with a $t = 64$ s CR-on period, is also associated with robust long-lasting anti-kindling and desynchronization for all CR stimulation intensity values K. Another region with similar characteristics lies at the center of Figs 3.3A and 3.3B for intermediate stimulation intensity and frequency values.

At a first glance, among those two bands in Figs 3.3A and 3.3B, where dark color dominates suggesting long-lasting anti-kindling after cessation of CR stimulation, the horizontal band seems especially intriguing. Along the lines of our model analysis, the horizontal band corresponds to pronounced desynchronizing outcome at favorably weak CR stimulation intensities within a range of stimulation frequencies. However, we have to keep in mind that the discrete grid is not very dense. Hence, in order to investigate whether this conclusion is justified, we calculated C_{av} and R_{av} for all the integer period T_s values for $K = 0.20$, ranging from $f_{stim} = 175\% f_0$ ($T_s = 10$ ms) to $f_{stim} = 40\% f_0$ ($T_s = 40$ ms). Fig 3.4 shows this fine-grained analysis. The boxplot for C_{av} is shown in Fig 3.4A, and for the R_{av} in Fig 3.4B. Note, in this figure the horizontal axis shows the CR stimulation period instead of the frequency. And it is sorted from larger to smaller values for an easier comparison between the two representations. The red and green dots indicate the reference stimulation period $T_0 = 16$ ms and intrinsic firing rate period $T_{int} = 14$ ms respectively. For $T_s \in [9, \cdots, 24$ ms] we observe robust anti-kindling effects. In contrast, for $T_s \in [25, \cdots, 28$ ms] many networks tend to be in a synchronized state, while for $T_s \in [29, \cdots, 38$ ms] the anti-kindling is found to be robust again, before finally reaching the largest T_s value where the CR stimulation signals are not effective at all. In summary, at weak stimulation intensities favorable stimulation outcomes are achieved within wide ranges of the stimulation frequency. For further analyses of stimulation induced effects observed in particular ranges of the stimulation intensity/frequency parameter plane,

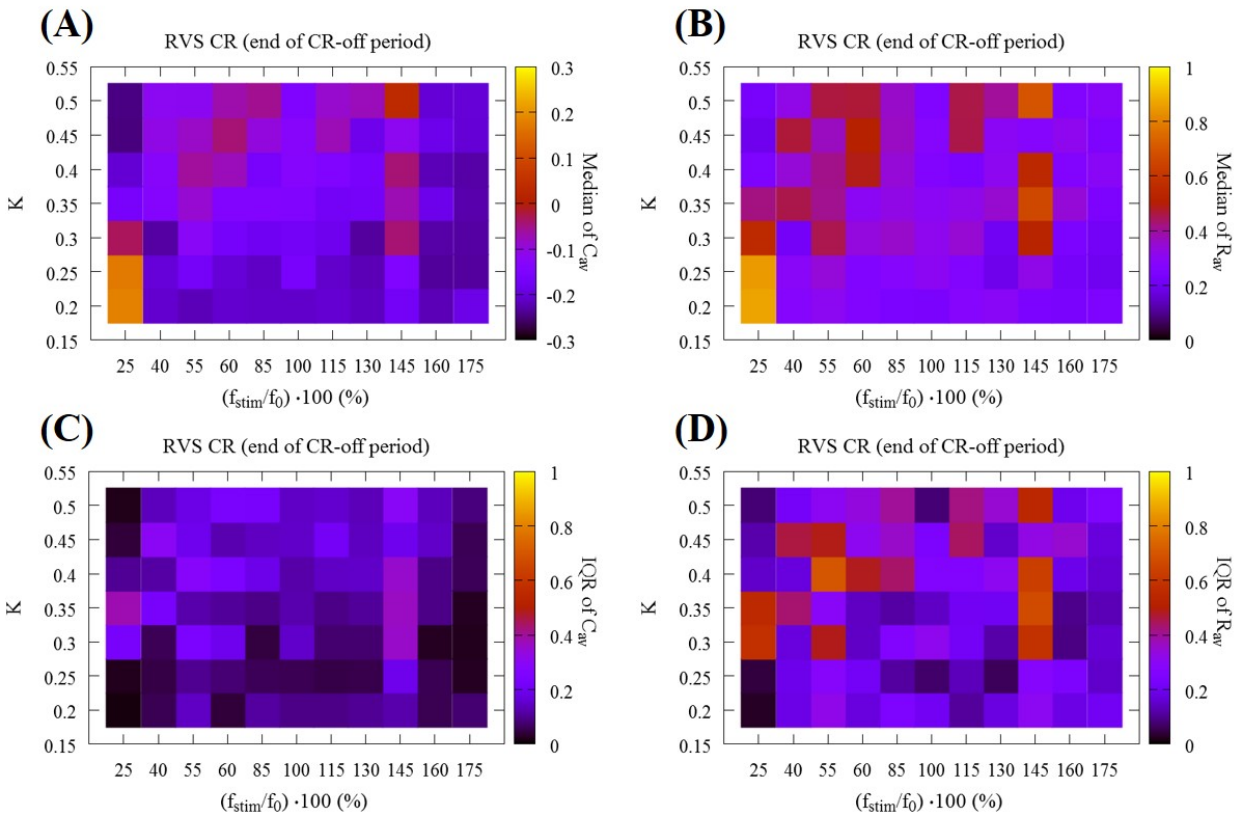

Figure 3.3: Global overview of the mean synaptic weight and synchronization at the end of the CR-off period using RVS CR stimulation. (A) Median of the mean synaptic weight C_{av}, (B) median of the order parameter R_{av} (11 different random initial network configurations and 11 different RVS CR random signals). Long-lasting anti-kindling is achieved in all dark regions as indicated by the corresponding color-bars. Panels (C) and (D) show the dispersion around these median values by plotting their IQR respectively. All IQR values being close to zero indicate that the middle 50% of the distribution are very close to the median value.

we refer to the Supporting Information in [Manos, Zeitler, and P. A. Tass 2018a]. For particular stimulation parameters, similar acute effects, as assessed with macroscopic quantities R_{av} and C_{av}, may lead to qualitatively different results. Neither prominent features of the connectivity matrix nor the dynamical states of the individually stimulated subpopulations at the end of the CR-on period enabled us to predict the long-term outcome. Furthermore, this analysis revealed that CR may be effective without causing side-effects that are time-locked to the individual stimuli.

Simulation description for short-term CR dosage regimen

We investigate two singleshot and two multishot, spaced CR stimulation protocols (Fig. 3.5). The multishot Protocols A and C consist of five single CR shots of 128 s duration, each followed by a pause of 128 s, respectively (Figs. 3.5A,3.5C). The CR singleshot Protocol B consists of a long singleshot

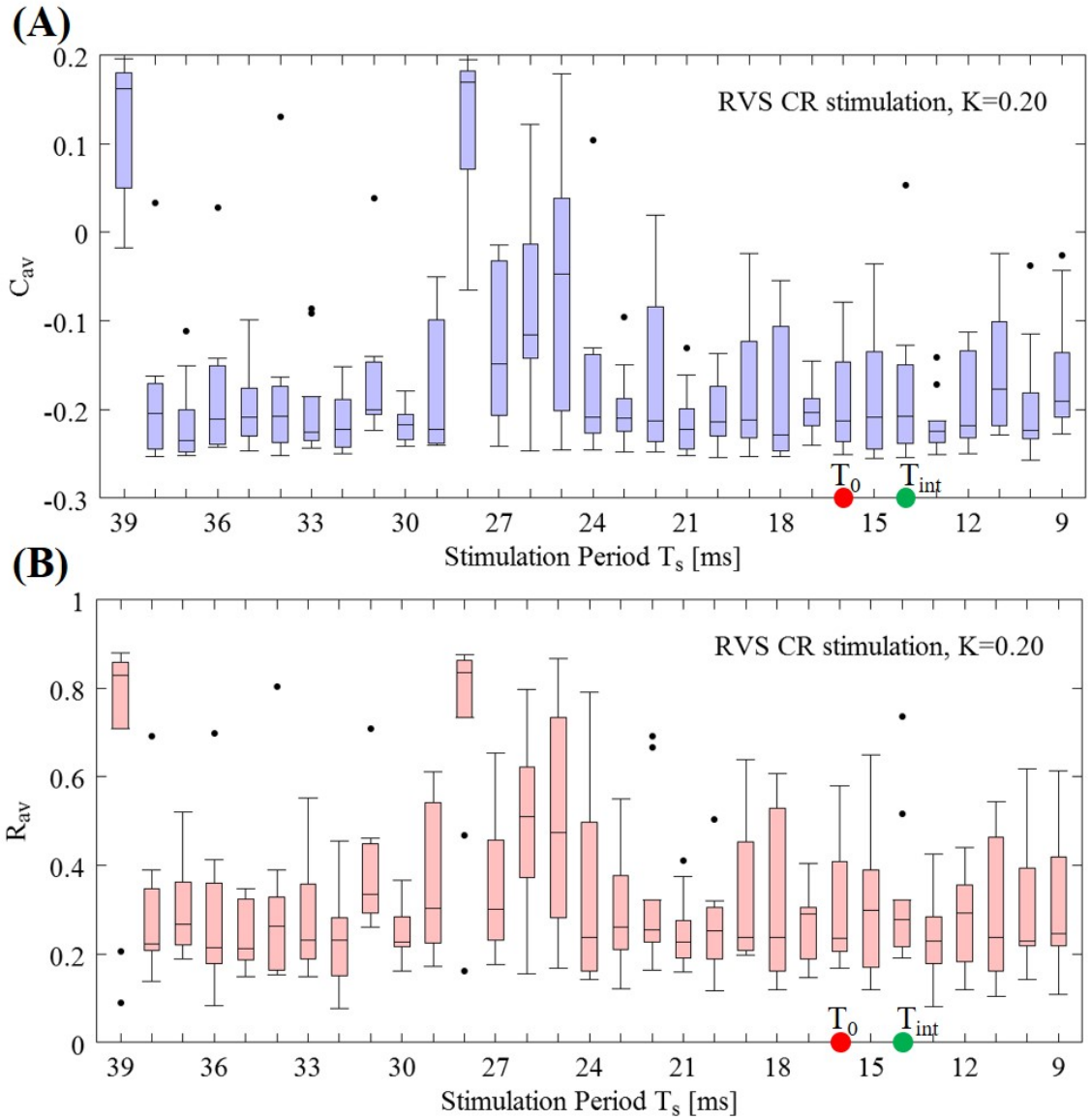

Figure 3.4: Fine-grained T_s-period grid analysis for RVS CR stimulation at intensity $K = 0.20$. (A) Boxplots of C_{av} (mean synaptic weight) and (B) R_{av} (order parameter) for fixed and weak stimulation intensity $K = 0.20$ for a finer sample on the T_s integer value interval at the end of the CR-off period. The red and green dots indicate the reference stimulation period $T_0 = 16$ ms and intrinsic firing rate period $T_{int} = 14$ ms, respectively.

of 5×128 s followed by a pause of 5×128 s (Fig. 3.5B). The CR singleshot Protocol D consists of a long singleshot consisting of five single shots of 128 s duration, strung together without pauses in between, followed by a pause of 5×128 s (Fig. 3.5D). The integral stimulation duration is identical for Protocols A and B. In Protocols A and B all stimulation parameters are kept constant. In contrast, in Protocol C at the end of each pause the amount of synchrony is evaluated in a time window of

100 stimulation periods length (Fig. 3.5) and a three-stage control scheme is put in place: (i) If the amount of synchrony does not fall below a pre-defined threshold, the CR stimulation frequency is mildly varied. (ii) If the desynchronization effect is moderate, the CR stimulation frequency remains unchanged. (iii) If desynchronization is achieved, the stimulation intensity is set to zero for the subsequent shot. Analogously, in Protocol D at the end of each single shot the amount of synchrony is evaluated in a time window of 100 stimulation periods length (Fig. 3.5) and the three-stage control scheme is executed. The difference between Protocol C and D is that the evaluation for the control intervention is performed in a pause subsequent to a single shot (Protocol C) as opposed to during a single shot (Protocol D).

For the stage (i) control, the variation of the CR stimulation frequency is not adapted to frequency characteristics of the neuronal network. Rather a minor variation of the CR stimulation frequency is performed to make a fresh start with the subsequent single CR shot. These minor changes of the CR stimulation frequency do not lead to changes of the neurons' intrinsic firing rates of more than $\pm 3\%$. Due to the stage (iii) control, the demand-controlled shutdown of CR stimulation, the maximum integral stimulation duration of Protocol C and D can reach the level of Protocols A and B, but may well fall below. We use the order parameter to assess the amount of synchronization. We here present a few representative results regarding Protocols A and C only. The complete analysis for all Protocols can be found in [Manos, Zeitler, and P. A. Tass 2018b].

Protocol A: Spaced multishot CR stimulation with fixed stimulation parameters.

For this stimulation protocol all stimulation parameters are kept constant (Fig. 3.5). Accordingly, the CR stimulation period T_s remains constant, too. We study the stimulation outcome of only five symmetrically spaced consecutive single CR shots. To this end, for both RVS CR and SVS CR (not shown here) stimulation we consider two unfavorable parameter pairs of fixed CR stimulation period and intensity, respectively. One example refers to cases where CR stimulation induces acute effects, but no long-lasting desynchronizing effects. The other example concerns the case where CR stimulation causes neither acute nor long-lasting desynchronizing effects in a reliable manner.

RVS CR stimulation: Case I: $(K, T_s) = (0.30, 11)$. At a stimulation duration of 128 s these parameters caused only an acute, but no long-lasting desynchronization in the majority of networks studied (Fig. 3.6), where $T_s = 11$ ms corresponds to $\approx 127\%$ of the intrinsic firing rate (or $\approx$ 91 Hz)]. Case II: $(K, T_s) = (0.20, 28)$. In the majority of networks tested, these parameters did neither lead to acute nor long-lasting desynchronization after administration of a single CR shot (Fig. 3.4) where $T_s = 28$ ms corresponds to $\approx 50\%$ of the intrinsic firing rate (or ≈ 36 Hz)]. For both cases, we investigate the order parameter $< R >$ averaged over a sliding window for 11 different networks (marked with different color/line types, Figs 3.6A,C). Boxplots of the order parameter R_{av} averaged over a window of length $100 \cdot T_s$ at the end of each pause demonstrate the overall stimulation outcome for all tested 11 networks (Figs. 3.6B,D).

Case I: RVS CR stimulation induces a desynchronization during the CR shots (Fig. 3.6A), but no reliable, long-lasting desynchronization in the subsequent pauses (Fig. 3.6B). The spacing protocol with five identical RVS CR shots does not significantly improve the desynchronizing outcome of a single RVS CR shot. In fact, in the boxplots the large dispersion around the median value remains almost unchanged in the course of this protocol (Fig. 3.6B). Case II: Neither during the RVS CR shots nor during the subsequent pauses a sufficient desynchronization is observed (Figs. 3.6C,D). The spacing protocol does not cause an improvement of the stimulation outcome in this case, too

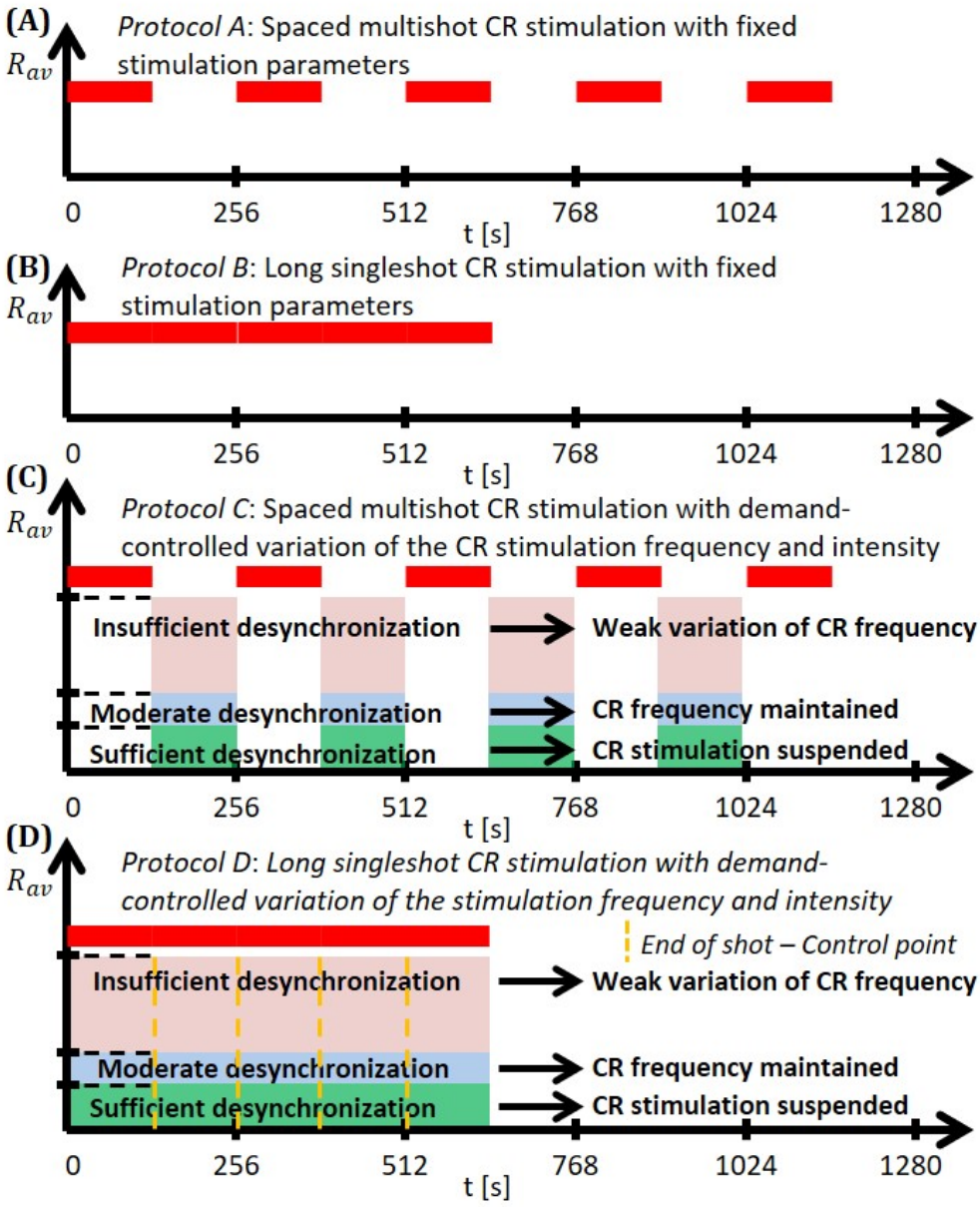

Figure 3.5: Schematic summary of the CR stimulation protocols. (A) Protocol A: Spaced multishot CR stimulation with fixed stimulation parameter. (B) Protocol B: Long singleshot CR stimulation with fixed stimulation parameters. (C) Protocol C: Spaced multishot CR stimulation with demand-controlled variation of the CR stimulation frequency and intensity. (D) Protocol D: Long singleshot CR stimulation with demand-controlled variation of the stimulation frequency and intensity (see text).

(Fig. 3.6D).

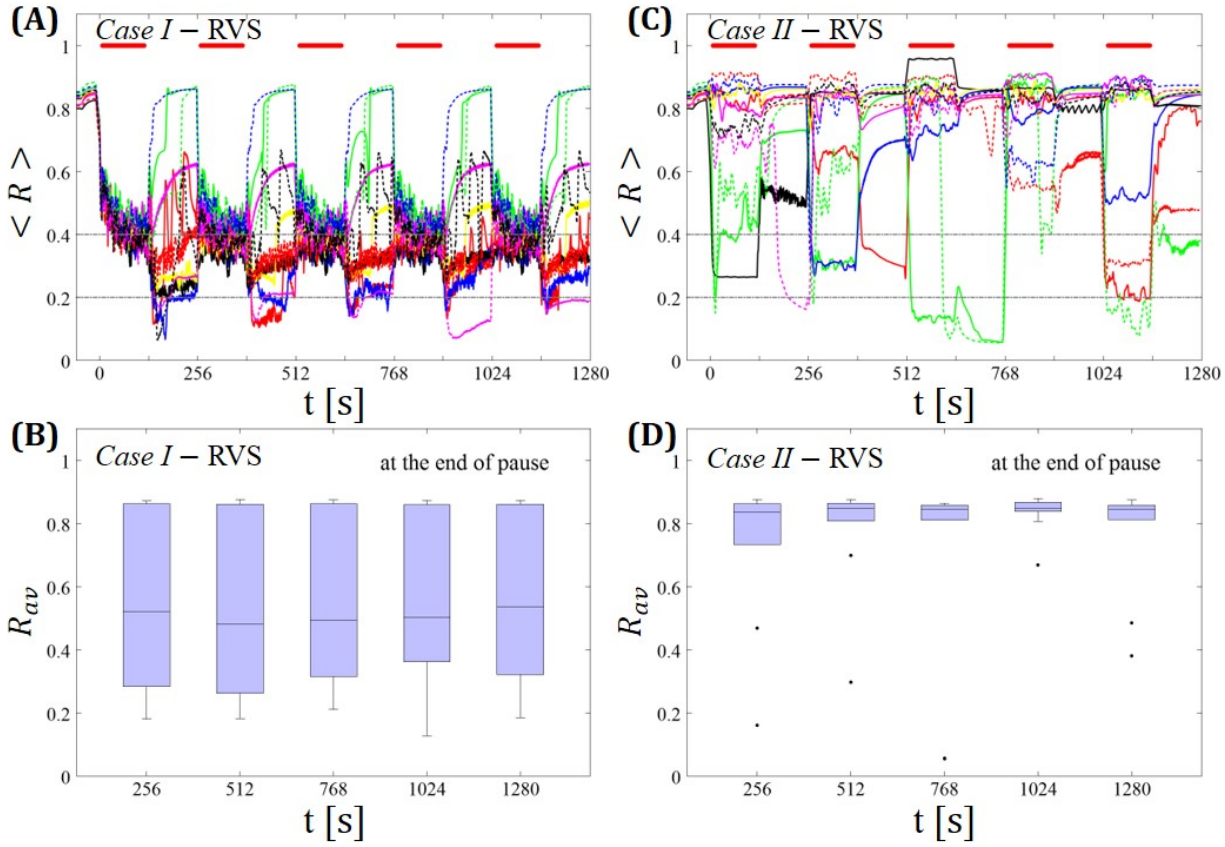

Figure 3.6: Protocol A: Spaced multishot RVS CR stimulation with fixed stimulation period T_s. (A,C) Time evolution of the order parameter $< R >$ averaged over a sliding window during 5 consecutive RVS CR shots with fixed CR stimulation period. Different colors correspond to different networks. Stimulation parameters are unfavorable for anti-kindling in Case I (A,B) and Case II (C,D) (see text). (A,C) The horizontal solid red lines indicate the CR shots, while the horizontal dashed grey lines serve as visual cues. Spacing is symmetrical, i.e. CR shots and consecutive pauses are of the same duration. (B,D) Boxplots for R_{av}, averaged over a window of length $100 \cdot T_s$ at the end of each pause, illustrate the overall outcome for all tested 11 networks. Case I: $(K, T_s) = (0.30, 11)$. Case II: $(K, T_s) = (0.20, 28)$.

Protocol C: Spaced multishot CR stimulation with demand-controlled variation of stimulation period T_s and intensity.

We study the stimulation outcome of only five symmetrically spaced consecutive single CR shots with stimulation period T_s and intensity varied according to a three-stage control scheme. To this end, for both RVS CR and SVS CR (not shown here) stimulation we consider two unfavorable parameter pairs of fixed CR stimulation period and intensity, respectively. One example refers to cases where CR stimulation induces acute effects, but no long-lasting desynchronizing effects. The other example concerns the case where CR stimulation causes neither acute nor long-lasting desynchronizing effects in a reliable manner. We consider a regular and a random type of demand-controlled variation of the

CR stimulation period T_s. Note, in both cases the CR stimulation period is not adapted to frequency characteristics of the network. We consider the time courses of the time-averaged order parameter $< R >$ and R_{av}, the order parameter averaged over a window of length $100 \cdot T_s$ at the end of pause.

Demand-controlled regular variation of the CR stimulation period and demand-controlled variation of the intensity: At the end of each pause we calculate the order parameter R_{av} averaged over a window of length $100 \cdot T_s$. We vary the CR stimulation period and intensity according to the amount of synchrony, based on a three-stage control scheme:

1. Insufficient desynchronization: If $R_{av} > 0.4$, we decrease the CR stimulation period of the subsequent RVS shot by $T_s(j+1) = T_s(j) - 1$ ms, where the index j stands for the $j-$th CR shot. As lower bound we set $T_s = 9$ ms (corresponding to $\approx 156\%$ of the intrinsic firing rate), in order to avoid undesirably high CR stimulation frequencies. In a previous computational study the latter turned out to be unfavorable for desynchronization (see [Manos, Zeitler, and P. A. Tass 2018a]). As soon as T_s reaches its lower bound of 9 ms, it is reset to $T_s(1) + 1$ ms.

2. Moderate desynchronization: If $0.2 \leq R_{av} \leq 0.4$, we preserve the CR stimulation period for the subsequent CR shot: $T_s(j+1) = T_s(j)$, where the index j denotes the $j-$th CR shot. $0.2 \leq R_{av} \leq 0.4$ is considered to be indicative of a desynchronization effect.

3. Sufficient desynchronization: If $R_{av} < 0.2$, the CR stimulation is suspended for the subsequent shot by setting $K = 0$ for the next shot and until $0.2 \leq R_{av}$. $R_{av} < 0.2$ is considered a sufficient desynchronization.

Spaced multishot RVS CR stimulation with demand-controlled regular variation of the stimulation period T_s and demand-controlled variation of the intensity: In both Cases (I and II) this protocol reliably induces a desynchronization for all networks tested (Figs. 3.7A,C). After the second RVS CR shot the median of the time-averaged order parameter R_{av} at the end of the corresponding pauses falls below 0.4, with moderate dispersion (Figs. 3.7B,D). Note, already after the first mild variation of the CR stimulation period T_s the amount of synchrony is strongly reduced. In several networks and pauses, the desynchronization criterion, $R_{av} < 0.2$, is fulfilled, so that during the subsequent CR shots no stimulation is delivered (Figs. 3.7A,C). Accordingly, Protocol C enables to reduce the integral amount of stimulation.

In realistic biological systems intrinsic (model) parameters typically vary over time. These variations may be of complex dynamical nature [see e.g. [Timmer et al. 2000; Yulmetyev et al. 2006]. To obtain some indication as to whether Protocol C is robust against low-amplitude intrinsic variations of the neuronal firing rates, we added a low-amplitude term $I_{var} = A \cdot \sin(2\pi \cdot f \cdot t)$ to the right-hand side of Eq. (3.1). In the stimulation-free case, I_{var} causes variations of the neurons' firing rates in the order of $\pm 3\%$ and no qualitative changes of the network dynamics. For different frequencies f this type of variation does not significantly affect the long-term desynchronization outcome of Protocol C ($f = 0.004$ Hz, 4 Hz and 20 Hz, see Figs. 3.8 and 3.9). By the same token, the neuronal firing rates are not significantly altered by the additional periodic force.

Note, this is not intended to be a comprehensive study of the impact of periodic forcing of arbitrary frequency on the spontaneous or stimulation-induced dynamics of the model network under consideration. Rather, the slow oscillatory forcing is meant to model slow physiological modulatory processes in an illustrative manner. In the extreme case of $f = 0.004$ Hz the slow oscillatory modula-

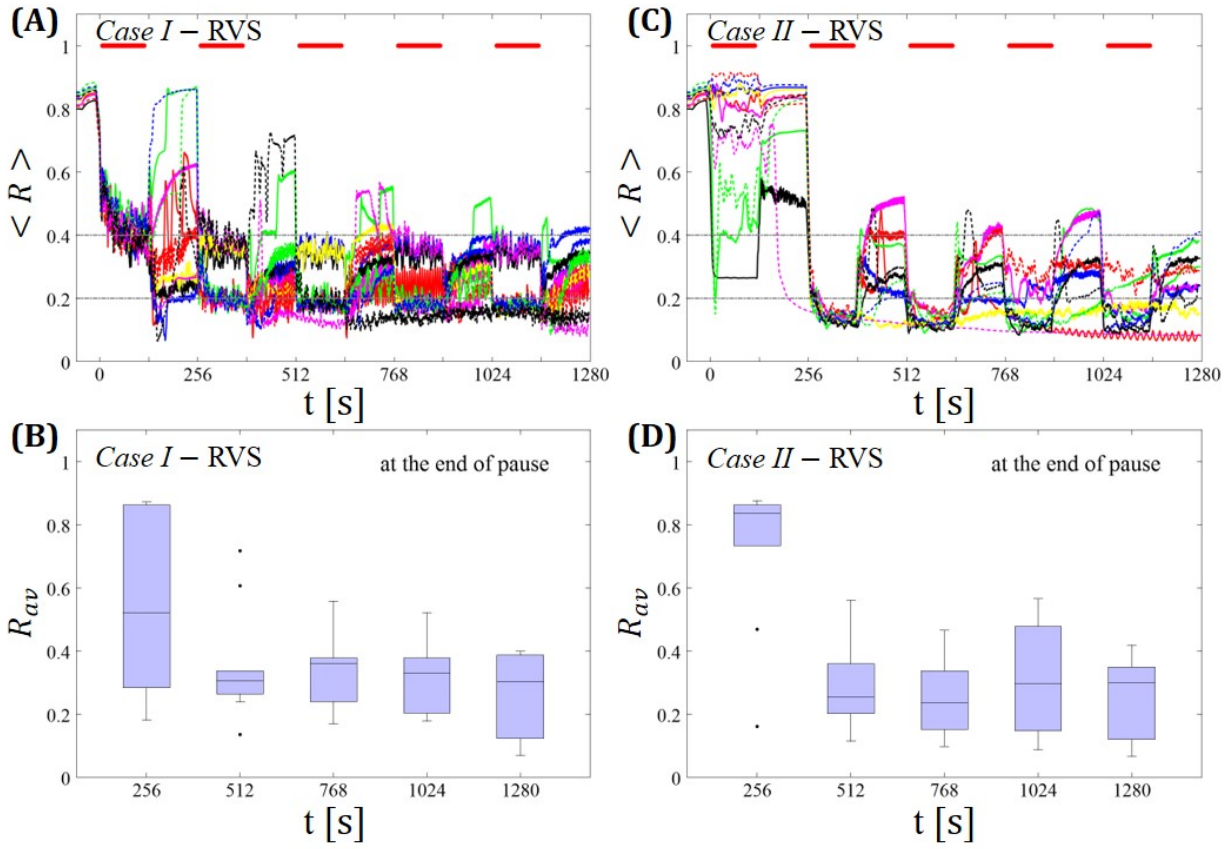

Figure 3.7: Protocol C: Spaced multishot RVS CR stimulation with demand-controlled regular variation of the stimulation period T_s and with demand-controlled variation of the intensity. (A,C) Time evolution of the order parameter $< R >$ averaged over a sliding window during 5 consecutive RVS CR shots. If R_{av}, the order parameter averaged over a window of length $100 \cdot T_s$ at the end of a pause, exceeds 0.4, the CR stimulation period of the subsequent RVS shot is decreased by $T_s \mapsto T_s - 1$ ms (see text). Stimulation parameters are unfavorable for anti-kindling in Case I (A,B) and Case II (C,D) (see text). (A,C) The horizontal solid red lines indicate the CR shots, while the horizontal dashed grey lines serve as visual cues. Spacing is symmetrical, i.e. CR shots and consecutive pauses are of the same duration. (B,D) Boxplots for the time-averaged order parameter R_{av} at the end of each pause, illustrate the overall outcome for all tested 11 networks. Case I: $(K, T_s) = (0.30, 11)$. Case II: $(K, T_s) = (0.20, 28)$.

tion acts on the same time scale as a cycle comprising shot and pause and, hence smoothly emulates the step-wise modulation of the CR stimulation frequency in Protocol C.

3.6 Summary and outlook

By systematically varying the CR stimulation frequency and intensity and comparing the stimulation outcome of the two different CR protocols, RVS and SVS CR stimulation [Manos, Zeitler, and P. A. Tass 2018a], RVS CR proved to be more robust with respect to variations of the stimulation

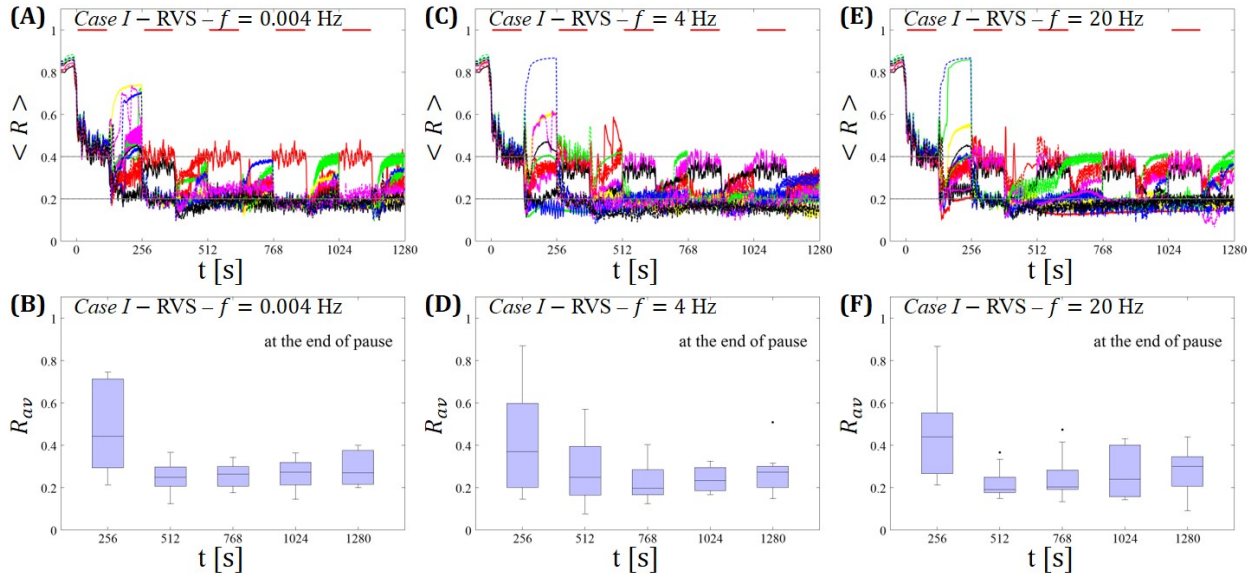

Figure 3.8: Protocol C in the presence of intrinsic variations of the firing rates caused by a modulatory low-amplitude current input $I_{var} = A \cdot \sin(2\pi \cdot f \cdot t)$, with $A = 1$, $f = 0.004$ Hz (A, B), $f = 4$ Hz (C, D) and $f = 20$ Hz (E, F). Spaced multishot RVS CR stimulation with demand-controlled random variation of the stimulation period T_s and with demand-controlled variation of the intensity. The low-amplitude variation I_{var} is active during the entire simulations, respectively. Its low amplitude $A = 1$ ensures that the dynamics of the network is not drastically affected. (A, C, E) Time evolution of the order parameter $< R >$ averaged over a sliding window during 5 consecutive RVS CR shots respectively. If R_{av} at the end of a pause exceeds 0.4, the CR stimulation period of the subsequent SVS shot is decreased by $T_s \mapsto T_s - 1$ ms (see text). (B, D, F) Boxplots for the time-averaged order parameterR_{av} at the end of each pause, illustrate the overall outcome for all tested 11 networks respectively. The horizontal solid red lines indicate the CR shots, while the horizontal dashed grey lines highlight the two control thresholds (see text). Case I stimulation parameters are unfavourable for anti-kindling: $(K, T_s) = (0.30, 11)$.

frequency. However, in accordance with a previous computational study, restricted to a fixed value of the stimulation frequency [Zeitler and P. A. Tass 2015], SVS CR stimulation can induce stronger anti-kindling effects. In our study, we obtained specific parameter ranges related to particularly favorable stimulation outcome. If no closed loop adaptation for the stimulation frequency is available, RVS CR stimulation at weak intensities and with stimulation frequencies in the range of the neuronal firing rates enables us to effectively and robustly achieve an anti-kindling.

To the best of our knowledge, in our study in a plastic network the CR stimulation frequency and intensity were systematically varied for the first time to investigate the impact on acute and long-lasting stimulation outcome. Remarkably, pronounced acute desynchronization (as measured by means of the standard order parameter) does not necessarily lead to long-lasting desynchronization. On the one hand, this finding might inspire future computational and pre-clinical studies aiming at specifically designing stimulation protocols for long-lasting (as opposed to acute) desynchronization. On the other hand, this finding is significant for the development of clinical calibration procedures

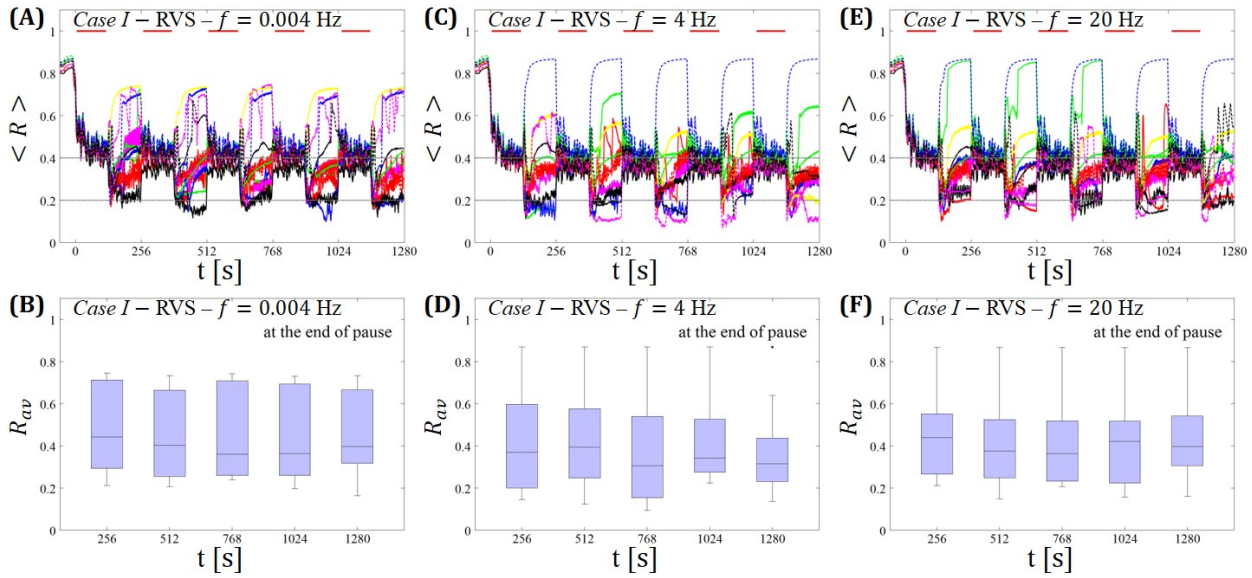

Figure 3.9: Protocol A in the presence of intrinsic variations of the firing rates caused by a modulatory low-amplitude current input $I_{var} = A \cdot \sin(2\pi \cdot f \cdot t)$, with $A = 1$, $f = 0.004$ Hz (A, B), $f = 4$ Hz (C, D) and $f = 20$ Hz (E, F). Spaced multishot RVS CR stimulation with fixed stimulation period T_s. Same series of simulations and analysis as in Fig.3.8. (A, C, E) Time evolution of the order parameter $< R >$ averaged over a sliding window during 5 consecutive RVS CR shots respectively. (B, D, F) Boxplots for the time-averaged order parameter R_{av} at the end of each pause, illustrate the overall outcome for all tested 11 networks respectively. Spacing is symmetrical, i.e. CR shots and consecutive pauses are of the same duration. Case I stimulation parameters are unfavourable for anti-kindling: $(K, T_s) = (0.30, 11)$.

for CR stimulation, see [Adamchic, Toth, Hauptmann, Walger, et al. 2017].

We cannot expect a stimulation technique to be generically effective, irrespective of the neural network model used. Nevertheless, stepwise adding further physiologically and anatomically relevant features to the neural network models employed may help to generate specific predictions and, ultimately, to further improve stimulation protocols and dosage regimes. In that sense, the finding that RVS CR stimulation at weak to moderate intensities and stimulation frequencies adapted to the neurons' intrinsic firing rates causes a desynchronization in neural network models without STDP [Lysyansky, O. V. Popovych, and P. A Tass 2011] and with STDP as shown in this study, is relevant and, in fact, in accordance with pre-clinical findings [J. Wang et al. 2016; P. A. Tass, Qin, et al. 2012a]. Furthermore, the fact that SVS CR stimulation might even be more effective, but requires more careful parameter adaptation may guide future development of calibration techniques as put forward in [Manos, Zeitler, and P. A. Tass 2018b].

We demonstrated that over a wide range of stimulation parameters favorable acute effects do not automatically lead to favorable long-lasting, sustained after-effects. This is in agreement with a computational study in the same model, but performed in only a restricted parameter range [Zeitler and P. A. Tass 2015], as well as with an electroencephalograms (EEG) experiment performed in tinnitus patients [Adamchic, Toth, Hauptmann, Walger, et al. 2017]. To characterize stimulation induced ef-

fects, we here used the average synaptic weight and the average amount of neuronal synchrony. These macroscopic quantities enabled us to effectively investigate the impact of variations of stimulation parameters on the stimulation outcome.

In neural networks without STDP tested so far, CR stimulation works at higher intensities as well, see e.g. [Lysyansky, O. V. Popovych, and P. A Tass 2011]. In that case, pronounced cluster states are induced, but coherent synchrony is reliably suppressed. This is not the case in the neural network model with STDP studied here. For both RVS CR and SVS CR, for several parameters tested the long-term outcome deteriorates with increasing stimulation intensity. Accordingly, based on our results, in pre-clinical and clinical applications stimulation at higher intensities should be avoided. Another important aspect refers to the more pronounced periodicity of SVS CR pattern. In previous papers (lacking a wider scan of the parameter space), SVS CR stimulation appeared to be superior to RVS CR stimulation [Zeitler and P. A. Tass 2015; Zeitler and P. A. Tass 2016]. Here, we showed that SVS CR stimulation decisively depends on the appropriate choice of the stimulation frequency. This sensitivity may significantly reduce the performance in the presence of biologically realistic variations of the neuronal firing rates and might, hence, be the very reason, why the outcome of SVS CR stimulation is significantly better for smaller numbers of sequence repetitions.

In contradiction to the results obtained in networks without STDP [P. A. Tass 2003b; P. A. Tass 2003a; Lysyansky, O. V. Popovych, and P. A Tass 2011], CR stimulation may cause a full-blown anti-kindling without any phase resets of the subpopulations time locked to the corresponding stimuli (see S4 Fig. in [Manos, Zeitler, and P. A. Tass 2018a]). This is relevant for two reasons: (i) Since effective CR stimulation does not require phase resets time-locked to the individual stimuli, further computational studies should elucidate whether it makes sense to calibrate CR stimuli for pre-clinical and clinical applications by selecting stimulus parameters that favorably achieve phase resets. Corresponding results might be relevant for the design of calibration procedures and, in addition, challenge existing patents that are based on selecting parameters that optimally achieve phase resets of the stimuli delivered to the individual sub-populations. (ii) By the same token, our results do not only challenge current hypotheses on the mechanism of CR stimulation, but also fundamental patents in the field of invasive as well as non-invasive CR stimulation. Accordingly, future computational studies should focus on the mechanism of action of CR stimulation in networks with STDP in order to actually understand and possibly improve anti-kindling protocols.

Our goal was to accomplish an anti-kindling in a way as robust as possible, complying with clinically motivated constraints. For instance, striving for anti-kindling induced at minimal stimulation intensities led to the computational development of spaced CR stimulation [O. V. Popovych, Xenakis, and P. A. Tass 2015] and two-stage CR stimulation with weak onset intensity [Zeitler and P. A. Tass 2016]. The motivation behind these developments was to avoid side effects by substantially reducing stimulation intensities. In this context, it might turn out to be beneficial that RVS CR stimulation causes sustained after-effects over a wide range of stimulation frequencies even at weak intensity (Fig. 3.3). Accordingly, RVS CR stimulation might provide an appropriate stimulation protocol, in particular, if applied in an open-loop manner, without the ability to calibrate the stimulation parameters, especially the stimulation frequency by adapting it to the dominant peaks in the frequency spectrum of electrophysiological signals such as local field potentials or EEG signals.

By comparing spaced CR stimulation with fixed stimulation parameters (Protocol A) and massed, continuous CR stimulation with equal integral duration (Protocol B) with a flexible spaced CR stimulation with demand-controlled variation of CR stimulation frequency and intensity (Protocol C), and with a flexible non-spaced CR stimulation with demand-controlled variation of CR stimulation

frequency and intensity (Protocol D), we demonstrated [Manos, Zeitler, and P. A. Tass 2018b] that Protocol C enables to significantly improve the long-term desynchronization outcome of both RVS and SVS CR stimulation, even at comparatively short integral stimulation duration. Remarkably, spacing alone (Protocol A) is not sufficient to provide an efficient short-term dosage regimen. In fact, in particular cases fivefold longer stimulation duration might even be more efficient than five consecutive single CR shots with identical integral stimulation duration, at least for RVS CR stimulation [Manos, Zeitler, and P. A. Tass 2018b]. The low performance of pure spacing (Protocol A) might be due to the low number of single CR shots, here five, as opposed to slightly larger numbers of CR shots, say eight, tested for the case of subcritical CR stimulation before [O. V. Popovych, Xenakis, and P. A. Tass 2015]. However, more important might be the approx. fifty-fold longer stimulation and pause duration used for the spaced subcritical CR stimulation protocol. The long spaced subcritical CR stimulation protocol might be beneficial for invasive application, such as DBS, and help reduce side-effects by substantially reducing stimulation current intake of the issue.

We computationally showed that a spacing with rigid five-shot timing structure, but flexible, demand-controlled variation of stimulation frequency and intensity (Protocol C) provides a short-term dosage regimen that significantly improves the long-term desynchronization outcome of RVS and SVS CR stimulation. At the end of each pause between CR shots, the stimulus after-effect is assessed. If the desynchronization is considered to be insufficient, a mild variation of the CR stimulation frequency is performed to possibly provide a better fit between network and CR stimulation frequency, without actually adapting the stimulation frequency to frequency characteristics of the network stimulated. If desynchronization is considered to be moderate, the subsequent CR shot is delivered with parameters unchanged. If desynchronization is sufficient, CR stimulation is suspended during the subsequent shot. Intriguingly, in the vast majority of parameters and networks tested, this short-term dosage regimen induces a robust and reliable long-lasting desynchronization. This protocol might be a candidate especially for non-invasive, e.g. acoustic [P. Tass, Adamchic, et al. 2009] or vibrotactile [Syrkin-Nikolau et al. 2018; P. A. Tass 2017], applications of CR stimulation to increase desynchronization efficacy, while keeping the stimulation duration at moderate levels.

Demand-controlled variation of CR stimulation frequency and intensity (Protocol D) alone (i.e. without inserting pauses) is not sufficient to significantly improve the outcome of RVS and SVS stimulation [Manos, Zeitler, and P. A. Tass 2018b]. Hence, introducing pauses significantly improves the effect of the demand-controlled variation of CR stimulation frequency and intensity. In principle, stimulation parameters other than the CR stimulation frequency might be varied depending on the stimulation outcome. However, in this study we have chosen to vary the CR stimulation frequency, since the latter turned out to be a sensitive parameter, especially for SVS CR stimulation (see [Manos, Zeitler, and P. A. Tass 2018a]). In fact, the short-term dosage regimen with demand-controlled variation of stimulation parameters (Protocol C) might help to turn SVS CR stimulation in a method that causes a particularly strong anti-kindling in a robust and reliable manner.

Protocol C does not require a direct adaption of the CR stimulation frequency to measured quantities reflecting frequency characteristics of the network. We have chosen this design, since it might be an advantage not to rely on specific biomarker-type of information. For instance, in the case of PD a number of relevant studies were devoted to closed-loop DBS (see e.g. [Graupe et al. 2010; Rosin et al. 2011; Little et al. 2013; Rosa et al. 2015]). A relevant issue in this context is the availability of a biomarker adequately reflecting the individual patient's extent of symptoms [Beudel and Brown 2016; Kühn and Volkmann 2017]. In fact, it is not clear whether low or high frequency beta band oscillations might be more appropriate as biomarker-type of feedback signal [Beudel and

Brown 2016]. For several reasons, beta band oscillations might possibly not be an optimal feedback signal (see e.g. [Kühn and Volkmann 2017]). Enhanced beta band oscillations are not consistently found in all PD patients [Beudel and Brown 2016; Kühn and Volkmann 2017]. The clinical score of PD patients might more appropriately be reflected by the power ratio of two distinct bands of high frequency oscillations around 250 Hz and 350 Hz [Özkurt et al. 2011]. Appropriate biomarkers might depend on the patient phenotype [Quinn et al. 2015]: In tremor dominant (compared to akinetic rigid) PD patients resting state beta power may decrease during tremor epochs [Bronte-Stewart et al. 2009; Quinn et al. 2015]. By a similar token, theta and beta oscillations interact with high-frequency oscillations under physiological [Yanagisawa et al. 2012] as well as pathological [Yang et al. 2014] conditions. Also, quantities assessing the interaction of brain oscillation, e.g. phase amplitude coupling might be used as biomarker to represent the amount of symptoms [Beudel and Brown 2016]. Also, activity in the beta band might be relevant for compensatory purposes, as recently shown in a parkinsonian monkey study with sensorimotor rhythm neurofeedback [Philippens et al. 2017].

It might be another potential advantage for clinical applications that the three-stage control of the proposed short-term dosage regimen (Protocol C) could possibly be approximated by scores reflecting the patient's state or the amount symptoms. A simple three-stage rating of the patient's state (bad, medium, and good) might replace the feedback signal-based stages (i), (ii), and (iii). Assessments of the patient's state might be performed in a pause after a CR shot. Depending on the rating, the CR stimulation frequency or intensity of the subsequent CR shot may be varied. In particular, for non-invasive application of CR stimulation a non-invasive assessment of the stimulation effect might straightforwardly be realized.

Intrinsic variations of sufficient size might naturally mimic variations of the relationship between CR stimulation frequency and intrinsic neuronal firing rates as introduced on purpose in Protocol C. Accordingly, already the purely spaced stimulation without demand-controlled variability (Protocol A) might display some variability of the relationships between intrinsic firing rates and CR stimulation frequency simply due to the intrinsic variability. However, at least with the frequencies 0.004 Hz, 4 Hz and 20 Hz in the low-amplitude term $I_{var} = A \cdot \sin(2\pi \cdot f \cdot t)$ added to the right-hand side of Eq. (3.1), we were not able to observe any substantial improvement of the desynchronizing outcome of Protocol A (Fig. 3.9 from Supplementary Fig. 2 in [Manos, Zeitler, and P. A. Tass 2018b]). However, more physiological patterns of firing rate modulations might have a more significant impact on the stimulation outcome of Protocol A. In future studies typical variations of the signals relevant to a particular pre-clinical or clinical application might be taken into account to further improve desynchronizing short-term dosage regimen. The additional periodic forcing considered here was meant to illustrate the stability of the suggested control approach. However, future studies could also provide a detailed analysis of the interplay of one or more periodic inputs and noise, thereby focusing on stochastic resonance and related phenomena (e.g. [A. S. Pikovsky and J. Kurths 1997]). The number of stimulation sites and CR stimulation spatial decay was based on [Lysyansky, O. V. Popovych, and P. A Tass 2011]. In accordance to that study, adding more stimulation sites does neither lead to qualitatively different results nor does it improve the stimulation outcome.

The short-term dosage regimen proposed here provides a closed-loop CR stimulation concept that enables to significantly increase the robustness and reliability of the stimulation outcome. Our results motivate to further improve the CR approach by closed loop or feedback-based dosage regimen. Compared to the computationally developed initial concept of demand-controlled CR-induced desynchronization of networks with fixed coupling constants [P. A. Tass 2003b; P. A. Tass 2003a], the focus will now be on a feedback-adjusted modulation of synaptic patterns to induce long-lasting

therapeutic effects. Currently, clinical proof of concept (*phase IIa*) is available for deep brain CR stimulation for the therapy of Parkinson's disease [Adamchic, Hauptmann, et al. 2014] and acoustic CR stimulation for the treatment of chronic subjective tinnitus [P. Tass, Adamchic, et al. 2009]. In addition, promising first in human (*phase I*) data are available for vibrotactile CR stimulation for the treatment of Parkinson's disease showing pronounced and highly significant sustained therapeutic effects [Syrkin-Nikolau et al. 2018]. For the clinical development of these treatments it is mandatory to perform dose-finding studies (*phase IIb*) to reveal optimal stimulation parameters and dosage regimens, for comparison see [Friedman, Furberg, and Demets 2010]. The latter are required to get properly prepared for large efficacy (*phase III*) trials [Friedman, Furberg, and Demets 2010]. Since CR stimulation modulates complex neuronal dynamics, dose-finding studies are sophisticated, since stimulation parameters as well as dosage patterns have to be chosen appropriately. Selecting appropriate stimulation parameters and dosage regimens by trial and error may neither be effective nor affordable, since it would require a huge number of patients. In contrast, this work illustrates the important role of computational medicine in generating hypotheses for dose-finding studies. Specifically, we show that spacing (i.e. adding pauses in between stimulation epochs) as well as moderate and unspecific parameter variations adapted in the course of the therapy are not sufficient to overcome limitations of CR stimulation. Intriguingly, the combination of both, spacing plus adaptive moderate parameter variation increases the robustness of the stimulation outcome in a significant manner. This computational prediction can immediately be tested in dose-finding studies and, hence, help to optimize the CR therapy, shorten the development time and reduce related costs.

Perspectives

Besides the spike timing-dependent plasticity (modulating relative synaptic strength connectivity between neurons on a time scale of seconds to minutes) there is also the structural plasticity (deletion pre-existing or generation new synapses in order to homeostatically adapt the firing rate of the neurons on a time scale of days to months), see e.g. [Diaz-Pier et al. 2016]. The latter one is not extensively studied while combining both types of plasticity is a rather complicated task as one should design models that can operate at different time scales. An interesting future task could be to investigate the role of structural plasticity in explaining long-term deep brain stimulation effects. In this framework, we aim to set up a rather detailed network and incorporate physiologically relevant mechanisms, such as dynamical evolution of synaptic connections between neurons, in order to optimize the stimulation protocols [Manos T., Diaz-Pier S. and Tass P.A. "Long-term desynchronization by coordinated reset stimulation in a neural network model with synaptic and structural plasticity", (in revision) 2020]. This type of investigation is not able to take place at a clinical setting and hence one needs to employ theoretical and computational studies in order to ultimately improve the quality of life of patients and minimize side effects of the deep brain stimulation after surgery.

Nonlinear dynamical systems have been recently employed in the study of the human brain also at larger spatio-temporal scales. The human brain is a complex neural network able to self-organise into different emergent states crucial for its healthy and pathological functioning. At a meso- and macro-scale level, a brain connectivity network consists of nodes (grey matter regions) and edges. Edges can represent white matter tracts in structural networks connectome, the so-called structural connectivity, or correlations between for example, two blood-oxygen-level-dependent (BOLD) or EEG time series in functional networks, the so-called functional connectivity (FC), see e.g. [Sporns, Tononi, and Kötter 2005]. Interdisciplinary approaches using concepts from nonlinear dynamics, physics, bi-

ology and medicine, have allowed us to understand in more depth how the human brain functions. A dynamical-model approach, can provide links between attractors, bifurcations, synchronisation patterns and empirical neuroimaging data, such as EEG, BOLD functional magnetic resonance imaging (fMRI), etc. By choosing adequate model parameters (e.g. via a parameter sweep exploration), it is feasible to build customised virtual brain activity for individual subjects. These parameters can serve as dynamical biomarkers and predictors of different brain states (healthy vs diseased) and behavioural modes [O. V. Popovych, Manos, et al. 2019]. Following such concepts, the virtual epileptic patient has been recently proposed [Jirsa et al. 2017], where such medical-treatment approaches using personalised mathematical models for epileptic patients has been illustrated. By better understanding the pathological activity as opposed to health, one aims to optimize appropriately the treatment. Furthermore, such brain networks nodes and edges are not uniquely defined. Typically, the voxel parcellation is based on certain criteria from the analysis of the neuroimaging data. These criteria may be based for example on structural neural information of the areas or their functionality or co-activation during a task, see e.g. [Stanley et al. 2013; Thirion et al. 2014; Eickhoff, Yeo, and Genon 2018]. Ultimately, one is able to reduce the dimensionality of the brain data by merging hundred thousands of voxels from the high-resolution neuroimaging data into a few brain regions. So far, there is no unified brain parcellation. One important benefit for such a result would be the interpretability and comparability of the results for different subjects and studies.

There are many ways to design such a parcellation map (brain atlas). Recently, we investigate two paradigmatically distinct cases [Popovych O. V., Kyesam J., Manos T., Diaz-Pier S., Hoffstaedter F., Schreiber J., Yeo, B. T. T. and Eickhoff S. B., "Impact of brain parcellation and empirical data on modeling of the resting-state brain dynamics", (submitted) 2020]: (i) a parcellation of the cortex regions according to its folding properties, e.g., into gyral-based parcels encircled by tracing from the depth of one sulcus to another [Desikan et al. 2006] and (ii) a parcellation approach based on the brain function, where the patterns of the resting-state FC can be used to group the voxels (or vertices) into parcels of similar connectivity [Schaefer et al. 2018]. Thus, we can model and investigate the effects of brain parcellation in great detail with a dynamical system, e.g. coupled phase oscillators suggested for modeling cortical oscillations and resting-state BOLD dynamics [Breakspear, Heitmann, and Daffertshofer 2010; Cabral et al. 2011; Ponce-Alvarez et al. 2015; Fukushima and Sporns 2018]. In this approach, each node is modeled by a phase oscillator (e.g. [Kuramoto 1984]), the total number of brain node is assigned by the given brain atlas, the relative connectivity strength and delay signal propagation can be estimated by the empirical neuroimaging data (for each subject) as well as estimates about the nodes' frequency. All the above can be used as inputs into the dynamical system and allow for a relatively small free set of parameters (physiologically relevant, such as global coupling, delay scaling etc.) to be explored and tuned in a way that can describe and ultimately explain adequately the dynamics of certain resting-states or brain activity during tasks as well as distinguish between healthy and pathologically states.

Bibliography

Adamchic, I., C. Hauptmann, U.B. Barnikol, N. Pawelczyk, O.V. Popovych, Thomas T. Barnikol, A. Silchenko, J. Volkmann, G. Deuschl, W.G. Meissner, M. Maarouf, V. Sturm, H.-J. Freund, and P.A. Tass (2014). "Coordinated reset neuromodulation for Parkinson's disease: proof-of-concept study". In: *Movement disorders : official journal of the Movement Disorder Society* 29.13, pp. 1679–1684.

Adamchic, I., B. Langguth, C. Hauptmann, and P. A. Tass (2012). "Psychometric Evaluation of Visual Analog Scale for the Assessment of Chronic Tinnitus". In: *Am. J. Audiol.* 21.2, pp. 215–225.

— (2014). "Abnormal cross-frequency coupling in the tinnitus network". In: *Frontiers in Neuroscience* 8, p. 284.

Adamchic, I., T. Toth, C. Hauptmann, and P. A. Tass (2014). "Reversing pathologically increased EEG power by acoustic coordinated reset neuromodulation". In: *Hum. Brain Mapp.* 35.5, pp. 2099–2118.

Adamchic, I., T. Toth, C. Hauptmann, M. Walger, B. Langguth, I. Klingmann, and P. A. Tass (2017). "Acute effects and after-effects of acoustic coordinated reset neuromodulation in patients with chronic subjective tinnitus". In: *NeuroImage: Clinical* 15, pp. 541–558.

Angelini, L., M. De Tommaso, M. Guido, K. Hu, P. Ch. Ivanov, D. Marinazzo, G. Nardulli, L. Nitti, M. Pellicoro, C. Pierro, and S. Stramaglia (2004). "Steady-State Visual Evoked Potentials and Phase Synchronization in Migraine Patients". In: *Phys. Rev. Lett.* 93 (3), p. 038103.

Athanassoula, E. (2003). "What determines the strength and the slowdown rate of bars?" In: *Mon. Not. R. Astron. Soc.* 341, pp. 1179–1198.

Athanassoula, E., R. E. G. Machado, and S. A. Rodionov (2013a). "Bar formation and evolution in disc galaxies with gas and a triaxial halo: morphology, bar strength and halo properties". In: *Mon. Not. R. Astron. Soc.* 429, pp. 1949–1969.

— (2013b). "Bar formation and evolution in disc galaxies with gas and a triaxial halo: morphology, bar strength and halo properties". In: *Mon. Not. R. Astron. Soc.* 429, pp. 1949–1969.

Athanassoula, E. and A. Misiriotis (2002). "Morphology, photometry and kinematics of N -body bars - I. Three models with different halo central concentrations". In: *Mon. Not. R. Astron. Soc.* 330, pp. 35–52.

Athanassoula, E., M. Romero-Gómez, A. Bosma, and J. J. Masdemont (2009). "Rings and spirals in barred galaxies - II. Ring and spiral morphology". In: *Mon. Not. R. Astron. Soc.* 400, pp. 1706–1720.

— (2010). "Rings and spirals in barred galaxies - III. Further comparisons and links to observations". In: *Mon. Not. R. Astron. Soc.* 407, pp. 1433–1448.

Athanassoula, E., M. Romero-Gómez, and J. J. Masdemont (2009). "Rings and spirals in barred galaxies - I. Building blocks". In: *Mon. Not. R. Astron. Soc.* 394, pp. 67–81.

Bartsch, R. P., A. Y. Schumann, J. W. Kantelhardt, T. Penzel, and P. C. Ivanov (2012). "Phase transitions in physiologic coupling". In: 109.26, pp. 10181–10186.

Batistić, B., T. Manos, and M. Robnik (2013). "The intermediate level statistics in dynamically localized chaotic eigenstates". In: *Europhys. Lett.* 102.5, p. 50008.

Batistić, B. and M. Robnik (2010). "Semiempirical theory of level spacing distribution beyond the Berry–Robnik regime: modeling the localization and the tunneling effects". In: *J. Phys. A: Math. Theor.* 43.21, p. 215101.

— (2013a). "Dynamical localization of chaotic eigenstates in the mixed-type systems: spectral statistics in a billiard system after separation of regular and chaotic eigenstates". In: *J. Phys. A: Math. Theor.* 46.31, p. 315102.

— (2013b). "Quantum localization of chaotic eigenstates and the level spacing distribution". In: *Phys. Rev. E* 88 (5), p. 052913.

Benabid, A. L., P. Pollak, C. Gervason, D. Hoffmann, D. M. Gao, M. Hommel, J. E. Perret, and J. de Rougemont (1991). "Long-term suppression of tremor by chronic stimulation of the ventral intermediate thalamic nucleus". In: *The Lancet* 337, pp. 403–406.

Benettin, G., L. Galgani, A. Giorgilli, and J.-M. Strelcyn (1980). "Lyapunov characteristic exponents for smooth dynamical systems and for Hamiltonian systems - A method for computing all of them. I - Theory. II - Numerical application". In: *Meccanica* 15, pp. 9–30.

Benettin, G., L. Galgani, and J.-M. Strelcyn (1976). "Kolmogorov entropy and numerical experiments". In: *Phys. Rev. A* 14, pp. 2338–2345.

Berry, M. V. (1977). "Regular and irregular semiclassical wavefunctions". In: *J. Phys. A: Math. Gen.* 10.12, pp. 2083–2091.

— (1985). "Semiclassical theory of spectral rigidity". In: *Proceedings of the Royal Society of London. A. Mathematical and Physical Sciences* 400.1819, pp. 229–251.

Berry, M. V. and M. Robnik (1984). "Semiclassical level spacings when regular and chaotic orbits coexist". In: *J. Phys. A: Math. Gen.* 17.12, pp. 2413–2421.

Beudel, M. and P. Brown (2016). "Adaptive deep brain stimulation in Parkinson's disease". In: *Parkinsonism Relat. D.* 22, S123–S126.

Bi, Guo-qiang and Mu-ming Poo (1998). "Synaptic modifications in cultured hippocampal neurons: Dependence on spike timing, synaptic strength, and postsynaptic cell type". In: *J. Neurosci.* 18.24, pp. 10464–10472.

Binney, J. and S. Tremaine (2008). *Galactic Dynamics: Second Edition*. Princeton University Press.

Bjørk, M. H. and T. Sand (2008). "Quantitative EEG Power and Asymmetry Increase 36 h Before a Migraine Attack". In: *Cephalalgia* 28.9, pp. 960–968.

Bliss, T.V.P. and T. Lømo (1973). "Long-lasting potentiation of synaptic transmission in the dentate area of the anaesthetized rabbit following stimulation of the perforant path". In: *J. Physiol.* 232.2, pp. 331–356.

Bohigas, O., M. J. Giannoni, and C. Schmit (1984). "Characterization of Chaotic Quantum Spectra and Universality of Level Fluctuation Laws". In: *Phys. Rev. Lett.* 52 (1), pp. 1–4.

Bountis, T., T. Manos, and C. Antonopoulos (2012). "Complex statistics in Hamiltonian barred galaxy models". In: *Celest. Mech. Dyn. Astron.* 113, pp. 63–80.

Bountis, T., T. Manos, and H. Christodoulidi (2009). "Application of the GALI method to localization dynamics in nonlinear systems". In: *J. Comput. Appl. Math.* 227, pp. 17–26.

Bour, L. J., M. A. J. Lourens, R. Verhagen, R. M. A. de Bie, P. van den Munckhof, P. R. Schuurman, and M. F. Conta (2015). "Directional Recording of Subthalamic Spectral Power Densities in Parkinson's Disease and the Effect of Steering Deep Brain Stimulation". In: *Brain Stimul.* 9.4, pp. 730–741.

Breakspear, M., S. Heitmann, and A. Daffertshofer (2010). "Generative models of cortical oscillations: neurobiological implications of the Kuramoto model". In: *Front. Hum. Neurosci.* 4, p. 190.

Brody, T. A., J. Flores, J. B. French, P. A. Mello, A. Pandey, and S. S. M. Wong (1981). "Random-matrix physics: spectrum and strength fluctuations". In: *Rev. Mod. Phys.* 53 (3), pp. 385–479.

Bronte-Stewart, H., C. Barberini, M. M. Koop, B. C. Hill, J. M. Henderson, and B. Wingeier (2009). "The STN beta-band profile in Parkinson's disease is stationary and shows prolonged attenuation after deep brain stimulation". In: *Experimental Neurology* 215.1, pp. 20–28.

Buta, R., D. L. Block, and J. H. Knapen (2003). "A Technique for Separating the Gravitational Torques of Bars and Spirals in Disk Galaxies". In: *Astron. J.* 126, pp. 1148–1158.

Buta, R., E. Laurikainen, and H. Salo (2004). "The Distribution of Maximum Relative Gravitational Torques in Disk Galaxies". In: *Astronomical Journal* 127, pp. 279–294.

Buta, Ronald J., Harold G. Corwin, and Stephen C. Odewahn (2007). *The de Vaucouleurs Atlas of Galaxies.*

Cabral, J., E. Hugues, O. Sporns, and G. Deco (2011). "Role of local network oscillations in resting-state functional connectivity". In: *NeuroImage* 57.1, pp. 130–139.

Cachucho, F., P. M. Cincotta, and S. Ferraz-Mello (2010). "Chirikov diffusion in the asteroidal three-body resonance (5, -2, -2)". In: *Celest. Mech. Dyn. Astron.* 108, pp. 35–58.

Casati, G., B. Chirikov, J. Ford, and F. M. Izrailev (1979). "Stochastic behavior of a quantum pendulum under a periodic perturbation". In: *Lect. Notes Phys.* 93, p. 334.

Casati, G. and I. Guarneri (1984). "Non-recurrent behaviour in quantum dynamics". In: *Commun. Math. Phys.* 95, pp. 121–127.

Casati, G., I. Guarneri, F. M. Izrailev, and R. Scharf (1990). "Scaling behavior of localization in quantum chaos". In: *Phys. Rev. Lett.* 64 (1), pp. 5–8.

Casati, G., F. M. Izrailev, and L. Molinari (1991). In: *J. Phys. A: Math. Gen.* 24, p. 4755.

Casati, G., F. Valz-Gris, and I. Guarneri (1980). "On the connection between quantization of nonintegrable systems and statistical theory of spectra". In: *Lett. Nuovo Cimento* 28, pp. 279–282.

Chaves-Velasquez, L., P. A. Patsis, I. Puerari, Ch. Skokos, and T. Manos (2017). "Boxy Orbital Structures in Rotating Bar Models". In: *Astrophys. J.* 850.2, p. 145.

Combes, F. (2008a). In: *Formation and Evolution of Galaxy Discs.* Ed. by J. Funes & E. Corsini. Vol. 396. ASP conference series, p. 325.

— (2008b). "Pattern speed evolution and bar reformation." In: *Memorie della Societa Astronomica Italiana Supplementi* 18, p. 53.

Contarino, M. F., L. J. Bour, R. Verhagen, M. A.J. Lourens, R. M. A. de Bie, P. van den Munckhof, and P. R. Schuurman (2014). "Directional steering". In: *Neurology* 83.13, pp. 1163–1169.

Contopoulos, G. (2002). *Order and Chaos in Dynamical Astronomy.* Berlin: Springer-Verlag.

Contopoulos, G., L. Galgani, and A. Giorgilli (1978). "On the number of isolating integrals in Hamiltonian systems". In: *Phys. Rev. A* 18, pp. 1183–1189.

Contopoulos, G. and M. Harsoula (2008). "Stickiness in Chaos". In: *Int. J. Bif. Chaos* 18, p. 2929.

— (2010). "Stickiness effects in chaos". In: *Celest. Mech. Dyn. Astron.* 107, pp. 77–92.

— (2013). "3D chaotic diffusion in barred spiral galaxies". In: *Mon. Not. R. Astron. Soc.*

damchic, I., P. A. Tass, B. Langguth, C. Hauptmann, M. Koller, M. Schecklmann, F. Zeman, and M. Landgrebe (2012). "Linking the Tinnitus Questionnaire and the subjective Clinical Global Impression: which differences are clinically important?" In: *Health Qual. Life Outcomes* 10, p. 79.

Dash, A., S. Singh, and J. Tolman (2014). *Pharmaceutics: Basic Principles and Application to Pharmacy Practice.* Amsterdam: Elsevier.

Dehnen, W. (1993). "A Family of Potential-Density Pairs for Spherical Galaxies and Bulges". In: *Mon. Not. R. Astron. Soc.* 265, p. 250.

Dehnen, W. (2000). "A Very Fast and Momentum-conserving Tree Code". In: *Astrophys. J.* 536, pp. L39–L42.

— (2002). "A Hierarchical O(N) Force Calculation Algorithm". In: *J. Comput. Phys.* 179, pp. 27–42.

Desikan, R. S., F. Segonne, B. Fischl, B. T. Quinn, B. C. Dickerson, D. Blacker, R. L. Buckner, A. M. Dale, R. P. Maguire, B. T. Hyman, M. S. Albert, and R. J. Killiany (2006). "An automated labeling system for subdividing the human cerebral cortex on MRI scans into gyral based regions of interest". In: *NeuroImage* 31.3, pp. 968–980.

Deuschl, G., C. Schade-Brittinger, P. Krack, J. Volkmann, H. Schäfer, K. Bötzel, C. Daniels, A. Deutschländer, U. Dillmann, W. Eisner, D. Gruber, W. Hamel, J. Herzog, R. Hilker, S. Klebe, M. Kloß, J. Koy, M. Krause, A. Kupsch, D. Lorenz, S. Lorenzl, H. M. Mehdorn, J. R. Moringlane, W. Oertel, M. O. Pinsker, H. Reichmann, A. Reuß, G.-H. Schneider, A. Schnitzler, U. Steude, V. Sturm, L. Timmermann, V. Tronnier, T. Trottenberg, L. Wojtecki, E. Wolf, W. Poewe, and J. Voges (2006). "A Randomized Trial of Deep-Brain Stimulation for Parkinson's Disease". In: *New England Journal of Medicine* 355.9, pp. 896–908. ISSN: 0028-4793.

Diaz-Pier, S., M. Naveau, M. Butz-Ostendorf, and A. Morrison (2016). "Automatic Generation of Connectivity for Large-Scale Neuronal Network Models through Structural Plasticity". In: *Front. Neuroanat.* 10, p. 57.

Dijk, K. J. van, R. Verhagen, A. Chaturvedi, C. C. McIntyre, L. J. Bour, C. Heida, and P. H. Veltink (2015). "A novel lead design enables selective deep brain stimulation of neural populations in the subthalamic region". In: *J. Neural Eng.* 12.4, p. 046003.

Dominguez, M., S. Becker, I. Bruce, and H. Read (2006). "A Spiking Neuron Model of Cortical Correlates of Sensorineural Hearing Loss: Spontaneous Firing, Synchrony, and Tinnitus". In: *Neural Computation* 18.12, pp. 2942–2958.

Ebbinghaus, H., C. E. Bussenius, and H. A. Ruger (1913). *Memory; A Contribution to Experimental Psychology.* New York, NY: Teachers College, Columbia University.

Ebert, M., C. Hauptmann, and P.A. Tass (2014). "Coordinated reset stimulation in a large-scale model of the STN-GPe circuit". In: *Frontiers in Computational Neuroscience* 8, p. 154.

Eggermont, J. J. and P. A. Tass (2015). "Maladaptive Neural Synchrony in Tinnitus: Origin and Restoration". In: *Front. Neurol.* 6, p. 29.

Eickhoff, S. B., B. T. T. Yeo, and S. Genon (2018). "Imaging-based parcellations of the human brain". In: *Nat. Rev. Neurosci.* 19.11, pp. 672–686.

Elgoyhen, A.B., B. Langguth, D. De Ridder, and S. Vanneste (2015). "Tinnitus: perspectives from human neuroimaging". In: *Nat Rev Neurosci.* 16.10, pp. 632–642.

Erwin, Peter and Victor P. Debattista (2013). "Peanuts at an angle: detecting and measuring the three-dimensional structure of bars in moderately inclined galaxies". In: *Mon. Not. R. Astron. Soc.* 431.4.

Esfahani, Z., L. Gollo, and A. Valizadeh (2016). "Stimulus-dependent synchronization in delayed-coupled neuronal networks". In: *Sci. Rep.*, p. 23471.

Ferraye, M. U., B. Debû, V. Fraix, J. Xie-Brustolin, S. Chabardès, P. Krack, A-L Benabid, and P. Pollak (2008). "Effects of subthalamic nucleus stimulation and levodopa on freezing of gait in Parkinson disease". In: *Neurology* 70.16 Part 2, pp. 1431–1437.

Ferrers, N. M. (1877). "On the Potentials, Ellipsoids, Ellipsoidal Shells, Elliptic Laminae and Elliptic Rings, of Variable Densities". In: *Quart. J. Pure Appl. Math.* 14, pp. 1–22.

Fishman, S., D.R. Grempel, and R.E. Prange (1982). "Chaos, Quantum Recurrences, and Anderson Localization". In: *Phys. Rev. Lett.* 49 (8), pp. 509–512.

Fitzhugh, R. (1961). "Impulses and Physiological States in Theoretical Models of Nerve Membrane". In: *Biophys. J.* 1.6, pp. 445–466.

Friedman, L.M., C.D. Furberg, and D. Demets (2010). *Fundamentals of Clinical Trials*. New York, NY: Springer.

Fujisaka, H. (1983). "Statistical Dynamics Generated by Fluctuations of Local Lyapunov Exponents". In: *Prog. Theor. Phys.* 70.5, pp. 1264–1275.

Fukushima, M. and O. Sporns (2018). "Comparison of fluctuations in global network topology of modeled and empirical brain functional connectivity". In: *PLoS Comput. Biol.* 14.9, e1006497.

Geisel, T., J. Nierwetberg, and A. Zacherl (1985). "Accelerated diffusion in Josephson junctions and related chaotic systems". In: *Phys. Rev. Lett.* 54, pp. 616–619.

Gerstner, Wulfram, Richard Kempter, J. Leo van Hemmen, and Hermann Wagner (1996). "A neuronal learning rule for sub-millisecond temporal coding". In: *Nature* 383, pp. 76–78.

Giordano, C. M. and P. M. Cincotta (2004). "Chaotic diffusion of orbits in systems with divided phase space". In: *Astron. Astrophys.* 423, pp. 745–753.

Graupe, D., I. Basu, D. Tuninetti, P. Vannemreddy, and K. V. Slavin (2010). "Adaptively controlling deep brain stimulation in essential tremor patient via surface electromyography". In: *Neurol. Res.* 32.9, pp. 899–904.

Grossmann, S. and M. Robnik (2006). "On level spacing distributions for 2D non-normal Gaussian random matrices". In: *J. Phys. A: Math. Theor.* 40.3, pp. 409–421.

Grygiel, K. and P. Szlachetka (1995). "Lyapunov Exponents Analysis of Autonomous and Nonautonomous Sets of Ordinary Differential Equations". In: *Acta Phys. Pol. B* 26, pp. 1321–1331.

Guhr, T., A. Müller-Groeling, and H.A. Weidenmüller (1998). "Random-matrix theories in quantum physics: common concepts". In: *Phys. Rep.* 299.4, pp. 189–425.

Haake, F. (2001). *Quantum Signatures of Chaos*. Berlin: Springer.

Haken, H. (1983). *Synergetics*. Berlin Springer.

Hammond, C., H. Bergman, and P. Brown (2007). "Pathological synchronization in Parkinson's disease: networks, models and treatments". In: *Trends Neurosci.* 30.7, pp. 357–364.

Hansel, D., G. Mato, and C. Meunier (1993). "Phase Dynamics for Weakly Coupled Hodgkin-Huxley Neurons". In: *Europhys. Lett.* 23.5, pp. 367–372.

Harsoula, M. and C. Kalapotharakos (2009). "Orbital structure in N-body models of barred-spiral galaxies". In: *Mon. Not. R. Astron. Soc.* 394, pp. 1605–1619.

Harsoula, M., C. Kalapotharakos, and G. Contopoulos (2011a). "Asymptotic orbits in barred spiral galaxies". In: *Mon. Not. R. Astron. Soc.* 411, pp. 1111–1126.

— (2011b). "Diffusion of Chaotic Orbits in Barred Spiral Galaxies". In: *Int. J. Bif. Chaos* 21, p. 2221.

Hauptmann, C. and P. A. Tass (2007). "Therapeutic rewiring by means of desynchronizing brain stimulation". In: *Biosystems* 89, pp. 173–181.

— (2009). "Cumulative and after-effects of short and weak coordinated reset stimulation: a modeling study". In: *J. Neural. Eng.* 6.1, p. 016004.

Hénon, M. and C. Heiles (1964). "The Applicability of the Third Integral of Motion: Some Numerical Experiments". In: *Astron. J.* 69.1, pp. 73–79.

Hernquist, L. (1993). "N-body realizations of compound galaxies". In: *Astrophys. J. Suppl. S.* 86, pp. 389–400.

Heusler, S., S. Müller, P. Braun, and F. Haake (2004). In: *J. Phys.A: Math. Gen.* 37.3, pp. L31–L37.

Hodgkin, A. L. and A. F. Huxley (1952). "A quantitative description of membrane current and its application to conduction and excitation in nerve". In: *The Journal of Physiology* 117, pp. 500–544.

Hübener, M. and T. Bonhoeffer (2014). "Neuronal plasticity: beyond the critical period". In: *Cell* 159.4, pp. 727–737.

Huxley, A. F. (1959). "Ion Movements During Nerve Activity". In: *Annals of the New York Academy of Sciences* 81.2, pp. 221–246.

Izhikevich, E. M. (2005). *Dynamical systems in neuroscience: The geometry of excitability and bursting*. MIT Press.

— (2007). *Dynamical systems in neuroscience*. The MIT Press, Cambridge.

Izrailev, F. M. (1986). "Limiting quasienergy statistics for simple quantum systems". In: *Phys. Rev. Lett.* 56 (6), pp. 541–544.

— (1987). "Chaotic stucture of eigenfunctions in systems with maximal quantum chaos". In: *Phys. Lett. A* 125.5, pp. 250–252.

— (1988). "Quantum localization and statistics of quasienergy spectrum in a classically chaotic system". In: *Phys. Lett. A* 134.1, pp. 13–18.

— (1989). "Intermediate statistics of the quasi-energy spectrum and quantum localisation of classical chaos". In: *J. Phys. A: Math. Gen.* 22.7, pp. 865–878.

— (1990). "Simple models of quantum chaos: Spectrum and eigenfunctions". In: *Phys. Rep.* 196.5, pp. 299–392.

Izrailev, F. M. and D. L. Shepelyansky (1980). "Quantum resonance for a rotator in a nonlinear periodic field". In: *Theor. Math. Phys.* 43, pp. 553–561.

Jahanshahi, M., I. Obeso, C. Baunez, M. Alegre, and P. Krack (2015). "Parkinson's Disease, the Subthalamic Nucleus, Inhibition, and Impulsivity". In: *Mov. Disord.* 30.2, pp. 128–140.

Jirsa, V.K., T. Proix, D. Perdikis, M.M. Woodman, H. Wang, J. Gonzalez-Martinez, C. Bernard, C. Bénar, M. Guye, P. Chauvel, and F. Bartolomei (2017). "The Virtual Epileptic Patient: Individualized whole-brain models of epilepsy spread". In: *NeuroImage* 145, pp. 377–388.

Katsanikas, M. and P. A. Patsis (2011). "The Structure of Invariant Tori in a 3d Galactic Potential". In: *Int. J. Bif. Chaos* 21, p. 467.

Katsanikas, M., P. A. Patsis, and G. Contopoulos (2011). "The Structure and Evolution of Confined Tori Near a Hamiltonian Hopf Bifurcation". In: *Int. J. Bif. Chaos* 21, p. 2321.

Katsanikas, M., P. A. Patsis, and A. D. Pinotsis (2011). "Chains of Rotational Tori and Filamentary Structures Close to High Multiplicity Periodic Orbits in a 3d Galactic Potential". In: *Int. J. Bif. Chaos* 21, p. 2331.

Kaufmann, D. E. and G. Contopoulos (1996). "Self-consistent models of barred spiral galaxies." In: *Astron. Astrophys.* 309, pp. 381–402.

Kelley, P. and T. Whatson (2013). "Making long-term memories in minutes: a spaced learning pattern from memory research in education". In: *Front. Hum. Neurosci.* 7, p. 589.

Klafter, J. and G. Zumofen (1994). "Lévy statistics in a Hamiltonian system". In: *Phys. Rev. E* 49, pp. 4873–4877.

Kottos, T., A. Politi, F.M. Izrailev, and S. Ruffo (1996). "Scaling properties of Lyapunov spectra for the band random matrix model". In: *Phys. Rev. E* 53 (6), R5553–R5556.

Krack, P., A. Batir, N. Van Blercom, S. Chabardes, V. Fraix, C. Ardouin, A. Koudsie, P. D. Limousin, A. Benazzouz, J. F. LeBas, A.-L. Benabid, and P. Pollak (2003). "Five-Year Follow-up of Bilat-

eral Stimulation of the Subthalamic Nucleus in Advanced Parkinson's Disease". In: *New England Journal of Medicine* 349.20, pp. 1925–1934. ISSN: 0028-4793.

Kühn, A. A., F. Kempf, C. Brücke, L. G. Doyle, I. Martinez-Torres, Alek Pogosyan, T. Trottenberg, A. Kupsch, G.-H. Schneider, M. I. Hariz, W. Vandenberghe, B. Nuttin, and P. Brown (2008). "High-frequency stimulation of the subthalamic nucleus suppresses oscillatory beta-activity in patients with Parkinson's disease in parallel with improvement in motor performance". In: *J. Neurosci.* 28.24, pp. 6165–6173.

Kühn, A. A. and J. Volkmann (2017). "Innovations in deep brain stimulation methodology". In: *Mov. Disord.* 32.1, pp. 11–19.

Kuramoto, Y. (1984). *Chemical oscillations, waves, and turbulence*. Berlin: Springer.

Lenz, F. A., H. C. Kwan, R. L. Martin, R. R. Tasker, J. O. Dostrovsky, and Y. E. Lenz (1994). "Single unit analysis of the human ventral thalamic nuclear group - Tremor-related activity in functionally identified cells". In: *Brain* 117, pp. 531–543.

Lichtenberg, A. J. and M. A. Lieberman (1992). *Regular and Chaotic Dynamics*. 2nd. Applied Mathematical Sciences 38. New York, NY: Springer-Verlag.

Little, S., A. Pogosyan, S. Neal, B. Zavala, L. Zrinzo, M. Hariz, T. Foltynie, P. Limousin, K. Ashkan, J. FitzGerald, A. L. Green, T. Z. Aziz, and P. Brown (2013). "Adaptive deep brain stimulation in advanced Parkinson disease". In: *Ann. Neurol.* 74.3, pp. 449–57.

Lysyansky, B., O. V. Popovych, and P. A Tass (May 2011). "Desynchronizing anti-resonance effect of m:n ON-OFF coordinated reset stimulation". In: *J. Neural. Eng.* 8.3, p. 036019.

Machado, R. E. G. and E. Athanassoula (2010). "Loss of halo triaxiality due to bar formation". In: *Mon. Not. R. Astron. Soc.* 406, pp. 2386–2404.

Maffione, N. P., L. A. Darriba, P. M. Cincotta, and C. M. Giordano (2011). "A comparison of different indicators of chaos based on the deviation vectors: application to symplectic mappings". In: *Celestial Mechanics and Dynamical Astronomy* 111, pp. 285–307.

— (2013). "Chaos detection tools: application to a self-consistent triaxial model". In: *Mon. Not. R. Astron. Soc.* 429, pp. 2700–2717.

Maistrenko, Yuri L., Borys Lysyansky, Christian Hauptmann, Oleksandr Burylko, and Peter A. Tass (2007). "Multistability in the Kuramoto model with synaptic plasticity". In: *Phys. Rev. E* 75.6, pp. 066207–066207.

Manos, T. and E. Athanassoula (2011). "Regular and chaotic orbits in barred galaxies - I. Applying the SALI/GALI method to explore their distribution in several models". In: *Mon. Not. R. Astron. Soc.* 415, pp. 629–642.

Manos, T., T. Bountis, and C. Skokos (2013). "Interplay between chaotic and regular motion in a time-dependent barred galaxy model". In: *J. Phys. A: Math. Theor.* 46.25, 254017, p. 254017.

Manos, T. and R. E. G. Machado (2014). "Chaos and dynamical trends in barred galaxies: bridging the gap between N-body simulations and time-dependent analytical models". In: *Mon. Not. R. Astron. Soc.* 438, pp. 2201–2217.

Manos, T. and M. Robnik (2013). "Dynamical localization in chaotic systems: Spectral statistics and localization measure in the kicked rotator as a paradigm for time-dependent and time-independent systems". In: *Phys. Rev. E* 87 (6), p. 062905.

— (2014). "Survey on the role of accelerator modes for anomalous diffusion: The case of the standard map". In: *Phys. Rev. E* 89 (2), p. 022905.

— (2015). "Statistical properties of the localization measure in a finite-dimensional model of the quantum kicked rotator". In: *Phys. Rev. E* 91 (4), p. 042904.

Manos, T. and S. Ruffo (2011). "Scaling with System Size of the Lyapunov Exponents for the Hamiltonian Mean Field Model". In: *Transport Theor. Stat.* 40, pp. 360–381.

Manos, T., C. Skokos, and C. Antonopoulos (2012). "Probing the local dynamics of periodic orbits by the generalized alignment index (GALI) method". In: *Int. J. Bif. Chaos* 22, p. 1250218.

Manos, T., C. Skokos, E. Athanassoula, and T. Bountis (2008). "Studying the global dynamics of conservative dynamical systems using the SALI chaos detection method". In: *Nonlinear Phenom. Complex Syst.* 11, pp. 171–176.

Manos, T., M. Zeitler, and P. A. Tass (2018a). "How stimulation frequency and intensity impact on the long-lasting effects of coordinated reset stimulation". In: *PLoS Comput. Biol.* 14.5, e1006113.

— (2018b). "Short-Term Dosage Regimen for Stimulation-Induced Long-Lasting Desynchronization". In: *Front. Physiol.* 9, p. 376.

Markram, H., W. Gerstner, and P.J. Sjostrom (2012). "Spike-timing-dependent plasticity: A comprehensive overview". In: *Front. Synaptic Neurosci.* 4.2, p. 2.

Markram, Henry, Joachim Lübke, Michael Frotscher, and Bert Sakmann (1997). "Regulation of synaptic efficacy by coincidence of postsynaptic APs and EPSPs". In: *Science* 275.5297, pp. 213–215.

Martens, H. C. F., E. Toader, M. M. J. Decré, D. J. Anderson, R. Vetter, D. R. Kipke, Kenneth B. Baker, Matthew D. Johnson, and Jerrold L. Vitek (2011). "Spatial steering of deep brain stimulation volumes using a novel lead design". In: *Clin. Neurophysiol.* 122.3, pp. 558–566.

Mehta, M. L. (1991). *Random Matrices*. Boston: Academic Press.

Miyamoto, M. and R. Nagai (1975). "Three-dimensional models for the distribution of mass in galaxies". In: *PASJ* 27, pp. 533–543.

Moges, H., T. Manos, and Ch. Skokos (2020). "On the behavior of the Generalized Alignment Index (GALI) method for regular motion in multidimensional Hamiltonian systems". In: *Nonlin. Phenom. Complex Syst.* 23.2, pp. 153–164.

Müller, S., S. Heusler, A. Altland, P. Braun, and F. Haake (2009). "Periodic-orbit theory of universal level correlations in quantum chaos". In: *New J. of Phys.* 11.10, p. 103025.

Müller, S., S. Heusler, P. Braun, F. Haake, and A. Altland (2004). "Semiclassical Foundation of Universality in Quantum Chaos". In: *Phys. Rev. Lett.* 93 (1), p. 014103.

— (2005). "Periodic-orbit theory of universality in quantum chaos". In: *Phys. Rev. E* 72 (4), p. 046207.

Muzzio, J. C., D. D. Carpintero, and F. C. Wachlin (2005). "Spatial Structure of Regular and Chaotic Orbits in A Self-Consistent Triaxial Stellar System". In: *Celest. Mech. Dyn. Astron.* 91, pp. 173–190.

Naqib, F., W. S. Sossin, and C. A. Farah (2012). "Molecular determinants of the spacing effect". In: *Neural Plast.*, p. 581291.

Nini, A., A. Feingold, H. Slovin, and H. Bergmann (1995). "Neurons in the globus pallidus do not show correlated activity in the normal monkey, but phase-locked oscillations appear in the MPTP model of parkinsonism". In: *J. Neurophysiol.* 74, pp. 1800–1805.

Nolan, J. P. (2013). *Stable Distributions - Models for Heavy Tailed Data*. In progress, Chapter 1 online at academic2.american.edu/∼jpnolan. Boston: Birkhauser.

Ochi, K. and J. J. Eggermont (1997). "Effects of quinine on neural activity in cat primary auditory cortex". In: *Hear. Res.* 105.1, pp. 105–118.

Ott, E. (1993). *Chaos in Dynamical Systems*. Cambridge University Press.

Özkurt, T. E., M. Butz, M. Homburger, S. Elben, J. Vesper, L. Wojtecki, and A. Schnitzler (2011). "High frequency oscillations in the subthalamic nucleus: A neurophysiological marker of the motor state in Parkinson's disease". In: *Exp. Neurol.* 229.2, pp. 324–331.

Patsis, P. A. (2006). "The stellar dynamics of spiral arms in barred spiral galaxies". In: *Mon. Not. R. Astron. Soc.* 369, pp. L56–L60.

Patsis, P. A., E. Athanassoula, and A. C. Quillen (1997). "Orbits in the Bar of NGC 4314". In: *Astrophys. J.* 483, p. 731.

Patsis, P. A. and M. Katsanikas (2014a). "The phase space of boxy-peanut and X-shaped bulges in galaxies - I. Properties of non-periodic orbits". In: *Mon. Not. R. Astron. Soc.* 445, pp. 3525–3545.

— (2014b). "The phase space of boxy-peanut and X-shaped bulges in galaxies - I. Properties of non-periodic orbits". In: *Mon. Not. R. Astron. Soc.* 445, pp. 3525–3545.

— (2014c). "The phase space of boxy-peanut and X-shaped bulges in galaxies - II. The relation between face-on and edge-on boxiness". In: *Mon. Not. R. Astron. Soc.* 445, pp. 3546–3556.

— (2014d). "The phase space of boxy-peanut and X-shaped bulges in galaxies - II. The relation between face-on and edge-on boxiness". In: *Mon. Not. R. Astron. Soc.* 445, pp. 3546–3556.

Patsis, P. A., D. E. Kaufmann, S. T. Gottesman, and V. Boonyasait (2009). "Stellar and gas dynamics of late-type barred-spiral galaxies: NGC 3359, a test case". In: *Mon. Not. R. Astron. Soc.* 394, pp. 142–156.

Pfenniger, D. (1984). "The 3D dynamics of barred galaxies". In: *Astron. Astrophys.* 134, pp. 373–386.

Pfister, J.-P. and P.A. Tass (2010). "STDP in Oscillatory Recurrent Networks: Theoretical Conditions for Desynchronization and Applications to Deep Brain Stimulation". In: *Front. Comput. Neurosci.* 4, p. 22.

Philippens, I. H. C. H. M., J. A. Wubben, R. A. P. Vanwersch, D. L. Estevao, and P. A. Tass (2017). "Sensorimotor rhythm neurofeedback as adjunct therapy for Parkinson's disease". In: *Ann. Clin. Transl. Neurol.* 4.8, pp. 585–590.

Pikovsky, A. S. and J. Kurths (1997). "Coherence Resonance in a Noise-Driven Excitable System". In: *Phys. Rev. Lett.* 78 (5), pp. 775–778.

Pikovsky, Arkady, Michael Rosenblum, and Jürgen Kurths (2003). *Synchronization: A universal concept in nonlinear sciences*. Cambridge University Press.

Ponce-Alvarez, A., G. Deco, P. Hagmann, G. L. Romani, D. Mantini, and M. Corbetta (2015). "Resting-State Temporal Synchronization Networks Emerge from Connectivity Topology and Heterogeneity". In: *PLoS Comput. Biol.* 11.2, e1004100.

Popovych, O. V., T. Manos, F. Hoffstaedter, and S. B. Eickhoff (2019). "What can computational models contribute to neuroimaging data analytics?" In: *Front. Syst. Neurosci.* 12, p. 68.

Popovych, O. V., M. N. Xenakis, and P. A. Tass (2015). "The Spacing Principle for Unlearning Abnormal Neuronal Synchrony". In: *PLoS One* 10.2, e0117205.

Popovych, O.V. and P.A. Tass (2012). "Desynchronizing electrical and sensory coordinated reset neuromodulation". In: *Front. Hum. Neurosci.* 6, p. 58.

Porter, C. E. (1965). *Statistical theory of spectra: fluctuations*. New York: Acadedic Press.

Proix, T., F. Bartolomei, M. Guye, and V. K. Jirsa (2017). "Individual brain structure and modelling predict seizure propagation". In: *Brain* 140.3, pp. 641–654.

Prosen, T. (2000). *in Proceedings of the International School of Physics "Enrico Fermi", Course CXLIII*. edited by G. Casati and I. Guarneri and U. Smilyanski (Amsterdam: IOS Press, 2000) p. 473.

Prosen, T. and M. Robnik (1993). "Energy level statistics in the transition region between integrability and chaos". In: *J. Phys. A: Math. Gen.* 26.10, pp. 2371–2387.

Prosen, T. and M. Robnik (1994a). "Semiclassical energy level statistics in the transition region between integrability and chaos: transition from Brody-like to Berry-Robnik behaviour". In: *J. Phys. A: Math. Gen.* 27.24, pp. 8059–8077.

— (1994b). "Semiclassical energy level statistics in the transition region between integrability and chaos: transition from Brody-like to Berry-Robnik behaviour". In: *J. Phys. A: Math. Gen.* 27.24, pp. 8059–8077.

— (1998). "General Poissonian model of diffusion in chaotic components". In: *J. Phys. A: Math. Gen.* 31.18, pp. L345–L353.

— (1999a). "Intermediate statistics in the regime of mixed classical dynamics". In: *J. Phys. A: Math. Gen.* 32.10, pp. 1863–1873.

— (1999b). "Intermediate statistics in the regime of mixed classical dynamics". In: *J. Phys. A: Math. Gen.* 32.10, pp. 1863–1873.

Quinn, E. J., Z. Blumenfeld, A. Velisar, M. M. Koop, L. A. Shreve, M. H. Trager, B. C. Hill, C. Kilbane, J. M. Henderson, and H. Brontë-Stewart (2015). "Beta oscillations in freely moving Parkinson's subjects are attenuated during deep brain stimulation". In: *Mov. Disord.* 30.13, pp. 1750–1758.

Rimmer, R. H. and J. P. Nolan (2005). "Stable Distributions in Mathematica". In: *Mathematica J.* 9, pp. 776–789.

Robnik, M. and M. V. Berry (1986). "False time-reversal violation and energy level statistics: the role of anti-unitary symmetry". In: *J. Phys. A: Math. Gen.* 19.5, pp. 669–682.

Robnik, M. and G. Veble (1998). "On spectral statistics of classically integrable systems". In: *J. Phys. A: Math. Gen.* 31.20, pp. 4669–4704.

Rocha, J. de la, C. Marchetti, M. Schiff, and A. D. Reyes (2008). "Linking the Response Properties of Cells in Auditory Cortex with Network Architecture: Cotuning versus Lateral Inhibition". In: *Journal of Neuroscience* 28.37, pp. 9151–9163.

Romero-Gómez, M., E. Athanassoula, J. J. Masdemont, and C. Garcıéa-Gómez (2007). "The formation of spiral arms and rings in barred galaxies". In: *Astron. Astrophys.* 472, pp. 63–75.

Romero-Gómez, M., J. J. Masdemont, E. Athanassoula, and C. Garcıéa-Gómez (2006). "The origin of rR1 ring structures in barred galaxies". In: 453, pp. 39–45.

Rosa, M., M. Arlotti, G. Ardolino, F. Cogiamanian, S. Marceglia, A. Di Fonzo, F. Cortese, P. M. Rampini, and A. Priori (2015). "Adaptive deep brain stimulation in a freely moving Parkinsonian patient". In: *Mov. Disord.* 30.7, pp. 1003–5.

Rosin, B., M. Slovik, R. Mitelman, M. Rivlin-Etzion, S. N. Haber, Z. Israel, E. Vaadia, and H. Bergman (2011). "Closed-Loop Deep Brain Stimulation Is Superior in Ameliorating Parkinsonism". In: *Neuron* 72.2, pp. 370–384.

Saito, R. K., M. Zoccali, A. McWilliam, D. Minniti, O. A. Gonzalez, and V. Hill (2011). "Mapping the X-shaped Milky Way Bulge". In: *Astron. J.* 142, 76, p. 76.

Schaefer, A., R. Kong, E. M. Gordon, T. O. Laumann, X. N. Zuo, A. J. Holmes, S. B. Eickhoff, and B. T. Thomas (2018). "Local-Global Parcellation of the Human Cerebral Cortex from Intrinsic Functional Connectivity MRI". In: *Cereb. Cortex* 28.9, pp. 3095–3114.

Shepelyansky, D. L. (1986). "Localization of quasienergy eigenfunctions in action space". In: *Phys. Rev. Lett.* 56 (7), pp. 677–680.

Sieber, M. and K. Richter (2001). "Correlations between Periodic Orbits and their R?le in Spectral Statistics". In: *Physica Scripta* T90.1, p. 128.

Silchenko, A. N., I. Adamchic, C. Hauptmann, and P. A. Tass (2013). "Impact of acoustic coordinated reset neuromodulation on effective connectivity in a neural network of phantom sound". In: *NeuroImage* 77, pp. 133–147.

Skokos, C. (2010). "The Lyapunov Characteristic Exponents and Their Computation". In: *Lect. Notes Phys.* 790, pp. 63–135.

Skokos, C., T. Bountis, and C. Antonopoulos (2008). "Detecting chaos, determining the dimensions of tori and predicting slow diffusion in Fermi-Pasta-Ulam lattices by the Generalized Alignment Index method". In: *Eur. Phys. J. Spec. Top.* 165, pp. 5–14.

Skokos, C., T. C. Bountis, and C. Antonopoulos (2007). "Geometrical properties of local dynamics in Hamiltonian systems: The Generalized Alignment Index (GALI) method". In: *Physica D* 231, pp. 30–54.

Skokos, C. and T. Manos (2016). "The Smaller (SALI) and the Generalized (GALI) Alignment Indices: Efficient Methods of Chaos detection". In: *Lect. Notes Phys.* 915.

Skokos, Ch., T. Bountis, and Ch. Antonopoulos (2007). In: *Physica D* 231, p. 30.

Skokos, Ch., G. A. Gottwald, and J. Laskar, eds. (2016). *Chaos Detection and Predictability*. Vol. 915. Lect. Notes Phys. Berlin-Heidelberg: Springer-Verlag.

Skokos, Ch., P. A. Patsis, and E. Athanassoula (2002). "Orbital dynamics of three-dimensional bars – I. The backbone of three-dimensional bars. A fiducial case". In: *Mon. Not. R. Astron. Soc.* 333.4, pp. 847–860.

Sporns, O. (2011). *Networks of the Brain*. Cambridge, MIT Press.

Sporns, O., G. Tononi, and R. Kötter (2005). "The Human Connectome: A Structural Description of the Human Brain". In: *PLoS Comput. Biol.* 1.4.

Stanley, M. L., M. N. Moussa, B. M. Paolini, R. G. Lyday, J. H. Burdette, and P. J. Laurienti (2013). "Defining nodes in complex brain networks". In: *Front. Comput. Neurosci.* 7, UNSP 169.

Stöckmann, H. J. (1999). *Quantum Chaos - An Introduction*. Cambridge: Cambridge University Press.

Strogatz, S. H. (2000). *Nonlinear Dynamics and Chaos: With Applications to Physics, Biology, Chemistry and Engineering*. Westview Press.

— (2003). *Sync: The Emerging Science of Spontaneous Order*. Hyperion Press.

Symonds, R., C. Deehan, C. Meredith, and J. Mills (2012). *Walter and Miller's Textbook of Radiotherapy: Radiation physics, Therapy and Oncology*. Churchill Livingstone: Elsevier.

Syrkin-Nikolau, J., R. Neuville, J. O'Day, C. Anidi, M. Miller Koop, T. Martin, P. A. Tass, and H. Bronte-Stewart (2018). "Coordinated reset vibrotactile stimulation shows prolonged improvement in Parkinson's disease". In: *Mov. Disord.* 33.1, pp. 179–180.

Tass, P. A. (1999). *Phase resetting in medicine and biology - stochastic modelling and data analysis*. Springer.

— (2001). "Desynchronizing double-pulse phase resetting and application to deep brain stimulation". In: *Biol. Cybern.* 85, pp. 343–354.

— (2003a). "A model of desynchronizing deep brain stimulation with a demand-controlled coordinated reset of neural subpopulations". In: *Biol. Cybern.* 89.2, pp. 81–88.

— (2003b). "Desynchronization by means of a coordinated reset of neural sub-populations". In: *Progress of Theoretical Physics Supplement* 150, pp. 281–296.

— (2017). "Vibrotactile Coordinated Reset Stimulation for the Treatment of Neurological Diseases: Concepts and Device Specifications". In: *Cureus* 9.8, e1535.

Tass, P. A. and O. Popovych (2012). "Unlearning tinnitus-related cerebral synchrony with acoustic coordinated reset stimulation: theoretical concept and modelling". In: *Biol. Cybern.* 106.1, pp. 27–36.

Tass, P. A., L. Qin, C. Hauptmann, S. Dovero, E. Bezard, T. Boraud, and W. G. Meissner (2012a). "Coordinated reset has sustained aftereffects in Parkinsonian monkeys". In: *Ann. Neurol.* 72.5, pp. 816–820.

— (2012b). "Coordinated reset has sustained aftereffects in Parkinsonian monkeys". In: *Ann. Neurol.* 72.5, pp. 816–820.

Tass, P.A., I. Adamchic, H.J. Freund, T. von Stackelberg, and C. Hauptmann (2009). "Counteracting tinnitus by acoustic coordinated reset neuromodulation". In: *Restor. Neurol. Neurosci.* 30.2, pp. 137–159.

Tass, P.A., A.N. Silchenko, C. Hauptmann, U.B. Barnikol, and E.J. Speckmann (2009). "Long-lasting desynchronization in rat hippocampal slice induced by coordinated reset stimulation". In: *Phys. Rev. E Stat. Nonlin. Soft. Matter Phys.* 80, p. 011902.

Tass, Peter A. and Milan Majtanik (2006). "Long-term anti-kindling effects of desynchronizing brain stimulation: a theoretical study". In: *Biol. Cybern.* 94.1, pp. 58–66.

Temperli, P., J. Ghika, J. G. Villemure, P. R. Burkhard, J. Bogousslavsky, and F. J. G. Vingerhoets (2003). "How do parkinsonian signs return after discontinuation of subthalamic DBS?" In: *Neurology* 60.1, p. 78.

Thirion, B., G. Varoquaux, E. Dohmatob, and J.-B. Poline (2014). "Which fMRI clustering gives good brain parcellations?" In: *Front. Neurosci.* 8, p. 167.

Timmer, J., S. Häussler, M. Lauk, and C.-H. Lücking (2000). "Pathological tremors: Deterministic chaos or nonlinear stochastic oscillators?" In: *Chaos* 10.1, pp. 278–288.

Tsigaridi, L. and P. A. Patsis (2015). "Morphologies introduced by bistability in barred-spiral galactic potentials". In: *Mon. Not. R. Astron. Soc.* 448, pp. 3081–3092.

Valluri, M., V. P. Debattista, G. S. Stinson, J. Bailin, T. R. Quinn, H. M. P. Couchman, and J. Wadsley (2013). "Halo Orbits in Cosmological Disk Galaxies: Tracers of Formation History". In: *Astrophys. J.* 767, 93, p. 93.

Vasiliev, E. (2013). "A new code for orbit analysis and Schwarzschild modelling of triaxial stellar systems". In: *Mon. Not. R. Astron. Soc.* 434.

Vemuri, V. (1978). *Modeling of Complex Systems: An Introduction*. New York: Academic Press.

Vidmar, G., H. J. Stöckmann, M. Robnik, U. Kuhl, R. Höhmann, and S. Grossmann (2007). In: *J. Phys. A: Math. Theor.* 40, p. 13883.

Voglis, N., I. Stavropoulos, and C. Kalapotharakos (2006). "Chaotic motion and spiral structure in self-consistent models of rotating galaxies". In: *Mon. Not. R. Astron. Soc.* 372, pp. 901–922.

Volman, V., M. Perc, and M. Bazhenov (2011). "Gap junctions and epileptic seizures–two sides of the same coin?" In: *PLoS One* 6.5, e20572.

Wang, J., S. Nebeck, A. Muralidharan, M. D. Johnson, J. L. Vitek, and K. B. Baker (2016). "Coordinated Reset Deep Brain Stimulation of Subthalamic Nucleus Produces Long-Lasting, Dose-Dependent Motor Improvements in the 1-Methyl-4-phenyl-1,2,3,6-tetrahydropyridine Non-Human Primate Model of Parkinsonism". In: *Brain Stimul* 9.4, pp. 609–17.

Wang, Y., H. Zhao, S. Mao, and R. M. Rich (2012). "A new model for the Milky Way bar". In: *Mon. Not. R. Astron. Soc.* 427, pp. 1429–1440.

Williams, R. L. (1992). "Dosage regimen design: pharmacodynamic considerations". In: *J. Clin. Pharmacol.* 32, pp. 597–602.

Wilson H. R, Cowan J. D. (1973). "A mathematical theory of the functional dynamics of cortical and thalamic nervous tissue". In: *Kybernetik* 13.2, pp. 55–80.

Winfree, A. T. (1980). *The Geometry of Biological Time*. Springer-Verlag Berlin Heidelberg.

Wong, R.K., R.D. Traub, and R. Miles (1986). "Cellular basis of neuronal synchrony in epilepsy". In: *Adv. Neurol.* 44, pp. 583–592.

Yanagisawa, T., O. Yamashita, M. Hirata, H. Kishima, Y. Saitoh, T. Goto, T. Yoshimine, and Y. Kamitani (2012). "Regulation of Motor Representation by Phase-Amplitude Coupling in the Sensorimotor Cortex". In: *J. Neurosci.* 32.44, pp. 15467–15475.

Yang, A. I., N. Vanegas, C. Lungu, and K. A. Zaghloul (2014). "Beta-Coupled High-Frequency Activity and Beta-Locked Neuronal Spiking in the Subthalamic Nucleus of Parkinson's Disease". In: *J. Neurosci.* 34.38, pp. 12816–12827.

Yulmetyev, R. M., S. A. Demin, O. Yu. Panischev, P. Hänggi, S. F. Timashev, and G. V. Vstovsky (2006). "Regular and stochastic behavior of Parkinsonian pathological tremor signals". In: *Physica A* 369.2, pp. 655–678.

El-Zant, A. and I. Shlosman (2002). "Dark Halo Shapes and the Fate of Stellar Bars". In: *Astrophys. J.* 577, pp. 626–650.

Zaslavsky, G. M. (2007). *The Physics of Chaos in Hamiltonian Systems*. London: Imperial College Press.

Zaslavsky, G. M. and M. Edelman (2000). "Hierarchical structures in the phase space and fractional kinetics: I. Classical systems". In: *Chaos* 10, pp. 135–146.

Zaslavsky, G. M., M. Edelman, and B. A. Niyazov (1997). "Self-similarity, renormalization, and phase space nonuniformity of Hamiltonian chaotic dynamics". In: *Chaos* 7, pp. 159–181.

Zeitler, M. and P. A. Tass (2015). "Augmented brain function by coordinated reset stimulation with slowly varying sequences". In: *Front. Syst. Neurosci.* 9, p. 49.

— (2016). "Anti-kindling Induced by Two-Stage Coordinated Reset Stimulation with Weak Onset Intensity". In: *Front. Comput. Neurosci.* 10, p. 44.

Zhang, H., Q. Wang, M. Perc, and G. Chen (2013). "Synaptic plasticity induced transition of spike propagation in neuronal networks". In: *Commun. Nonlinear Sci. Numer. Simul.* 18.3, pp. 601–615.

Zoccali, M., O. A. Gonzalez, S. Vasquez, V. Hill, M. Rejkuba, E. Valenti, A. Renzini, A. Rojas-Arriagada, I. Martinez-Valpuesta, C. Babusiaux, T. Brown, D. Minniti, and A. McWilliam (2014). "The GIRAFFE Inner Bulge Survey (GIBS). I. Survey description and a kinematical map of the Milky Way bulge". In: *Astron. Astrophys.* 562, A66.